

Thunderstorm Tracking and Monitoring on the Basis of Three-Dimensional Lightning Data and Conventional and Polarimetric Radar Data

A THESIS SUBMITTED TO THE FAKULTÄT FÜR PHYSIK,
LUDWIG-MAXIMILIANS-UNIVERSITÄT
MÜNCHEN FOR THE DEGREE OF DR. RER. NAT.



PRESENTED BY
DIPL.-ING. VERA MEYER
from Vienna, Austria

SUBMITTED ON 30 MAY 2010

Thunderstorm Tracking and Monitoring on the Basis of Three Dimensional Lightning Data and Conventional and Polarimetric Radar Data

A THESIS SUBMITTED TO THE FAKULTÄT FÜR PHYSIK,
LUDWIG-MAXIMILIANS-UNIVERSITÄT
MÜNCHEN FOR THE DEGREE OF DR. RER. NAT.



PRESENTED BY
DIPL.-ING. VERA MEYER
from Vienna, Austria

SUBMITTED ON 30 MAY 2010

Gutachter der Dissertation:

apl. Prof. Dr. habil. U. Schumann
Prof. Dr. H. D. Betz

Verteidigung der Arbeit am 28.06.2010

Contents

| | |
|---|-----------|
| Contents | i |
| Abstract | v |
| 1 Introduction | 1 |
| 2 Background of Convection Lifecycles and their Nowcasting | 5 |
| 2.1 Cloud Electrification and Lightning Discharges in Thunderstorms | 5 |
| 2.1.1 Global Electric Circuit | 5 |
| 2.1.2 Electrification Processes and Electrical Structure in Thunderstorms | 5 |
| 2.1.3 Lightning Processes and Their Discharge Characteristics | 7 |
| 2.2 Conceptual Model for Thunderstorm Development and Evolution | 14 |
| 2.2.1 Classical Life-Cycle Model | 14 |
| 2.2.2 Organization Forms of Thunderstorms | 17 |
| 2.3 Data Sources and Measurement Principles | 18 |
| 2.3.1 Lightning Monitoring Methods | 18 |
| 2.3.2 Radar Systems | 26 |
| 2.4 Methods and Applications of Thunderstorm Nowcasting | 30 |
| 2.4.1 Scale Dependencies | 30 |
| 2.4.2 Current Status of Thunderstorm Nowcasting | 32 |
| 2.4.3 Operational Thunderstorm Nowcasting Tools | 34 |
| 3 Methodology and Data Sources | 37 |
| 3.1 Concept ec-TRAM | 37 |
| 3.1.1 General Approach | 37 |
| 3.1.2 Radar-Cell Tracker rad-TRAM | 43 |
| 3.1.3 Lightning-Cell Tracker li-TRAM | 45 |
| 3.1.4 Tracking Method ec-TRAM | 46 |
| 3.1.5 Cell Database | 48 |
| 3.2 Data Sources | 49 |
| 3.2.1 Lightning detection network - LINET | 49 |
| 3.2.2 DWD Radar Fürholzen | 56 |
| 3.2.3 DLR Radar POLDIRAD | 56 |
| 3.2.4 Satellite Data from cell tracking algorithm Cb-TRAM | 57 |
| 3.2.5 Sampling Domain and Period | 58 |

| | |
|--|------------|
| 4 Performance and Verification of the Thunderstorm Tracker ec-TRAM | 61 |
| 4.1 Cell Identification with ec-TRAM | 62 |
| 4.2 Cell Tracking with ec-TRAM | 68 |
| 4.3 Cell Nowcasting and Nowcast Quality with ec-TRAM | 73 |
| 4.4 Statistical Analyses of Selected Cell Parameters | 74 |
| 5 Evaluation of Convective Life-Cycles from Thunderstorm Cell Tracker ec-TRAM | 81 |
| 5.1 Case-studies | 82 |
| 5.2 Statistical Results | 89 |
| 5.2.1 Lightning-Cell Parameter Correlations | 89 |
| 5.2.2 Time Lagged IC and CG Discharge Activity | 95 |
| 6 Conclusion and Outlook | 97 |
| A Appendix | 105 |
| A.1 Definition of Radio Wave Frequency Bands | 105 |
| A.2 Definition of Box-And-Whisker Plot | 105 |
| A.3 Verification Methods for Dichotomous (Yes/No) Forecasts | 106 |
| A.4 SQL Database | 108 |
| A.4.1 Tabular Structure and Linkages | 108 |
| A.4.2 Cell Parameters | 108 |
| A.5 Linear Lightning-Cell Parameter Correlation Plots with Distribution Spread | 114 |
| Acknowledgements | 119 |
| Bibliography | 120 |

Abstract

The aim of this work is to assess the benefit of total-lightning information as independent data source for thunderstorm tracking and short-term prediction (nowcasting) of storm evolution. Special focus has been laid on the three-dimensional lightning information and the in-cloud and cloud-to-ground discrimination provided by the lightning detection network LINET. The reliability of the lightning information and its usability for nowcasting purposes have been tested both separately and in combination with other data sources which are commonly used for thunderstorm nowcasting.

The new thunderstorm tracker ec-TRAM (tracking and monitoring of electrically charged cells; Meyer et al. (2009)) has been developed to identify, track, and monitor thunderstorms in high temporal and spatial resolution by combining the information of independently tracked convective ground-precipitation cells and lightning-cells to new cell objects. The algorithm builds on the autonomously operating routines rad-TRAM (tracking and monitoring of radar cells; Kober and Tafferner (2009)) and li-TRAM (tracking and monitoring of lightning cells). The latter has also been developed within this work.

The new tracking algorithm has been tested based on a thunderstorm data set of more than 500 storm tracks which were recorded by ec-TRAM in southern Germany during summer 2008. It is found that the newly composed cell objects comprehensively describe simple as well as complex thunderstorm structures and the cell tracking method of ec-TRAM proves to be more coherent and stable in comparison with the tracking performances of rad-TRAM and li-TRAM.

For two selected thunderstorms the time series of cell parameters monitored by ec-TRAM have been complemented with three-dimensional polarimetric radar data and satellite data to assess how the temporal evolution and parameter correlation of total-lightning strokes, hydrometeor formation, ground precipitation patterns, and cloud top temperature can be used to estimate the storm state and predict its development. The parameter evolutions are found to be consistent with the current state of knowledge. A principal life-cycle scheme can be identified for the cell parameters on large time scales. The stronger fluctuating short-term parameter evolutions are found to reflect the momentary storm dynamic. Based on the lifetime diagrams several warning parameters for subsequent storm events can be suggested.

Significant cell parameter correlations, which can be parameterized, are also found in statistical analyses over the complete data set. Strong positive correlations are found between cell extension, discharge frequency, and in-cloud discharge height. Two cell-regimes, sharply separated at a specific cell characteristic, can clearly be identified in all correlation diagrams. Interpreted on the basis of previous studies and in terms of the current state of knowledge, it seems most likely that the two cell-regimes reflect the storm characteristics of different storm organization forms. The parameterized correlation curves could then be used as cell parameterizations in operational nowcasting tools to predict the dynamic evolution, duration, and danger potential of a storm, provided that the storm system can be classified. Finally, it can be concluded that this study demonstrates the usability and the promising potential of total-lightning data as reliable and independent data source for future nowcasting tools.

Chapter 1

Introduction

Improved short-term prediction (nowcasting) of thunderstorm propagation and evolution and thunderstorm-related hazards like heavy rain, hail, and lightning strikes are of high benefit for weather-dependent industries. Although embedded in a synoptic environment, thunderstorms internal dynamics can restrict a reliable nowcasting to very short lead-times (Doswell and Bosart, 2001). Depending on the thunderstorm system, the lead-time can fall down to tens of minutes. A better understanding of the driving processes and a well-set monitoring of carefully selected crucial storm parameters would help to improve the prediction skills of their non-linear behaviour.

Byers and Braham (1948) suggested that isolated storms undergo a typical evolution. Analyzing mainly airborne field measurements, they concluded that thunderstorms generally consist of one or more independent convective systems, which go through similar stages. Based on their observations of updraft and precipitation characteristics, they suggested a conceptual model of a typical thunderstorm life-cycle which distinguishes three main consecutive stages: cumulus stage, mature stage, and dissipating stage. This basic concept persisted over the last 50 years and has been continuously developed further by more detailed background knowledge and complemented by information derived from newly available measurement techniques.

The employment of conceptual models for thunderstorm prediction in operational nowcasting tools is among the attempts to improve the nowcast quality. The models are supposed to help to assess the current thunderstorm state and to predict the thunderstorm evolution by providing a priori more detailed informations about storm state and development. Beside the efforts to establish schemes which describe the general storm evolution, other studies aim to identify characteristic warning parameters, which predict storm-related hazards for the near future. The automated nowcasting system GANDOLF (Pierce et al., 2001), which is operated by the UK Met. Office, for example, employs an object-oriented conceptual model of convection with five stages (Hand, 1996) in the nowcasting of fluvial floods. Recently the Hong-Kong Observatory complemented its territorial rainstorm warning system SWIRL with local severe thunderstorm warnings by testing a four stage conceptual model for thunderstorm development (Yeung et al., 2007). Since it is a challenging and demanding task to assess and compare the

performance of different nowcasting methods, it could not be verified so far, whether the usage of conceptual models outperforms other existing nowcasting approaches.

Information about three-dimensional storm structure, derived from radar data and satellite data, already proved to be valuable for thunderstorm and lightning nowcasting. According to the actual cloud charging theory (Dash et al., 2001; Saunders, 2008), especially the onset of electrical charging processes in the cloud can be assessed and used as warning parameter for subsequent discharge activity (Bringi et al., 1997; Altaratz et al., 2001).

Despite promising observations in case-studies, up to nowadays the information about electrical discharges in thunderstorms has been mostly neglected in operational nowcasting tools. This is primarily due to a lack of data accessibility and/or insufficient data quality. In current nowcasting tools lightning information is primarily used as an additional data source to obtain a more comprehensive picture about thunderstorm stage and danger potential. Hereby, discharge events are attributed to previously-defined tracking objects (Soul et al., 2002; Yeung et al., 2007). Furthermore, lightning events are often only considered when they occur within the identified cell volume (Soul et al., 2002). This data usage distorts the information about the actual lightning activity of the storm object in the nowcasting application.

With the evolution of lightning detection systems, lightning information became especially interesting for severe storm monitoring in regions where lightning data are the only high-resolution data available to monitor deep convection, as for example over the Mediterranean Sea (Price et al., 2007), in the Alps (Bertram and Mayr, 2004), or for tropical cyclones over oceans (Demetriades and Holle, 2006). Efforts are made to establish a methodology that uses lightning data as a proxy to estimate storm strength and rainfall location and intensity with the aim to develop algorithms for short-term nowcasting of thunderstorm-related hazards based on lightning data alone. But because of the low lightning detection efficiencies in the areas of interest, these studies are restricted to persistent, long-living storm types with strong electrical discharges to facilitate a comprehensive storm tracking. Currently, no operational nowcasting tool explores operationally usable, comprehensive, and reliable in-cloud and cloud-to-ground discharge information with three-dimensionally resolved discharge locations.

Based on this background, the focus of this work is set to assess the usability of three-dimensionally resolved total-lightning stroke information, provided by the European VLF/LF *Lightning Detection Network* (LINET), for thunderstorm monitoring and short-term prediction. The benefit of the new data source has been tested both alone and in combination with information about ground precipitation, three-dimensional microphysical storm structure, and cloud-top temperature. The thunderstorm tracker ec-TRAM (Meyer et al., 2009) has been newly developed and verified for this purpose. Ec-TRAM identifies, tracks, and monitors thunderstorms in high temporal and spatial resolution by combining the information of independently tracked convective precipitation fields and electrically active storm regions. The pre-existing cell tracker rad-TRAM

(Kober and Tafferner, 2009) is used to identify and track heavy precipitation cells on the basis of high-resolution two-dimensional low-level radar scans. The algorithm li-TRAM has been newly developed to identify and track lightning cells on the basis of spatially and temporally clustered lightning frequency maps. The algorithm ec-TRAM assigns both cell types to new cell objects via spatial overlap and tracks the newly defined cells on the basis of previously identified radar and lightning-cell tracks.

A relational database, which comprises more than 500 storm tracks with about 20 500 separate cell entries, has been established based on data recorded in southern Germany during the summer of 2008. The life-cycles of two selected thunderstorms are investigated in detail in order to assess, on one hand, the information content and the reliability of the cell information provided by ec-TRAM, and, on the other hand, the information upgrade which can be achieved, if the ec-TRAM output is combined with other data sources. Therefore, the time series of cell parameters recorded by ec-TRAM are complemented by three-dimensional information about storm structure and hydrometeor formation provided by polarimetric radar data and by cloud top temperature derived from satellite data. The resulting temporal parameter evolutions and correlations are compared with previous studies and interpreted in terms of the actual state of knowledge about underlying physical processes. Furthermore, the principal existence of parameter correlations, which could be used to predict the storm potential and evolution, has been tested in statistical analyses based on the total data set.

The present work was embedded in the BMBF (Bundesministerium für Bildung und Forschung) project RegioExAKT (*Regional Risk of Convective Extreme Weather Events: User-oriented Concepts for Climatic Trend Assessment and Adaptation*). In the context of the project, the present work is outlined as a pilot study, which aims to develop and test an optimized, fast, and simple nowcasting method for convective thunderstorms, based on currently available data sources and with respect to the next generation of polarimetric radar composite data provided by the *Deutscher Wetterdienst* (DWD).

Chapter 2

Background of Convection Lifecycles and their Nowcasting

2.1 Cloud Electrification and Lightning Discharges in Thunderstorms

2.1.1 Global Electric Circuit

Under blue sky conditions a natural vertical electric field between the earth surface and the ionosphere exists (MacGorman and Rust, 1998; Rakov and Uman, 2003). The earth's surface is charged negatively and the air is charged positively, so that the resulting electric field vector is directed downward. The so called global fair weather field is about 100 V/m at the surface decreasing to zero in the conductive region of the ionosphere (Rakov and Uman, 2003). Because the atmosphere is weakly conducting, there is a permanent fair weather leakage current of the order of 1 kA. The fair weather leakage current would neutralize the charge on the Earth and in the atmosphere in approximately 10 min without a recharging mechanism (MacGorman and Rust, 1998). Thunderstorms are assumed to act as generator, so that worldwide thunderstorm activity maintains the persistent electrical background field by bringing a net negative charge to ground (MacGorman and Rust, 1998; Rakov and Uman, 2003). Beside its role as global atmospheric generator thunderstorms are considered to play another important role as global NO_x source. The lightning induced NO_x , termed LNO_x , is found to be especially important for the tropospheric chemistry (Höller et al., 1999; Schumann and Huntrieser, 2007; Huntrieser et al., 2008).

2.1.2 Electrification Processes and Electrical Structure in Thunderstorms

Several observations and cloud charging models suggest that thunderstorms develop en gross a tripolar structure (Williams, 1989; Saunders, 2008). The main negative charge centre is concentrated in a rather shallow layer at temperatures between approximately -5°C to -25°C . The more extensive main positive centre is located a few kilometers

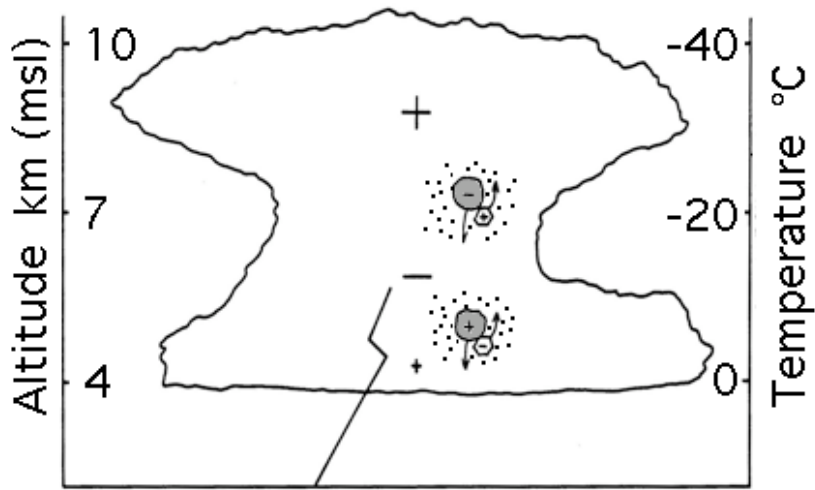


Figure 2.1: The charging mechanisms in a thunderstorm leading to the tripole charge distribution (after Saunders (2008)). Particle charging by graupel (grey) ice (white) rebounding collisions during droplet (black dots) accretion (riming). Graupel pellets charge negatively at low temperatures and positively at high temperatures in the updraft.

above the negative centre and the lower positive charge center is close to the 0°C level. Some studies also note, that the tripolar structure is a strong oversimplification of the actual thunderstorm structure (Stolzenburg et al., 1998; Carey et al., 2005). Field measurements reveal a much more complex composition with several extra charge regions and screening layers, but the principal tripolar structure remains mostly identifiable .

The *non-inductive charging theory* (NIC) (Takahashi, 1978; Dash et al., 2001; Saunders et al., 2006) fulfills the requirements to be the main driving process responsible for charge separation in thunderclouds. It is already stated that this theory has withstood the test of time (Saunders, 2008). The NIC theory states, that charge transfer happens in a certain layer within the updraft core, the so called mixed-phase-layer. In this layer ice crystals collide with riming graupel in presence of super cooled water droplets. Graupel and ice crystals are separated due to their different fall velocities. The graupel particles remain in the lower part of the cloud, building up the lower charge region, while the ice crystals are carried aloft in the updraft to form the upper charge region of the thunderstorm. It was found that the sign of the charge transfer is controlled by the relative diffusional growth rate of the interacting surfaces (Baker et al., 1987; Dash et al., 2001). Fast growth due to vapor deposition leads to a negative surface potential. The colliding ice surfaces tend to equalize their surface charges so that the faster grown surface loses negative charge. The charge exchange takes place in the melt water whereby the melted masses with the resolved charges are shared between the separating ice particles. Laboratory experiments found, that a charge reversal point exists, where the sign of the charge transfer changes (Takahashi, 1978; Saunders and Peck, 1998). The experiments also have shown, that the charge reversal point is a function of temperature and effective water content. A comparison between the different experiments suggests, that the charge reversal point depends strongly on the cloud conditions for particle

growth (Saunders et al., 2006). The latter finding implies that mixing between cloud parcels with different histories can accelerate or slow down the growth of ice crystals.

Figure 2.1 illustrates the charging mechanism and the development of a tripolar cloud structure. At higher altitudes with temperatures below the charge reversal temperature the graupel-ice-collisions lead to negatively charged graupel particles, which have faster fall velocities, while the positively charged ice crystals are carried aloft in the updraft. At lower altitudes with temperatures above the charge reversal temperature the charge separation contributes to the main negative charge center and the frequently observed positive charge center at the cloud bottom.

2.1.3 Lightning Processes and Their Discharge Characteristics

Lightning flashes serve to reduce spatial charge differences within a cloud, between clouds, or between cloud and ground. Lightning flashes can be grouped into two principal categories - those that strike the ground and those that do not. Flashes that contact to ground are called *cloud-to-ground (CG)* flashes. Flashes that do not, include in-cloud (intracloud), cloud-to-cloud (intercloud), and cloud-to-air discharges. Intracloud discharges occur within one thundercloud, intercloud discharges occur between different thunderclouds, and cloud-to-air discharges occur between a thundercloud and clear air. Within this notation all flashes that do not contact to ground are referred to as *in-cloud (IC)* flashes.

Lightning Initiation Theories

To the current state of knowledge there exists no generally accepted theory for the initiation processes, which initiate lightning discharges in thunderstorm. In the following paragraphs the two most prominent approaches and an interesting third approach, which tries to overcome the weaknesses of both theories by combining their strengths, are presented.

Conventional Breakdown Theory Dry air at surface pressure requires an electric field of about 3 MV/m (Rakov and Uman, 2003; Solomon et al., 2001; MacGorman and Rust, 1998) to initiate electrical breakdown. The magnitude of the field increases linearly with pressure (Solomon et al., 2001) reaching a value of about 2 MV/m at lightning initiation heights. The electric field is high enough to surmount collisional losses of the thermal electrons and generate a net energy flux from the bulk thermal particle population into suprathermal particles. Conventional breakdown does not require high-energy electrons in order to get started. No gamma-rays are emitted in this process. Conventional breakdown electrons are concentrated in a low-energy range up to 10 eV, they lose energy mostly to optical emission and the excitation of molecular nitrogen vibration levels (Gurevich and Zybin, 2005). Only a part of the upper energy tail effectively ionizes other particles (Gurevich and Zybin, 2005).

Runaway Electron Breakdown Theory The runaway-breakdown process requires a critical electric field of one tenth from that required for conventional breakdown process

(Solomon et al., 2001; Gurevich and Zybin, 2005). The low-energy electrons cannot start an electrical breakdown. Relativistic electrons are needed as trigger. For high energy electrons, the effective frictional force decreases with increasing electron energy until relativistic effects become significant. As a result high energy electrons are capable to trigger and sustain runaway acceleration under otherwise unfavorable conditions. The energy flows from energetic, relativistic electrons to thermal electrons (Gurevich and Zybin, 2005). Energy is lost mostly to ionization processes and almost no energy is lost to optical emission. Recombination occurs only for low energy electrons with energies less than 2 eV. In this process the number of free thermal electrons becomes large, about a million for each runaway electron under quasi-stationary condition (Gurevich and Zybin, 2005).

Combination of Conventional Breakdown and Runaway Electron Breakdown

Theory The conventional breakdown theory leaves the problem that up to now the electric fields observed in thunderclouds yield peak values, that are an order of magnitude weaker than the dielectric strength of air (Solomon et al., 2001; Petersen et al., 2008). In the case of the runaway breakdown mechanism, it seems not clear yet, how the diffuse discharges lead to the creation of lightning leaders (Petersen et al., 2008). So another approach suggests a combination of runaway breakdown mechanism and a hydrometeor-initiated positive streamer system (Petersen et al., 2008). This combined scenario suggests that a runaway breakdown event first generates a region of locally intensified fields, which are strong enough to support the generation of positive streamers on nearby hydrometeors and the transition into positive streamer systems. This positive streamer system results in a self-sustaining breakdown scenario with field strengths of about 1/3 of the observed field strengths.

The conventional breakdown model results in the formation of stepped leaders (see figure 2.2), which are supposed to be detectable as precursor of the actual lightning strokes in the VHF regime (see section 2.3.1). A more recent study found, that a large fraction of IC strokes is not preceded by observable stepped leaders and occurs in close time-coincidence with VHF emission (Betz et al., 2008). This finding supports an influence of fast electrons as described in the runaway electron breakdown model. The fast electrons are supposed to extend the breakdown mechanism over several hundred meters making the breakdown process visible in both, VHF and VLF, frequency regimes. Another study observed discrete, intense x-ray bursts in coincidence with the formation of the leader steps and dart leaders, which suggests a close correlation between the x-ray source and the stepping process (Dwyer et al., 2005). This finding further supports theories, where high-energy electrons are involved in lightning initiation. This study furthermore suggests that both leader types share common mechanisms.

Cloud-to-Ground Flashes

A ground flash occurs between the charge centers of the cloud and the ground. The question about what causes a cloud-to-ground (CG) flash is still an unsolved question of actual research. Why shall a leader channel leave the cloud bottom and propagate

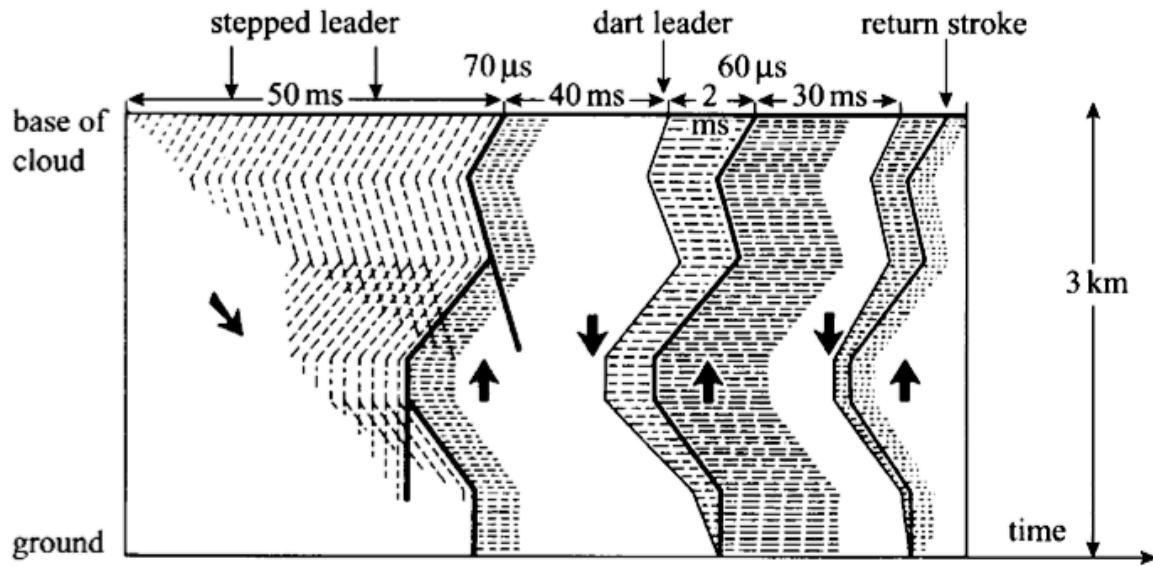


Figure 2.2: Time resolved luminous features of a cloud-to-ground flash as it would be recorded by a high-resolution camera. The time increases from left to right. The time scale is distorted (taken from Cooray (2003, chapter 4)).

to ground, instead of discharging the charge centers in the cloud directly? It is believed that, besides an electric field between the cloud bottom and the ground surface, which is high enough to sustain a leader propagation towards the ground, once the leader has been initiated, the CG flash has to be initiated itself by a small scale charge distribution. It has been observed, that CG flashes occur, when hail and graupel descent to the middle layers just below the main charge region (MacGorman et al., 1989; Lopez and Aubagnac, 1997; Carey and Rutledge, 1998). Lightning model studies (Mazur and Ruhnke, 1998; MacGorman et al., 2001) as well as VHF lightning mapping studies (Bruning et al., 2007; Wiens et al., 2005) suggest, that it is a small charge of opposite polarity beneath the main storm charge, that initiates the leader channel, which then, tapping the smaller charge pocket, propagates downwards to the ground.

When a ground flash transports a net negative charge into the cloud it is called *positive ground flash*, when it brings negative charge to earth it is called *negative ground flash*. Depending on the leader direction and of the net charge transfer four types of CG are distinguished, *negative downward*, *positive downward*, *negative upward* and *positive upward* CGs. The relative occurrence of all four flash types is not clear yet. The values differ strongly, depending on the measurement systems used, probably on the geographical region, and more. One study estimates, that about 90 % of the CG flashes are negative downward CGs, and about 10 % are positive downward flashes (Rakov and Uman, 2003). In the lightning data used for this study (see section 3.2.1), it is found, that 40 % of the CG events have positive amplitudes and 60 % negative amplitudes. The direction of the leader path cannot be determined. Generally it is believed that only a minor fraction of CG strokes have an upward propagating leader channel. It is further believed, that upward developing CGs are initiated by tall structures. In this

case a connecting leader is initiated, e.g. at the top of a tower, which propagates upward into the cloud. Dart leaders travel along this channel and initiate return strokes. As a consequence these flashes lack first return strokes initiated by stepped leaders.

Rakov and Uman (2003) cites, that the total duration of a CG flash ranges typically from 10 ms to 2 s, with a typical value of 300 ms, and the total charge lowered to ground ranges from 1 C to 400 C, typically around 20 C. The mechanisms, which are described in the following, are primarily based on observations with high-speed video cameras and photographs. In section 2.3.1 the visibility of the separate discharge components to other remote sensing systems is discussed. Beside the concept, which is described in the following, other concepts exist. The unidirectional leader concept, for example, is primarily used for return stroke modeling.

Several concepts exist to describe the CG process. The following description is based on observations of negative CG flashes and follows closely the description given by Cooray (2003, chapter 4). The description of Cooray has been complemented by other findings, which are separately cited. Some of the processes, described here, are also observed in other flash types. The graph in figure 2.2 illustrates schematically the temporal evolution of a negative downward CG flash on a respective time axis as it is visually observed with high-resolving optical measurement devices. The illustrated processes follow the description below.

A ground flash is initiated by an electrical breakdown process in the cloud which is called *preliminary breakdown*. Experiments in laboratory and the atmosphere support the idea of a double-ended tree structure, starting with a bi-directional streamer and continuing with their thermalized counterparts, the leaders (Williams, 2006). Because of different growing processes, the two ends of the tree do not develop in the same way. The breakdown field of a positive leader is about half of that for a negative leader so that the positive leader starts first. While the positive section of this leader pervades the negative charge region, it effectively supplies negative charge through the discharge origin to the negative section that then extends into the positive charge region. The positive leader end extends upward by virtue of the quasi-steady extension of a 'brush' of positive streamers at its head and radiates low energy, which is often below the threshold for detection. So called *recoil streamers* are found to originate at the positive leader tips and propagate towards the flash origin. They eventually make the negative leader process visible. The negative leader end extends downward in impulsive steps which can be well measured. Because of its stepped manner, the negative leader is called *stepped leader*. Both leader tips develop branches, the negative more than the positive.

As the stepped leader approaches the ground the electric field at ground level increases steadily. When the leader reaches a height of about a few hundred meters or less from the ground the electric field at the tip of grounded structures increases to a level that electrical discharges are initiated. These so called *connecting* or *attachment leaders* propagate towards the down-coming stepped leader. The gap is bridged as soon as one of them connects to the stepped leader. A wave of near ground potential travels then

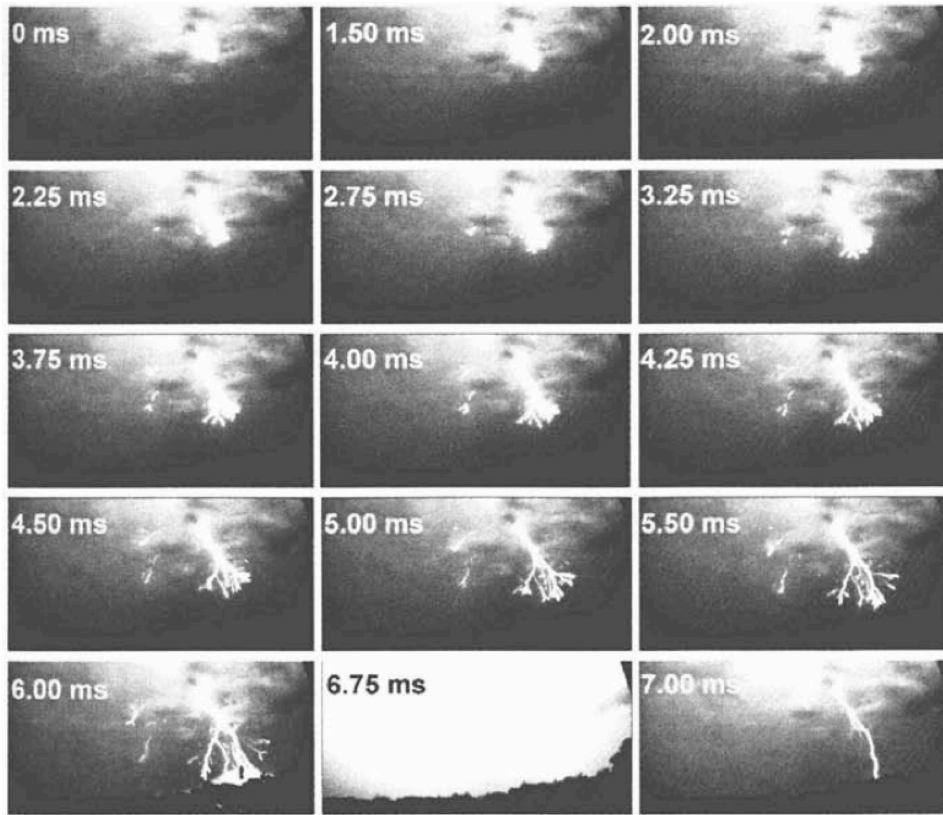


Figure 2.3: Time resolved luminous features of a cloud-to-ground flash recorded by a high-resolution camera with 4000 frames per second (taken from Betz et al. (2009b, chapter 9)).

along the channel upward towards the cloud with a speed of about 1/3 of the speed of light, illuminating the channel and neutralizing most of the charges in the channel. This ground-potential-wave is called *return stroke*.

Whenever the upward moving return stroke front encounters a branch, there is an immediate increase in the luminosity of the channel which is called *branch component*. Although the current associated with the return stroke tends to last for a few hundred microseconds, sometimes the return stroke current may not go to zero within this time but continue to flow at a low level for a few tens to a few hundreds of milliseconds. Such long duration currents are called *continuing currents*.

The approach of the first return stroke front at the cloud end of the return stroke channel leads to a change of potential in the vicinity of this point. This change in potential can initiate a positive discharge that travels away from the end of the return stroke channel. Again negative *recoil streamers* can start at the outer extremity of this positive discharge channel propagating the return stroke channel backward. It happens that these discharges die out before they reach the end of return stroke channel. They are called *K changes*. If they reach the return stroke channel while the return stroke channel still carries a continuing current, it will result in a discharge that travels towards the ground. Such discharges are called *M components*. When the M components reach the ground they do not initiate a return stroke but may be reflected from the ground.

If the return stroke channel is only partially conductive anymore and the current flow is already ceased the recoil streamers can initiate a new leader which travels towards the ground, the so called *dart leader*. A dart leader then initiates the so called *subsequent return strokes*.

Dart leaders travel preferentially along the old channel of the first return stroke but it is not uncommon for the dart leader to take different paths. In the latter case it ceases to be a dart leader turning into a new stepped leader and touching the ground at place, different from the first strike point. An observational study based on high-speed video analyses found the distance between such subsequent channels to be a few kilometers on average (Saba et al., 2006). In the same study about 80 % of negative CGs are composed of two or more subsequent return strokes, with an average of 4. Furthermore, 50 % of the multi-stroke CGs have multiple termination on ground. It was believed, that positive CGs normally have one, strong return stroke, only sometimes more (Cooray, 2003, chapter 4). Electrical activities in the cloud between subsequent strokes and after the final stroke are collectively called *junction processes* or *J processes*.

Cloud Flashes

In-cloud (IC) discharges typically occur between positive and negative cloud charges (Proctor, 1991; Lund et al., 2009) and have total time durations of about half a second, comparable to those of ground discharges (Uman, 2001). A typical cloud discharge transfers tens of coulombs of charge over a total spatial extent of 5 – 10 km. The lightning channel can be tilted or develop horizontally over long distances. Since most of the processes occur in the cloud, they are generally hidden from visible observations and can only be observed with other lightning detection systems (see section 2.3.1).

IC discharges have an 'electrodeless' nature. This means that, in contrast to CG discharges, they lack grounding. It is only obvious then, that IC discharges reveal other characteristics than CG discharges. They can be viewed to consist of three stages, an initial stage, an active stage, and a final stage. The scheme presented here and illustrated in figure 2.4 was developed by Cooray (2003, chapter 4) based on VHF radio imaging techniques (see section 2.3.1). It was found, that cloud flashes originate at higher altitudes and lower altitudes, while ground flashes generally originated at lower altitudes (Proctor, 1991; Lund et al., 2009).

The initial stage involves processes similar to the initial breakdown processes observed in CG flashes. The IC discharge starts as a bidirectional, more or less vertical leader tree (figure 2.4a). The vertical channel develops within the first 10 – 20 ms from the beginning of the flash. This channel is a few kilometers in length and develops with a speed of about $1.5 - 3.0 \times 10^5$ m/s. An increase observed in the electrostatic field after the channel was formed suggests, that negative charge is transferred to the upper levels along the vertical channel. At the end of this stage a conductive channel exists which connects the charge regions (figure 2.4b).

After the vertical channel has formed, an extensive horizontal branching in the positively charged upper level is observed which induces the active stage (figure 2.4c). The horizontal extensions are correlated to brief breakdowns at the negatively charged lower

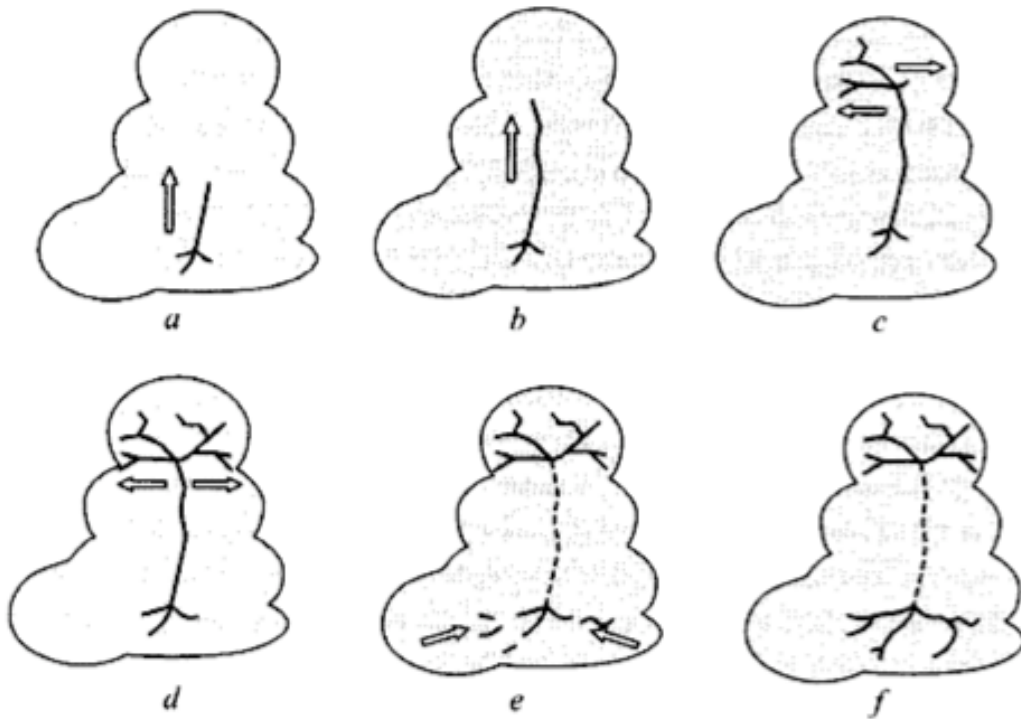


Figure 2.4: The individual stages of a cloud flash consist of an initial phase (a and b), an active stage (c, d and e), and a final stage (f). The arrows indicate the general direction of the discharge development (taken from Cooray (2003, chapter 4)).

levels. Discharges follow, propagating from the lower level to the upper level along the vertical channel. It is assumed that breakdown events, observed in the upper level, are initiated by the electric field changes due to the charge transfer from lower to upper parts of the cloud. Repeated breakdowns are observed for about 20 – 140 ms between the lower and upper levels along the vertical channel (figure 2.4d) which consequently transfer negative charge to the upper levels. These processes are classified as *K changes*. In the late active stage, which lasts about 140 – 200 ms, significant extensions of the lower channels in the negatively charged region take place (figure 2.4e). They appear retrogressively, which means that successive discharges, or *K changes*, often start just beyond the outer extremities of the existing channels and move back into and along these channels, continuously extending them further. These K changes transport negative charge from successively longer distances to the origin of the flash. Occasionally, they propagate to upper levels of the cloud flash. Occasionally the K changes initiate discharges that start at the origin of the flash and move away from it towards the initiation point of the K change.

The transition from the early stage to the late stage is thought to be associated with the loss of connection between the positive and negative sections (figure 2.4f). This cut off is probably caused by the decrease in the conductivity of the vertical channel. The late stage of the cloud discharges is also called the *J-type* stage, referring to the j-process in ground discharges. The various transient processes occurring during the late stage

when the leader contacts pockets of space charge opposite to its own are referred to as *recoil streamers* or *K-processes*. Just like K-changes rapid electric field variations are associated with K-processes.

Despite the efforts, which are done to explore the nature of lightning processes, no generally accepted theory to explain CG and IC lightning processes could be found yet. The explanations given here are only some state of the art, which have to be consistently revised, tested and upgraded by new findings. For example, the time-coincident occurrence of VHF and VLF/LF signals during the initial breakdown Betz et al. (2008) has not been considered here.

2.2 Conceptual Model for Thunderstorm Development and Evolution

2.2.1 Classical Life-Cycle Model

Over the last fifty years thunderstorm life-cycles were repeatedly investigated with continuously improving measurement techniques. It was found that thunderstorm development and evolution, when analyzed in detail, are complex processes depending on multiple aspects ranging from small scales to large scales. However, a basic concept of a thunderstorm life-cycle, which has been proposed by Byers and Braham (1948), proved itself useful over time. The conceptual model primarily bases on airborne measurements through thunderstorms. Byers and Braham concluded that thunderstorms normally consist of one or more independent convective systems or cells which go through similar stages. Based on updraft and precipitation characteristics they defined three well distinguishable stages with smooth transitions: the *cumulus stage*, the *mature stage*, and the *dissipating stage*. In the cumulus stage the cell is formed from an updraft of air. In this stage no rain has reached the ground yet. In the mature stage, rain is occurring and a large part of the cell consists of a downdraft, which characterizes the rain area. The updraft continues in parts of the cell in the low and intermediate cell levels and in all parts of the top levels. In the dissipating stage, downdrafts are throughout present, although weak upward motion is still apparent in the upper parts.

By adding other thunderstorm features a more detailed picture about thunderstorm evolution evolves. Charge separation starts in the mixed-phase layer in the presence of wet graupel, ice and super cooled droplets, as discussed in section 2.1.2, so a high reflectivity core is observed prior to the first electrical discharge (Bringi et al., 1997; Jameson et al., 1996; Dotzek et al., 2001; Altaratz et al., 2001). The charging efficiency depends, beside other factors, on the updraft strength and the updraft volume. It is expected that IC activity precedes the first CG event (Rakov and Uman, 2003) as the updraft increases and the storm becomes electrified. The forecast times spread between some minutes or less to up to tens of minutes strongly depending on storm type and climatological surrounding (MacGorman et al., 2006).

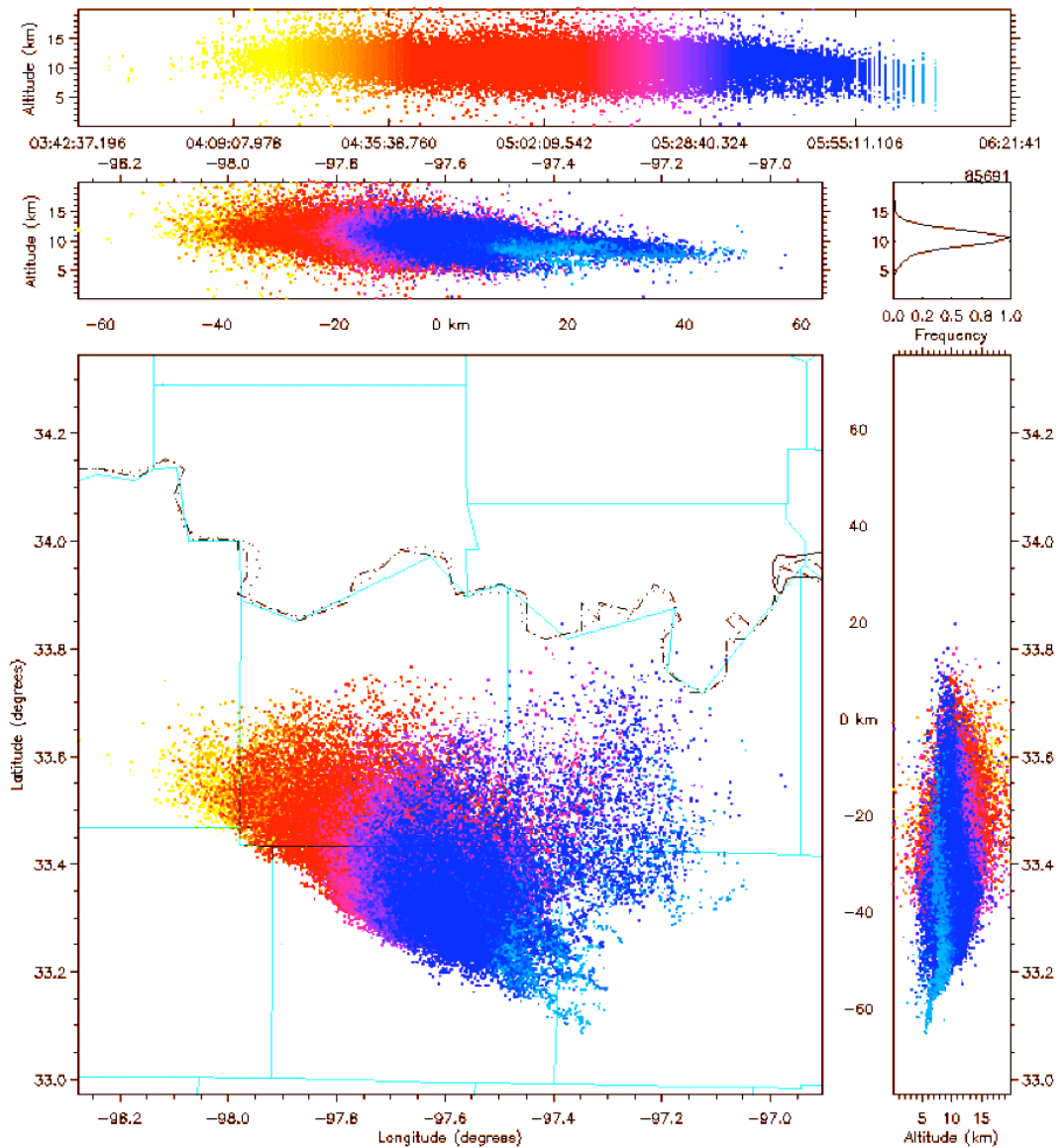


Figure 2.5: Three-dimensional VHF flash map of an isolated thunderstorm recorded by the LDAR II network on 25 May 2002 from 03:43 UTC to 06:22 UTC. The color indicates the time axis. Top panel: altitude versus time plot. Middle left panel: cross-section altitude versus longitude. Middle right panel: altitude versus source frequency. Lower left panel: plan view showing latitude versus longitude. Lower right panel: cross-section latitude versus altitude (taken from Demetriades et al. (2004)).

The electrical development of the storm is strongly connected to its dynamical and microphysical development, so that the time derivative of the total flash rate provides a signature of the growth and decay of the thunderstorm. The dynamical evolution of a Byers-Braham-Cell concept suggests, that the electrical evolution of a thunderstorm follows approximately an exponential growth-and-decay life-cycle and that the cell stage is reflected in discharge frequency.

The altitude of IC events is connected to the vertical extension of the cell part, where charge separation takes place, and those parts of the clouds, where charged particles are advected to. So, indirectly, the discharge height is related to cell stage and updraft strength. During the growing phase as the updraft establishes and the cell experience extensive vertical cell growth the maximum altitude of IC increases, shifting the altitude distribution to higher levels, until a maximum is reached. There it remains during the mature phase. During the dissipating stage, as the thunderstorm updraft decays and the cell core sinks, the maximum altitude decreases again. The change in altitude over time is shown exemplarily for an isolated thunderstorm recorded in Texas. A three-dimensional VHF flash map of the storm is presented in figure 2.5. The altering IC discharge height distribution with storm evolution can be clearly seen in the time plot and the cross-sections. It is also found, that storm cells with stronger updrafts have higher mean lightning flash origin heights than storm cells with weaker updrafts (McCormick et al., 2002). The change in the mean height of the IC discharge location could therefore be used as indicator for storm growth and storm strength.

The electrically active phase may have a duration lasting from a few minutes to hours depending on the storm type. It is found that the total amount of lightning and peak flash rates associated with a storm correlate with the storm intensity and parameters such as storm size and height (Williams, 1985; Price and Rind, 1992)), and duration and environment (Goodman and MacGorman, 1986; Fehr et al., 2005).

To summarize the aspects mentioned here and complementing the picture by the findings of previous studies the following conceptual scheme is proposed:

5 – 10 min after the detection of a 35 – 40 dBZ radar echo aloft, which correlates with onset of strong convection, the cloud electrification starts (Bringi et al., 1997; Jameson et al., 1996; Altaratz et al., 2001; Carey and Rutledge, 1998). Another 5 – 10 min later electrical activity starts within the cloud (Bringi et al., 1997; Jameson et al., 1996; Altaratz et al., 2001). As the updraft increases the reflectivity core experiences vertical growth and the maximum and mean IC discharge height increases (Demetriades et al., 2004). Few minutes later first CG events occur (Demetriades et al., 2004; Bringi et al., 1997; MacGorman et al., 2006). This is supposed to happen about 35 min after the strong convection started in accordance with the convective time scale which is the estimated time it takes for a lifted air parcel to rise from its low-level origin to equilibrium level. The lightning activity reaches its maximum about the same time, when the radar echo core reaches its peak height and peak volume (MacGorman et al., 1989). The peak rain rate lags the peak lightning activity by about 5 min (Carey and Rutledge, 1996) because of the time the storm precipitation core needs to reach the ground after the storm updraft has diminished. As the cell enters the dissipation stage the radar reflectivity core aloft ceases and starts to sink. In correlation to the evolution of the radar reflectivity core the IC mean discharge height sinks (Demetriades et al., 2004), and discharge activity decreases. The precipitation intensity at ground lightens but might still go on for some time after the electrical discharge activity has finally stopped.

2.2.2 Organization Forms of Thunderstorms

Roughly three basic types of thunderstorms are distinguished. Single cells, multi-cells, and supercells. Primarily the factors buoyancy, wind shear, and low-level forcing determine the final organization form. The relationships explained in the previous section should be true as long as independent cell cores are observed. For organized structures, it is stated that the growing stage and the dissipating stage follow the conceptual model, but probably on different time scales (Goodman and MacGorman, 1986), whereas the mature stage differs. The life-cycle of a multi-cell system might be considered as the superposition of several time-lagged single cell systems. The mature state of supercells is supposed to be elongated and possibly fluctuating, depending on the synoptic feeding.

Single Cells The class of single cells comprise cells that appear scattered and unorganized. Single cells mainly develop in environments with little to moderate buoyancy (little CAPE and little CIN) and weak wind shear. They develop independently, are small, short-lived with lifetimes of about one hour, they are poorly organized and likely to follow a characteristic life-cycle described in 2.2.1. Single cells may be vigorous with intense lightning activity, often accompanied by strong winds and heavy precipitation. But they rarely produce extreme hazards like large hail or tornadoes.

Multi-Cell Systems Multi-cell systems appear as cell clusters or organized in line formations, the so called squall lines. Unlike single cells the cells in multi-cell systems influence each other. The system consists of several cells in various stages of development. Every cell component is short lived and runs through a life-cycle just like single cells. The multi-cell components interact in a way that the cold outflow of older cells may trigger new cells, which elongates the lifetime of the cell system up to several hours. Squall lines are known to have strong hazardous potential being associated with heavy rain, hail, and wind gusts.

Supercells Supercells are characterized by a sustained deep and rotating updraft. They are typically severe storms with strong horizontal wind gusts, large hail, flash floods and sometimes tornadoes. They can live over several hours but in contrast to multi-cell systems, they consist of one single cell which has formed a self-sustaining dynamic entity.

Under favorable conditions, severe storms often do not follow the mid-level winds but propagate either to the right in anti-cyclonic (clockwise) wind shear or to the left in cyclonic (counter-clockwise) wind shear, depending on the direction and amount of crosswise vorticity. Those cells are called right mover or left mover, respectively. In environments with high speed wind shear (directional or non-directional) a dynamically induced storm splitting can occur, where one cell continues as left mover and the other one as right mover (Klemp, 1987).

2.3 Data Sources and Measurement Principles

2.3.1 Lightning Monitoring Methods

A complete lightning discharge is composed of a number of different successive processes as explained in detail in section 2.1.3. Every flash component has different physical properties in terms of space and time scales, discharge propagation, radio frequency radiation type, and current properties. Different monitoring methods can assess different flash components. But as a multi-scale physical process, it is not possible to assess all lightning phases with one measurement device. Charge accelerations in conductive channels can be assessed by monitoring the radiated electro-magnetic fields. The redistribution of charge in the cloud can be concluded from changes in the static E-field. If channels emerge from the cloud, optical observations with high-speed video cameras or photo cameras can be used to determine channel geometry, extension speed and other lightning features. Cloud tops illuminated by lightning can be observed from satellites.

Lightning Monitoring Based on Radio Wave Signals

Lightning processes radiate over a wide frequency range spanning from UHF to ULF. A complete list of the commonly used radio frequency bands is given in appendix A.1. The radio frequency bands The lightning induced electromagnetic signal is called *radio atmospheric signal* (sferic). Figure 2.6 gives an overview of lightning related radiation fields and their measuring methods. The emission sources are different for different frequency regimes. An overview of the radio wave frequency bands and their abbreviations is given in section A.1.

UHF/VHF frequencies are attributed to discharge lengths of less the 10 m. Breakdown and leader processes can be investigated in this frequency regimes. Negative leader processes can be monitored in VHF mapping systems, but positive leader processes are almost invisible for mapping systems due to their continuous and 'calm' nature. Mostly

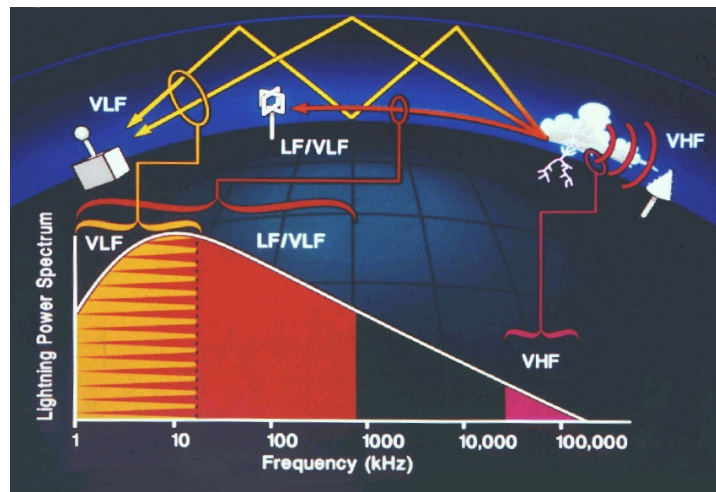


Figure 2.6: Overview of lightning induced electro-magnetic frequencies and their measurement methods (taken from Cummins and Murphy (2009)).

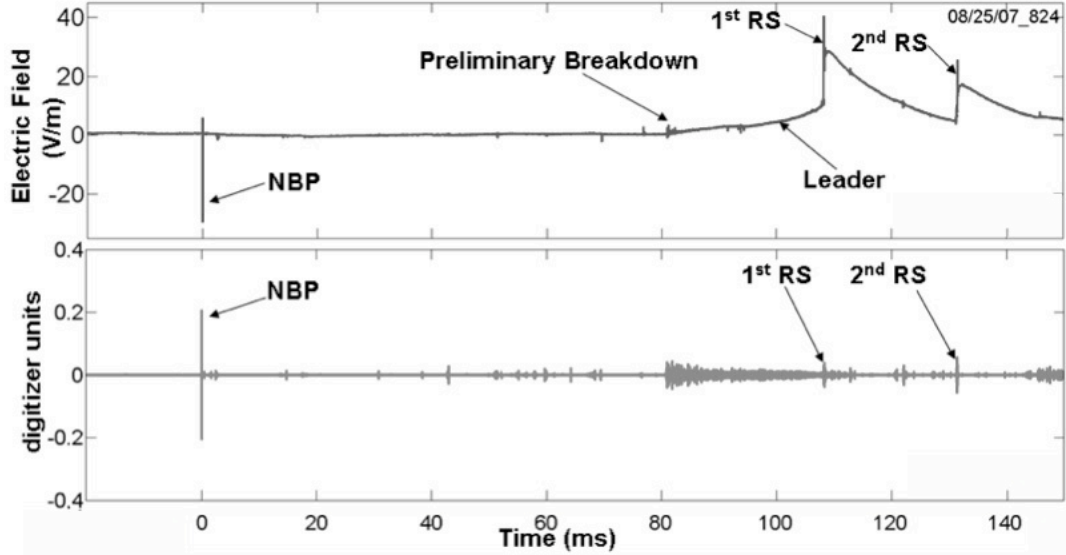


Figure 2.7: Wide-band E-field and HF (5 MHz) signatures of a narrow bipolar pulse (NBP) followed by preliminary breakdown processes and a negative CG (taken from Nag et al. (2007).)

recoil streamers, radiating in the VHF regime, reveal the streamer paths. Lightning processes with discharge lengths of some 100 – 1000 m radiate primarily in the VLF/LF regimes. Return strokes and strong IC current surges activity with longer discharge lengths can be recorded in this frequency regime.

According to theory the VLF/LF signal in a typical CG flash occurs several milliseconds after the leader phase seen by VHF systems. And a typical IC flash is supposed to show current pulses detectable by VLF/LF sensors in later stages of the flash (Rakov and Uman, 2003; Betz et al., 2007; Shao and Krehbiel, 1996). But a recent study found, that about 50 % of initial breakdown processes start with a strong discharge step, producing both, VLF/LF and VHF signals (Betz et al., 2008) (compare figure 2.7). In this study it has also been observed, that at the beginning of subsequent breakdowns during one flash, near time-coincident VLF/LF and VHF signals occur.

Figure 2.8 and figure 2.7 show signal pulse trains of negative CG strokes with preceding cloud activity recorded on different frequency regimes with different measurement devices. Figure 2.7 compares the pulse trains monitored in the wide-band E-field and in the VHF system. The example shows a narrow bipolar pulse (NBP), a strong current surge in the cloud, which precedes a subsequent CG stroke. The NBP is visible in both frequency regimes. Furthermore, it can be seen that systems operating in the VHF regime are sensible to small scaled preliminary breakdown and leader processes whereas the wide field antenna is mostly sensible to the return strokes. Figure 2.8 shows a pulse train recorded by LINET in the VLF/LF regime. The preliminary breakdown pulses are clearly visible during the first 600 μ s, but the subsequent stepped leader is almost

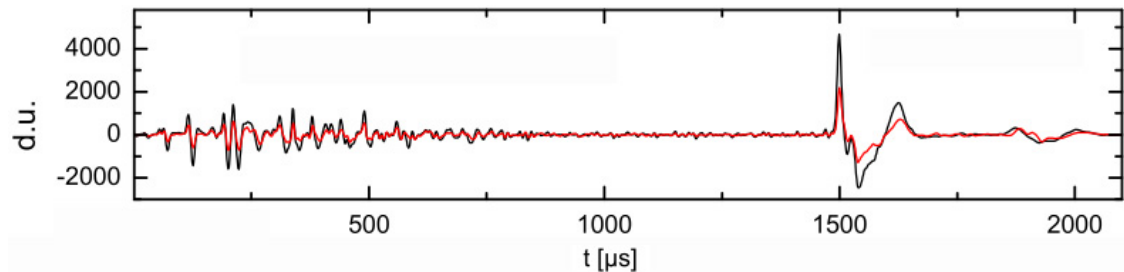


Figure 2.8: Signal pulse train of preliminary breakdown processes with a subsequent negative return stroke recorded in the VLF/LF regime with LINET System (taken from Schmidt (2007)).

invisible to the system. The return stroke appears as a pronounced peak after 1.5 ms.

Lightning-induced sferics are attenuated while they propagate over finitely conducting ground (Cooray et al., 2000). The main reason is dispersion. Different electrical conductivity of the ground surface have different attenuating properties. Studies have shown that higher frequencies suffer more selective attenuation. As a result the signal wave form and the total amplitude change while the signal propagates through the atmosphere (Cooray, 2007). The propagation effects depend on the electrical ground properties over which the electromagnetic field propagates. The propagation effects on radiation fields coming directly from cloud flashes differ from those coming from return strokes in ground flashes. Radio signals emitted by return strokes in ground flashes travel as ground waves directly influenced by the ground conductivity. Radio signals originating in the cloud travel the first part as space wave less influenced by the ground impact. But also if perfect conductivity is assumed transversal magnetic modi within the Earth-ionosphere wave guide attenuate the signal reducing preferentially high frequencies (Dowden et al., 2002).

Strong signals with lower frequencies can propagate reflected at ionosphere and ground over long distances of several 100 – 1000 km, depending on the peak amplitude and the frequency. Electromagnetic waves with frequencies below 100 Hz can propagate with little attenuation around the globe, guided within the Earth-ionosphere cavity. Constructive interference of these globally circum propagating electromagnetic waves results in Earth-ionosphere cavity resonances, so called Schumann resonances (Sentman, 1996).

Lightning Localization Methods

TOA - The Time Of Arrival Method The *time of arrival* (TOA) uses the differences of the sferic arrival times at differently located sensors to determine the source location. Figure 2.9b presents a scheme to illustrate the method. A point source for the signal is assumed. To locate the sferic source the arrival times from at least four stations are needed. Two stations give one time difference and a hyperbola can be determined. Three stations give two independent time differences and two hyperbola can

be constructed which usually have two intersections. Sometimes one of the intersections can be excluded if it is found to be unreasonably far away. To determine the exact location at least four stations must have recorded the wave front passage. The pure arrival time method varies the incident location and the arrival time in its fitting routine. The *arrival time difference* (ATD) method varies only the incident location in a fit routine. Since the height has to be positive, the height information is already included in the solution. If a separate parameter is introduced into the fit sum the emission height can be calculated, based on the four recorded wave transit times.

MDF - The Magnetic Direction Finder Method The *magnetic direction finder* (MDF) is one of the earliest methods to determine event times and locations of atmospheric discharges. The incident angle of the passing wave front at a sensor is used to determine the direction and the propagation path of the source. A scheme presented in figure 2.9a illustrates the method. The exact event location and time are found by calculating the intersection of two or more propagation paths. Under favorable conditions, if the event is not situated near the base line of the sensors, only two sensors are needed to locate the event. The so called base line error increases the closer the event is located to the sensor connecting line. In the worst case, if the event is located on the connection line, no intersection exists at all. In the calculation with two sensors two solutions exist, due to the spherical earth surface. Generally the nearer intersection is more reasonable and the farther one can be rejected. For three or more stations the most likely lightning location can be calculated iteratively by minimizing a fit sum. The event location is varied in order to optimize the fit sum.

The Interferometric Direction Finding Method Phase comparison base line interferometric arrays are used for direction finding (DF). The angle of arrival is measured in the interferometer by measuring the phase difference of signals received by two spatially separated antennas. The measured phase difference is directly related to the angle of arrival. Figure 2.9c illustrates the method in a simplified scheme. A system with three antennae, normally arranged in an isosceles triangle, can determine both the horizontal and the vertical incident angle. The baseline of the triangle varies from 1 – 300 m (Schmidt, 2007), depending on which frequency band the system operates. To avoid ambiguity the maximum distance between two antennas has to be half the wavelength. To cover larger bandwidths without ambiguity a multiple antenna array with non-uniform spacings is used. At least two of such systems are required to locate an event in three dimensions.

TOA based methods can assess the discharge location, and estimate the polarity, the peak current and the charge transfer. But the method needs distinctive points in the signal signature, like peaks and zero crossings, which are representative for the whole pulse train. The interferometric direction finding method can process long ongoing sequences without distinctive signal structure. But the method does not assess direct information about polarity, peak current and charge transfer.

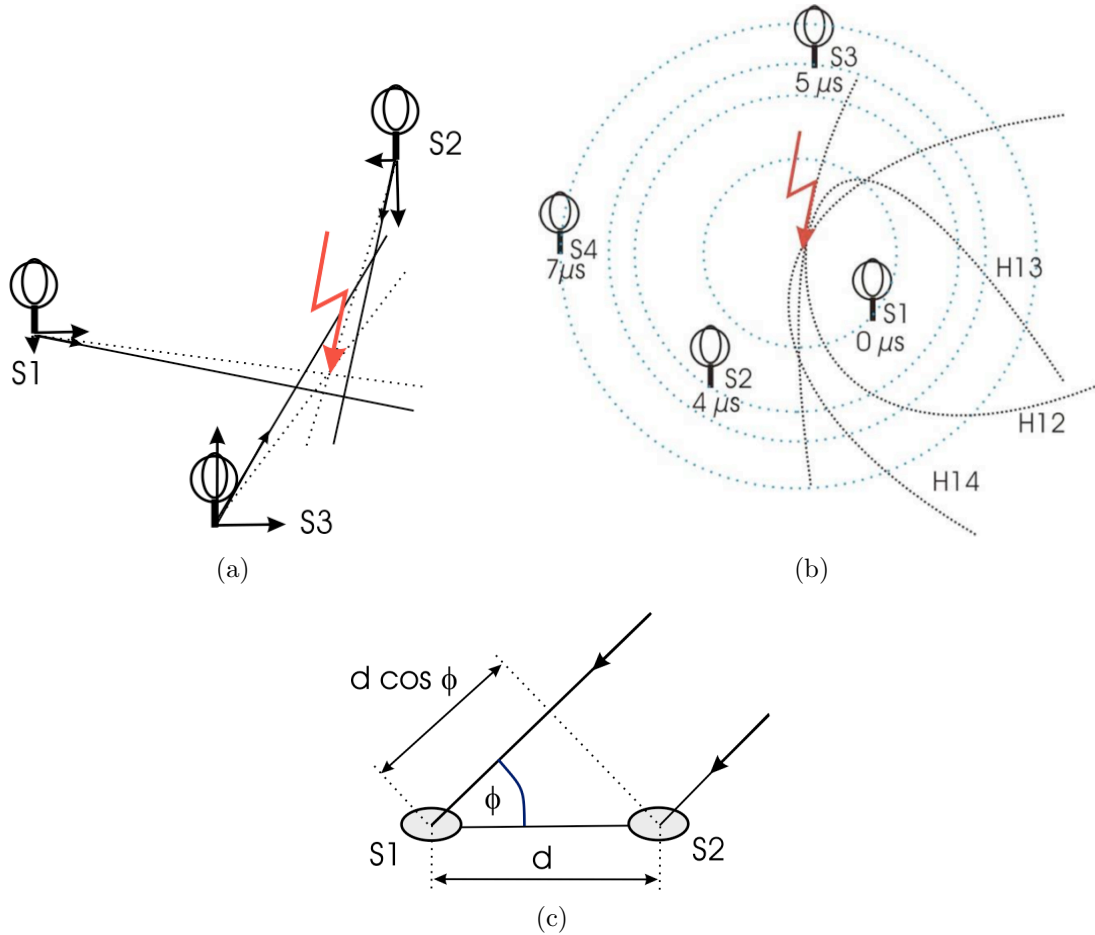


Figure 2.9: Schemes of lightning localization methods (taken from Schmidt (2007)).
 (a) MDF method with three stations. Indicated are the discharge source and the determined propagation paths which enclose an area of possible source locations. (b) TOA method with four antennas. Indicated are the three hyperbolas (H12, H13, H14) which are calculated from the arrival time differences related to the arrival time of station one (S1) and the source location. (c) Radio-interferometric method with two antennas. Indicated is the incident wave front and the important parameters.

Two and Three Dimensionally Resolving Lightning Localization Systems
 The most grave error sources for ground based lightning location networks are site anomalies, non-vertical lightning channels, background noise, and signals reflected from the ionosphere. The frequency regime and the lightning localization method define which parts of the lightning process can be monitored. Beside the method, the sensor spacing and the sensor constellation used to locate the discharge source determine the location accuracy and the detection efficiency. The bandwidth of currently operated ground-based systems ranges from long-range detection systems operated in the ULF, VLF, and LF regime to high-resolving VHF mapping systems.

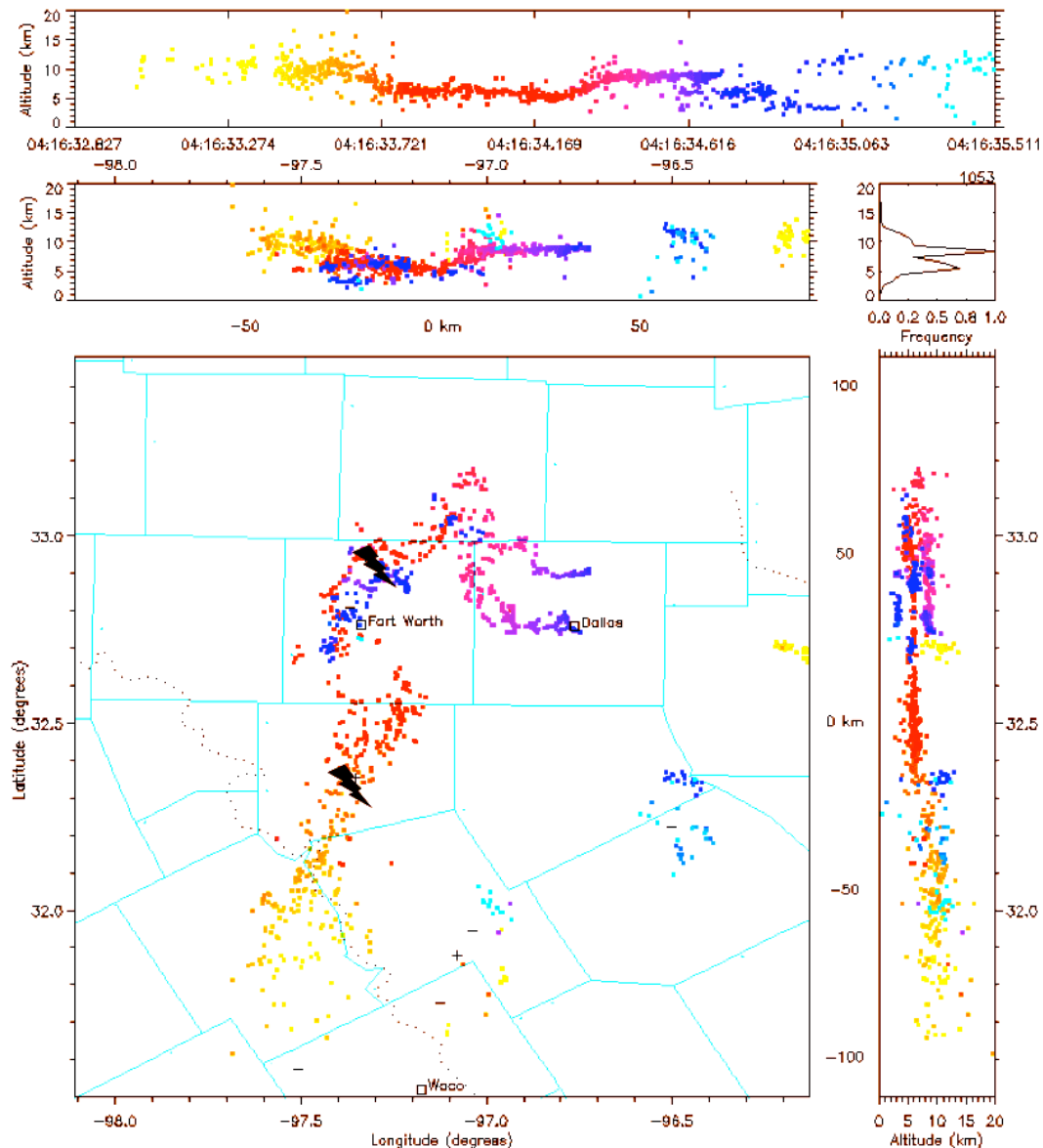


Figure 2.10: Three-dimensional VHF flash map recorded by the LDAR II network on 13 October 2001 at 04:17 UTC (taken from Demetriadis et al. (2004)). The color indicates the time axis. Top panel: altitude versus time plot. Middle left panel: cross-section altitude versus longitude. Middle right panel: altitude versus source frequency. Lower left panel: plan view showing latitude versus longitude. Lower right panel: cross-section latitude versus altitude

Two-dimensional lightning monitoring is rather simple. The distance from the sensor to the signal source is calculated as its radian multiplied by the earth radius. Long range lightning localization systems, which operate in the VLF and LF or in the ULF regime (Cummins and Murphy, 2009), are bound to use two-dimensional calculations because of their large base-lines. The extension of the lightning channel is simplified to a point source in the calculation and the discharge height is ignored. Since the VLF/LF

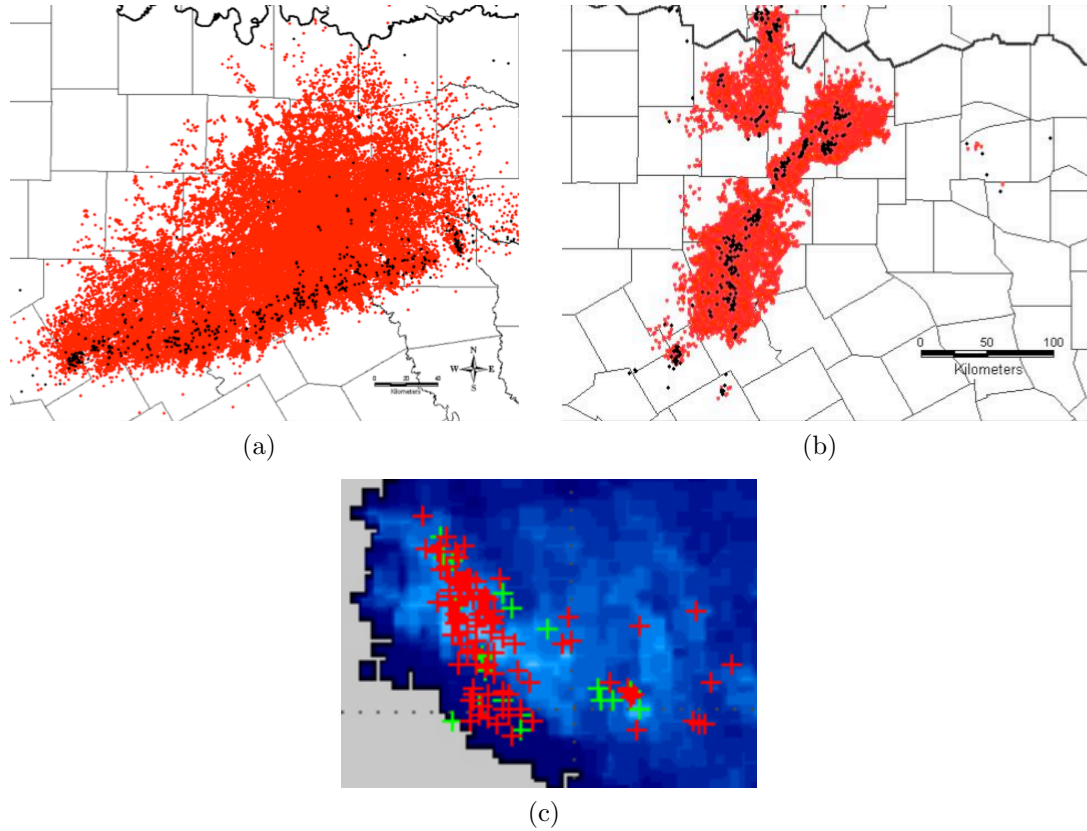


Figure 2.11: Illustration of information content of different lightning localization methods. Overlay of LDAR II VHF IC (red) and NLDN VLF/LF CG discharge sources (black) of a thunderstorm with (a) and without (b) stratiform region recorded on 13 October 2001 and on 15 June 2001, respectively (taken from Demetriades et al. (2004)). (c) LINET VLF/LF IC (red crosses) and CG (green crosses) discharge sources of a thunderstorm without stratiform region recorded in south Germany in 2008 (own illustration).

signals do not suffer strong attenuation (see section 2.3.1) while propagating through the atmosphere, the sensor spacing can be rather generous, and is finally defined by the required detection efficiency and location accuracy.

Three-dimensionally resolving lightning monitoring systems need the direct incoming electromagnetic signal wave to retrieve the discharge height information. This requirement limits the sensor spacing due to the curved earth surface. At a distance of 100 km a sensor cannot see a point below 800 m, at a distance of 200 km a point below 3.1 km, and at distance of 500 km a point below 19.5 km. With few exceptions three-dimensionally resolving systems operate in the VHF regime. VHF mapping systems can locate specific discharge features with an accuracy of 10 – 1000 m, depending on technique and feature type. They can assess information about the space-time behaviour of individual flashes, and from that derive information about the spatial extent of the charged region of a large thunderstorm. The systems provide information about fast leader processes that

are generally not well-represented in VLF/LF data. But they cannot directly locate CG return strokes or IC strokes, or estimate their peak current. In comparison with VLF/LF systems, the high resolution VHF mapping systems require much shorter sensor spacing with baselines of 10 – 40 km and high data processing capabilities. VHF mapping networks cover only small areas with about 100–200 km in diameter (Cummins and Murphy, 2009). Three-dimensionally resolving systems operating in the VLF/LF regime need sensor spacings less than 200 km. They do not achieve the high time-space resolution of VHF operating systems but they can cover large areas. Employing a TOA based method they can assess the discharge location, and estimate the polarity, the peak current and the charge transfer. In figure 2.11, which is discussed later in this section, characteristic features of different lightning localization methods are compared in discharge maps.

If three-dimensional resolution cannot be achieved to identify IC discharges, either if the system was not configured for this purpose or the sensor spacing is too wide, it is a common method to apply a combination of wave form and amplitude criteria, to have at least a guess about the IC to CG flash ratio. But this method has problems to classify lightning events correctly, especially if the cloud pulses are bipolar with nearly equal positive and negative peak amplitudes (Cummins and Murphy, 2009).

The best method to determine IC discharges consistently, reliable, and comprehensively over a large area is an unsolved, challenging, and strongly discussed issue.

Figure 2.10 and figure 2.11 give a comparison of the information content provided by VHF operating and by VLF operating systems. Figure 2.10 presents a highly resolved three-dimensional flash map recorded by the VHF system LDAR II. The discharge path can clearly be seen indicated by the color and the time plot. Indicated by black lightning bolts are the two CG signals the VLF network NLDN recorded. Figure 2.11 gives another comparison between the characteristics of different lightning localization systems. In figure 2.11 lightning activity maps recorded by different lightning detection systems of a thunderstorm complex with and without a stratiform region are shown, respectively. The different detection characteristics can clearly be seen. Figure 2.11c shows a lightning activity map recorded by the VLF/LF system LINET. LINET discriminates operationally between IC and CG events by calculating the discharge height. Although the data density is not so high compared with the VLF data, the area coverage of the total electrical discharge (TL) activity is obviously better than it would be with CG information alone.

It has been suggested in previous studies (Boccippio et al., 2001; MacGorman et al., 2006), that the lightning frequency in the cloud generally exceeds the number of CG strokes. The range depends strongly on the capabilities of the measurement devices. An obvious advantage of efficient TL monitoring is, that the TL lightning activity covers a larger area. Storms can be detected more quickly and reliably, simply due to the increase in data amount. This can be seen in the lightning maps presented in figure 2.10 and figure 2.11. Moreover, by monitoring in-cloud activity, areas can be identified where the threat of CG strokes is high although they did not occur yet. Such endangered areas are,

for example the area under stratiform rain regions (see figure 2.11a), which are attached to active thunderstorms or the area under extensive thunderstorm anvils (Holle et al., 1993; Carey et al., 2005; Lund et al., 2009).

It has been seen that the information about in-cloud activity provides a more reliable indication of the storm growth rate and storm intensity than CG stroke information alone (Demetriades and Holle, 2006). Other studies found, that severe storms have especially high IC to CG ratios and sometimes even no CG discharge is observed during the whole lifetime (Williams et al., 1999; Wiens et al., 2005).

An accumulated occurrence of positive polarity CGs is also observed from thunderstorm anvils, storms which become severe producing mesocyclones, large hail, or tornadoes (Tessendorf et al., 2005; Bonelli and Marcacci, 2008).

Lightning Monitoring Based on Optical Signals

Long-term global observations over of TL activity can be done via satellite based lightning sensors. In recent years the NASA Optical Transient Detector (OTD (Boccippio et al., 2000), onboard OV-1, flash detection efficiency approximately 40 – 65 %, horizontal resolution 10 km over $1300 \times 1300 \text{ km}^2$) covered latitudes between $\pm 75^\circ$. Currently the Lightning Imaging Sensor (LIS (Christian et al., 1999), part of the TRMM Mission, flash detection efficiency approximated with 90 % at nighttime and less at daytime, horizontal resolution 3 – 6 km over $550 \times 550 \text{ km}^2$) provides lightning data for latitudes between $\pm 35^\circ$. Both sensors are non-geostationary providing valuable information about lightning activity on a global scale. But their lightning data are useless for the tracking of individual thunderstorms, since a specific location is only observed for a couple of minutes per day with significant time lags in the data. With the next generations of GOES-R and MTG it is planned to launch geostationary lightning mappers, which will open a new dimension to global and local lightning monitoring.

2.3.2 Radar Systems

Radar Reflectivity

Radar devices used for weather observations operate on the theory of elastic light scattering. They emit pulses of electromagnetic waves of a well-defined wave length and polarity. On the propagation path hydrometeors such as rain drops, hailstones, or graupel become excited mainly in parallel to the polarity of the incident electromagnetic wave. Acting like electrical dipoles the hydrometeors themselves emit secondary electromagnetic waves mainly of the same wave length and polarity as the primary wave. With each pulse the radar emits, a radar resolution volume is illuminated and energy is backscattered. The radar then measures the backscattered energy of secondary electromagnetic waves. The received signal contains information about the bulk particle properties within the radar resolution volume.

In the case of pure Rayleigh scattering the cross-section σ of a particle can be expressed explicitly as a function of the agitating wave length λ (Doviak and Zrnić, 1984), the equivalent droplet diameter D_e , and the absolute index of refraction $|K|$ with

$$\sigma = \pi^5 |K| \frac{D_e^6}{\lambda^4}, \quad [\sigma] = \text{mm}^2. \quad (2.1)$$

For atmospheric air the Rayleigh approximation is satisfied if the condition $D_e \ll \frac{\lambda}{16}$ is fulfilled.

On the condition of Rayleigh scattering the principal radar equation for the mean power P_r received at the antenna can be simplified after Battan (1973) to

$$\overline{P_r} = C \frac{|K|^2}{r^2} \sum_{Vol} D_e^6, \quad [\overline{P_r}] = \text{W} \quad (2.2)$$

where C is the so called radar constant. The radar constant includes the information about the radar characteristics, namely the transmitted power, the antenna gain, and the wavelength of the transmitted electromagnetic wave, as well as the numerical constants. The summation in equation 2.2 is done for scatterers in the illuminated sample volume and is referred to as the reflectivity factor z . The reflectivity factor z can be expressed as (Meischner et al., 1995)

$$z = \frac{1}{V} \sum_{Vol} D_e^6 = \int_{Vol} N(D_e) D_e^6 dD_e, \quad [z] = \frac{\text{mm}^6}{\text{m}^3}. \quad (2.3)$$

The last term in equation 2.3 evolves the discrete and disordered summation over all particles within the illuminated sample volume to an integral over the product of particle size D_e and particle size distribution $N(D_e)$. This step allows to relate the radar reflectivity factor to the physical characteristics of the precipitation within the illuminated volume. Since the reflectivity factor covers a wide range, it is common to use its logarithmic expression. The *radar reflectivity* Z is defined as (Meischner et al., 1995)

$$Z = 10 \log_{10} \left(\frac{z}{\text{mm}^6/\text{m}^3} \right), \quad [Z] = \text{dBZ}. \quad (2.4)$$

Z is the logarithm of the ratio of the reflectivity factor to the unit radar reflectivity of $1 \text{ mm}^6/\text{m}^3$ and measured in *dBZ*.

Conventional and Polarimetric Radar Quantities

The *radar reflectivity* Z is the radar quantity, which is easiest to assess and therefore most common in operational radar applications. Z is also called conventional radar parameter. The total power backscattered by horizontally polarized incident waves is used to calculate Z . The technical demands are rather simple and signal processing easy in comparison to polarimetric radars but the information content is limited. It can be seen in equation 2.3 that the radar reflectivity factor is proportional to the particle density and to the power of six to droplet size. Only some few big, wet particles among a majority of small droplets within the illuminated sample volume will distort the signal to high values. The predominant hydrometeor type can not unambiguously be determined based on radar reflectivity alone, because the same backscattered signal

might arise from some few wet hail stones as well as dense rain.

Falling rain drops have more or less oblate ellipsoidal shapes. The bigger the droplet the more pronounced is the ellipsoid. The electromagnetic behaviour of an ellipsoid can be described as two crossed dipoles which are aligned with the principal axes of the particle projected onto the plane of polarization. In general, hydrometeors are canted with respect to the plane of polarization so that both dipoles are excited by a purely horizontally or vertically polarized incident plane wave which means hydrometeors depolarize the incident wave. They emit secondary radiation along both principle axes so that the backscattered electromagnetic field has two orthogonal components even if the incident electromagnetic field had only one.

In contrast to the conventional radar, a polarimetric radar can control the polarization state of the transmitted and the received electromagnetic waves. Generally, the horizontal and the vertical planes are used. Since most precipitating particles are not spheroidal, they appear different in the two polarization planes. Polarimetric parameters are, beside others, dependent on the size, shape, thermodynamic phase, and falling behaviour of the particles in the radar volume. The combined information of different polarimetric variables allows to deduce the predominant hydrometeor type within the illuminated sample volume, so that a picture of the actual microphysical structure of the meteorological target object can be retrieved.

The following notation will be adopted for polarimetric variables: Z_{HV} refers now to a radar reflectivity where the primary pulse was emitted in the horizontal plane and the backscattered return signal was measured in the vertical plane. The backscatter coefficient σ_{HV} refers to the ability of the scatterer to emit signals in the vertical plane, when the agitating signal is horizontally polarized.

Differential Reflectivity - ZDR The *differential reflectivity* (ZDR) is defined after Seliga and Bringi (1976) as

$$Z_{DR} = 10 \log_{10} \left(\frac{Z_{HH}}{Z_{VV}} \right) = 10 \log_{10} \left(\frac{\int_{Vol} \sigma_{HH} N(D_e) D_e^6 dD}{\int_{Vol} \sigma_{VV} N(D_e) D_e^6 dD} \right), [Z_{DR}] = \text{dB}. \quad (2.5)$$

ZDR can be considered as a measure of the reflectivity weighted axis ratio of hydrometeors within the radar sampling volume. It is a measure of the preferred orientation of non spherical hydrometeors. It becomes positive, if the precipitating particles are preferably horizontally aligned and negative, if they are preferably vertically aligned. Regarding precipitating particles, positive values are caused by the elliptical shape of large raindrops, values around zero are caused by canted or tumbling ice and graupel particles, and negative values can arise from large, oblate hail stones which are mostly aligned around the vertical axis.

The last term in equation 2.5 expresses ZDR in terms of the backscatter cross-sections. From this expression it can be seen, that the ratio makes ZDR independent of radar calibration and total particle concentration but dependent on properties affecting the

backscatter cross-section like particle shape, alignment, size, density and phase composition. ZDR is also dependent on the shape of the particle distribution, since large hydrometeors have much more influence on the reflectivity factor than small particles. Propagation effects, namely differential attenuation, affect ZDR, since the horizontal component of the radar wave is more affected by attenuation than the vertical component (Bringi and Chandrasekar, 2001).

Linear Depolarisation Ratio - LDR As mentioned before falling canted particles depolarize a totally linear polarized incident radar beam which means they emit secondary radiation along both principle axes. The *linear depolarization ratio* (LDR) is a measure for the depolarization within the sampling volume. Following Meischner et al. (1995), LDR is defined as

$$LDR = 10 \log_{10} \left(\frac{Z_{HV}}{Z_{HH}} \right) = 10 \log_{10} \left(\frac{\int_{Vol} \sigma_{HV} N(D_e) D_e^6 dD}{\int_{Vol} \sigma_{VV} N(D_e) D_e^6 dD} \right), \quad [LDR] = \text{dB.} \quad (2.6)$$

LDR, like ZDR, is sensible to the asymmetry of particle shapes and their preferred orientation relative to the incident beam. The mean shape of the particles within the sample volume, their mean canting angle, and the precipitation phase determine the value of LDR. LDR is always negative having its maximum value for non spherical particles with canting angles near 45° . Wet ice particles like particles melting or growing in wet mode, can lead to an increased value due to the enhanced refractive index as compared to pure ice. Therefore LDR is especially useful for the detection of graupel and hail above the melting level as these particles often consist of a small portion of water increasing the dielectric constant. Densely rimed ice hydrometeors exhibit a typical tumbling falling behaviour increasing LDR. LDR is independent of the total number concentration of particles and of the radar calibration but not insensitive to propagation effects. Furthermore LDR tends to be highly sensible to noise since the cross-polar signal is typically two to three orders of magnitude smaller than the co-polar signal. For the LDR radar *polarization diversity Doppler radar* (POLDIRAD) the lowest reliable value was found to be around -35 dBZ (Schroth et al., 1988).

Hydrometeor Classification

The possibility to discriminate precipitation types and retrieve microphysical information from polarimetric radar observations is an active field of research since the principle could be successfully tested in numerous studies using basic knowledge about storm kinematics and processes, scatter theory, ground observations and aircraft measurements. Still the method has to deal with several disturbing side effects, like signal attenuation, reflection and others. Several approaches to classify hydrometeors based on polarimetric variables exist. They range from decision trees (Höller et al., 1994)), to fuzzy logic (Straka et al., 2000; Keenan, 2003) and neuro-fuzzy logic (Liu and Chandrasekar, 2000). More details are given in section 3.2.3.

2.4 Methods and Applications of Thunderstorm Nowcasting

2.4.1 Scale Dependencies

The nowcasting of thunderstorms is complicated by the fact that multiple-scale forcing mechanisms often are operating at the same time. There is a mutual interaction between extra-tropical synoptic-scale processes and severe convection (Doswell and Bosart, 2001). Whereas synoptic-scale processes provide a setting in which severe convection develops (Johns and Doswell III, 1992; Barnes and Newton, 1983) the idea becomes accepted that convective processes themselves influence synoptic-scale processes via mesoscale processes. Although there is no universally accepted method to separate scales of motion, all approaches have one basic observation in common: the lifetime of a meteorological feature, like for example the rain field, is dependent on the scale of the feature, with large features evolving more slowly than small features. With this knowledge the dynamically motivated approach to divide scales (Emanuel, 1986; Doswell III, 1987) seems more appropriate than the scale division based on powers of 10 in space and time (Doswell III, 1987).

Like the question about meteorological scales, no universally valid definition for weather forecast regimes exists. In contrast to meteorological scales, weather forecasts are commonly defined based on the time scale of their prognoses only. Since temporal and spatial scales are related, the spatial aspects of the forecast targets are automatically incorporated in the forecast regimes. According to Wilson et al. (2004) and also in use at the DWD the term *nowcasting* is used for prognoses with a time horizon up to 6 h, whereas prognoses on longer time scales are called *forecasts*. *Very short-term nowcasting* refers to prognoses with forecast times up to 2 h. Adapted to the outlines of this work very short-term nowcasting will be used for thunderstorm prognoses up to 30 min.

Certainly the most important question in the field of forecast research is the general question about the predictability of the atmosphere. An extensive study series (Germann and Zawadzki, 2002) to (Germann et al., 2006) addresses to this question from storm to synoptic scales. Some crucial observations strongly influence current forecast research. Based on continent-scale radar composite images they used the lifetime of radar reflectivity patterns in Eulerian and Lagrangian coordinates as a measure of predictability. An important finding has been that the range of predictability increases with increasing scale (Germann and Zawadzki, 2002). They also found that advection explains a significant part of the variation of the precipitation rate at a given location favoring a Lagrangian-persistence approach over an Eulerian approach to extrapolate field patterns (Germann and Zawadzki, 2002). In their Lagrangian persistence approach they identified two sources of forecast uncertainty (Germann et al., 2006). One source is the permanent growth of precipitation and the other is the change in the storm motion field. They found that the contribution of changes in the motion field to forecast

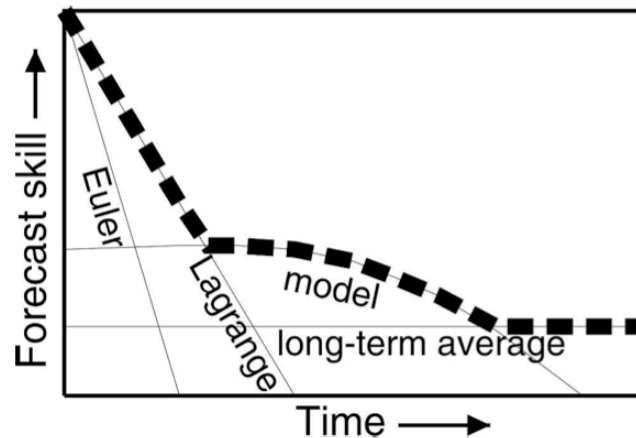


Figure 2.12: Scheme of precipitation predictability versus forecast time (taken from Germann et al. (2006)).

uncertainty is small in comparison with the fluctuation of precipitation.

In their study (Germann et al., 2006) they present a forecast scheme which conceptually illustrates the skill of different forecasting techniques as a function of forecast time. The scheme is given in figure 2.12. The envelope, thick dashed, curve is achieved if the best forecast technique is taken for every forecast time. But due to the problems nature the estimate will never be above the exact predictability. Nowcasting techniques are usually focused on analyses and extrapolation of the trend of a single variable on smaller scales, e.g. radar based rainfall distribution. Models resolve the larger, slower evolving scales, and local details are filled in by parameterisation or statistics. Nevertheless an unavoidable downward trend in information content exists with increasing forecast time due the fact that the atmosphere is a complex, non-linear system. Following figure 2.12 shows the well observed characteristic that for extrapolation methods the initial information capture is close to perfect. But because the method lacks information about atmospheric physics the information is lost rapidly with increasing nowcast time. In contrast thereto the limited resolution and the imperfect assimilation algorithms let models poorly represent the observed state, whereas the information loss with proceeding forecast time is not so large for the earlier part of the forecast. And finally no forecast method is able to assess higher skill than the long-term average.

It can be seen in figure 2.12 that there exists a theoretical intersection, when the information content of a model exceeds the information content of a nowcasting method. The scheme implies that two points have to be addressed in order to improve the nowcasting of weather features to the theoretical possible upper limit. First the nowcast techniques covering the different nowcast scales, like trend extrapolation and models, have to be brought to perfection and second the cross point has to be determined as exactly as possible. This is a complex and delicate issue since both points interact. It depends on the possibilities of the employed nowcasting methods and on the measures used to quantify the information content of the nowcasts. But finally and most important the

method depends on the principal nowcast objectives and the target objects the nowcast tool is designed for.

2.4.2 Current Status of Thunderstorm Nowcasting

In general thunderstorm nowcast algorithms operate in three steps: cell identification, cell tracking, and cell prediction.

Cell Tracker and Area Tracker

For a forecast time up to one hour extrapolation methods based on radar or satellite data are favored, because they provide area-wide information are fast due to rapid data updates, they need only a rather simple data processing, and they still have the highest nowcast skills. Two principal extrapolation techniques can be distinguished. Area trackers (e.g. TREC (Rinehart and Garvey, 1978), COTREC (Li et al., 1995)) use cross correlations between temporally separated consecutive pattern maps, mostly based on satellite or radar products, to find motion fields. Pure cell trackers identify individual storms first and obtain the motion of each storm centroid then over a cost function (e.g. TITAN (Dixon and Wiener, 1993), and (Bonelli and Marcacci, 2008)), or with cell extrapolation from the last time steps (e.g. SCIT (Johnson et al., 1998)). But there exist also nowcasting methods which use a combination of both (e.g. Cb-TRAM (Zinner et al., 2008), TRT (Hering et al., 2004)).

Area tracking algorithms tend to provide more accurate speed and direction information on larger areas, whereas centroid identification and tracking algorithms can track individual storms more effectively and provide cell characteristic information (Johnson et al., 1998). But the real advantage of area trackers is their ability to consider all scale movements to generate nowcasts, whereas pure cell trackers can consider only cell movements neglecting other scales. To assess all scales is an important skill as explained in section 2.4.1 and opens new dimensions for cell and pattern nowcasting which are explained later in this section.

Cell Identification

One method to identify comprehensive regions of enhanced intensities is to locate contiguous areas with values exceeding a single fixed threshold (e.g. TITAN (Dixon and Wiener, 1993)). It is a simple method which has the advantages that cell attributes do not change from one time step to the next and are comparable between different cells. The matter of cell splitting and merging is easier to interpret and handle. As a consequence, especially in strong convection, the so defined cell may contain more than one relative maximum that may be due to independent cells. SCIT (Johnson et al., 1998) applies seven fixed thresholds from 30 – 60 dBZ in 5 dBZ steps to identify the cell cores in a bigger cell complex. To find relative maxima and their adjacency within a cell complex TRACE3D (Handwerker, 2002) uses a second threshold of 10 dBZ in addition

to a basic threshold of 35 dBZ. The algorithm then defines cells from a contiguous region at 10 dBZ below the region maximum. If the region maximum minus 10 dBZ falls below the 35 dBZ the cell will be omitted. In another approach to identify cell cores TRT (Hering et al., 2004) uses an adaptive reflectivity thresholding method with a minimum limit of 36 dBZ to define individual cell cores.

Cell Tracking

Cells are usually tracked using spatial overlaps of previous cells with actual cells (Zinner et al., 2008; Hering et al., 2004)) or via cost functions (Dixon and Wiener, 1993; Bonelli and Marcacci, 2008) to obtain the most plausible cell assignments.

Cell Splitting and Merging Processes Storm splitting and merging are frequently observed processes both in nature and, consequently, in observational data. In order to maintain a continuous cell tracking it is common to track the biggest cell involved and record the minor cells as either new born or just dissipated cells.

Cell Nowcasting

The simplest method for cell trackers to generate a forecast is to extrapolate the future cell positions from past positions. Here it is common to extrapolate the positions of the cell centroids for the calculation. A persistent-nowcast does not use any trend assumption, whereas a trend-nowcast uses trend models in the attempt to capture cell trends out of the latest cell history (e.g. TITAN (Dixon and Wiener, 1993)). Another approach to improve nowcast trends of cell objects is to employ a conceptual model in order to introduce physically based knowledge (see section 2.2.1) about cell evolution into the cell nowcasts (e.g. GANDOLF (Soul et al., 2002), SWIRLII (Yeung et al., 2007)).

Current Nowcasting Approaches

Whereas cell trackers are limited to storm scale, area trackers offer new dimensions for pattern and cell extrapolation techniques (see section 2.4.1 and section 2.4.2). For example the dynamical and spatial scaling approach developed and employed in S-PROG (Seed, 2003) disaggregates the radar reflectivity field into a cascade of fields. Each level field of the cascade represents the features of the original field over a limited range of scales. The Lagrangian evolution of each level is modeled using an autoregressive model. It is assumed, that features at all scales between the outer and inner observed scales are present in the field. It is further assumed, that the lifetime of a feature in the field is dependent on the scale of the feature with large features evolving more slowly than small features.

Another approach generates probabilistic instead of deterministic nowcasts. The approach is based on the idea to express the obvious information loss of nowcasts with increasing forecast time (see 2.4.1) in probabilistic values. Based on the results of their previous studies (Germann and Zawadzki, 2002), Germann and Zawadzki propose a

method, which makes use of the intrinsic relationship between scale and predictability (Germann and Zawadzki, 2004).

Probabilistic values are also used for cell trackers (CellMOS (Hoffmann, 2007)). In this case the probability values express the uncertainty of the latest prognoses and are not related to space-time scales.

Based on the scheme shown in graph 2.12 the UK Meteorological Office developed the 0 – 6 h nowcasting system NIMROD that is a blend of radar echo extrapolation and numerical model precipitation nowcasts. For shorter forecast times the primary weight is given to the extrapolation method which is based on radar data. With increasing nowcast time the weight shifts to the numerical model and becomes almost totally dependent on the model for the 6 hr nowcast. For longer time periods the forecasts were found to be not better than the ability of the numerical model.

In another approach statistical methods were developed to link variables from numerical weather prediction (NWP), the predictors, with observed and predicted variables, the predictands. The perfect prognosis method (PP) (Klein et al., 1959) uses a concurrently developing statistical relationship between the variable to be estimated and selected variables which can be forecast by the model. Both predictand and predictors are observed quantities in the developmental sample. The relationship found in the statistics is applied to NWP output at a certain forecast time to estimate the predictand at exactly the same forecast time. The model output statistic (MOS) determines a statistical relationship between the predictand and the predictors. The forecast values need not necessarily be one of the model output variables. Another statistical method is the usage of neuronal networks which must be trained by large data sets, too. Fuzzy logic provides an efficient manner to combine data sets (e.g. NCAR ANC (Mueller et al., 2003)) and apply conceptual models. It eliminates the binary yes-no decision required by decision trees and uses mathematical functions based on conceptual models to nowcast the likelihood of storms over a grid point in a defined region. Performance statistics be used to tune the functions. In contrast to pure statistical methods fuzzy logic bases primarily on physical understanding, numerical simulations, theory and local forecaster knowledge.

2.4.3 Operational Thunderstorm Nowcasting Tools

As concluded in 2.4.1 the purpose of a nowcasting tool is the general crux of the nowcasting approach. It defines all aspects, the data basis, the tracking object, the tracking and nowcasting method, the data processing and analyses, and finally the verification possibilities. For research purpose it is not necessary to bring the information into an optimized enduser friendly shape but rather to leave all relevant information accessible. Instead, in order to build an end-to-end user tool, it is important to extract the key information and represent it clearly in a user-friendly graphical interface. In this case all unnecessary calculations and informations should be omitted for the benefit of oper-

ationally robustness, computing time, and clearness.

The main purpose of nowcasting research is public profit, e.g. to provide forecasters with appropriately edited weather information in well designed tools. Examples for operational nowcasting systems that are specialized on forecasting storm initiation, growth, and dissipation are at the United Kingdom's Met Office GANDOLF (Pierce et al., 2001) and Nimrod (Golding, 1998), the NCAR ANC (Mueller et al., 2003) in the U.S.. Implemented at the DWD are KONRAD (Lang, 2001), NinJo, both developed at the DWD in Germany, and WIIS, developed at the TU Graz, Austria. At the *Deutsches Zentrum für Luft- und Raumfahrt* (DLR) itself a nowcasting tool for aviation is currently developed within the project *Weather Forecast User Oriented System Including Object Nowcasting* (wxFusion) (Forster and Tafferner, 2009a,b).

Severe storm warnings based on extrapolation have dramatically improved in the past 10 – 15 years and numerous different nowcasting tools based on different or partly related nowcasting principles were developed. For the best possible progress regional test-beds where international researchers and users work side-by-side were introduced by the WWRP Forecast Demonstration Project (FDP) to test and compare actual nowcast techniques regularly under comparable conditions (Keenan et al., 2003). The test beds are oriented to the Olympic Games providing the weather informations for the event. Within the FDP during the Summer Olympic Games in Sydney some of the best known actual nowcasting tools (TITAN (Dixon and Wiener, 1993), S-PROG (Seed, 2003), GANDOLF (Pierce et al., 2001), Nimrod (Golding, 1998), ANC (Mueller et al., 2003)) have been tested. It is remarkable that despite the very different sophisticated methods no tracker could outperform the others. Final analyses from the FDP in Sydney conclude that the best method to improve thunderstorm nowcasts for the 0 – 6 h period in foreseeable future will be to combine numerical prediction with observational and statistical techniques encouraging the actual focus of nowcast research (Wilson et al., 2004). Since several trackers worked with limited capabilities and could not demonstrate their whole capacity. The results from following FDPs, e.g. during the Summer Olympic Games in Beijing 2008, have to be awaited for further insights.

Chapter 3

Methodology and Data Sources

This chapter explains the principal method of the thunderstorm tracking tool named *tracking and monitoring of potential electrically active cells* (ec-TRAM). This tool has been developed for this work to identify thunderstorms and track them through time on the basis of convective ground precipitation and electrical cloud discharges. The new method benefits from the high temporal and spatial resolution, which allows to record small scale storm evolution, the enhanced information content due to the data combination of lightning frequency and ground precipitation, and a more coherent storm tracking, which is the result of the usage of two independent tracking objects, namely lightning-cells and radar-cells. The first part of this chapter, section 3.1, describes the functional structure of the tool ec-TRAM. A detailed description about the method and its subcomponents follows in section 3.1.2, 3.1.3, and 3.1.4. The selection of the final parameter settings, used in the routine ec-TRAM, are discussed in detail in section 4.1. Section 3.1.5 describes the cell data management. The second part of this chapter, section 3.2, describes the data sources, the data preprocessing, and the data usage of this work.

3.1 Concept ec-TRAM

3.1.1 General Approach

The ec-TRAM algorithm is designed to identify, track, and monitor thunderstorms and to generate storm size and location estimates based on convective precipitation and lightning patterns with a temporal resolution of 5 min and a horizontal resolution of approximately $0.7 \times 0.55 \text{ km}^2$ ($0.01^\circ \text{longitude} \times 0.005^\circ \text{latitude}$). The algorithm consists of two separately operating basic routines for precipitation and lightning pattern, respectively. They identify, track, monitor, and nowcast intense ground precipitation regions and electrically active regions independently. The radar-cell tracking algorithm named *tracking and monitoring of intense precipitation fields* (rad-TRAM) (Kober and Tafferner, 2009) is used to identify intense ground precipitation fields by analyzing radar scans close to the ground (see section 3.1.2). The lightning-cell tracking algorithm named *tracking and monitoring of electrically active cells* (li-TRAM) is used to identify electrically active regions in the storm by analyzing lightning data (see section 3.1.3). A cell

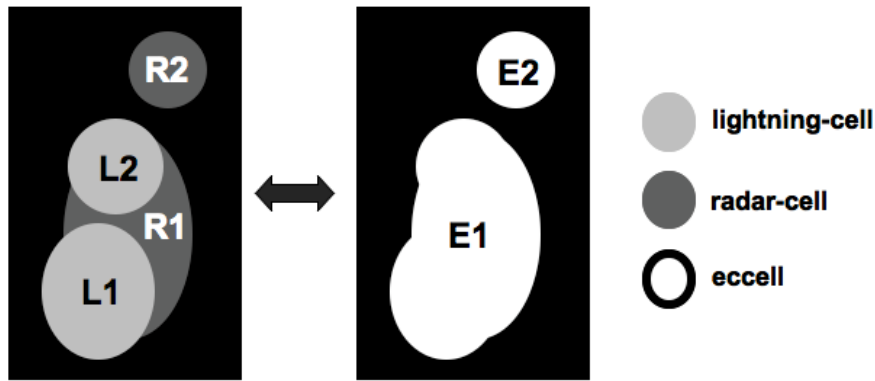


Figure 3.1: Schematic illustration of the tracking object *eccell*. By identifying overlaps of contemporary radar-cells ($R1$, $R2$) and lightning-cells ($L1$, $L2$) the new cell object *eccells* ($E1$, $E2$) is defined. The two-sided arrow indicates, that, due to the introduced data management, no information about single *eccell* components is lost in this mapping.

object identified by rad-TRAM is termed radar-cell (*radcell*). A cell object identified by li-TRAM is termed lightning-cell (*licell*). For every single time step the ec-TRAM routine combines the information from both cell types, *radcell* and *licell*, via spatial overlap into new cell objects (see section 3.1.4). A cell object, which is finally identified by ec-TRAM, is called *potential electrically active cell* (*eccell*). The scheme, presented in figure 3.1 illustrates the definition of an *eccell*. A detailed description of all working processes follows in the subsequent sections.

The tracking routines rad-TRAM and li-TRAM build the fundament of the ec-TRAM algorithm. The procedural structure of the ec-TRAM routine is shown in figure 3.4. They have similar structures. Like the general structure of a tracking tool from the 'TRAM' family (Cb-TRAM (Zinner et al., 2008), rad-TRAM (Kober and Tafferner, 2009), and li-TRAM) they perform the following steps:

1. Two-dimensional intensity maps are retrieved from the primary data source which capture the temporal evolution and motion of the tracking features.
2. A general displacement vector-field is calculated from the intensity maps of two consecutive time steps. The vector-field describes the general motion and the local temporal development of the patterns on a pixel basis.
3. The fields of interest, e.g. strong precipitation or lightning frequency, are identified and marked as cell objects.
4. The tracking and monitoring procedure (TRAM) links detected cell objects from different time steps. The history of information about the detected cell patterns are stored in cell log-files.

5. Spatial nowcasts for cell position and cell shape are calculated by extrapolation of current cells using the displacement vector-field.
6. Specialized tools read the cell log-files and analyze the cell histories or plot selectable cell information.

The ec-TRAM routine uses the log-files, which are generated in step 6 and creates separate log-files for *eccells*. In the log-files of *eccells* general *eccell* features are recorded. Furthermore, the log-files of the respective *licell* and *radcell* constituents, which were generated in step 4, are linked, so that the original cell informations remain accessible (see section 3.1.5). Step 1, 3, 4, and 6 differ in the rad-TRAM and li-TRAM routines and are explained in detail in the subsequent sections. In step 2 and 5 the same methods are used for both algorithms. They are explained in the following.

To extract a pixel-based motion field, the so called pyramidal image matching method is used. The pyramidal image matcher was originally developed for the satellite data-based thunderstorm tracking tool *tracking and monitoring of cumulonimbus objects* (Cb-TRAM) and is described and illustrated in detail in Zinner et al. (2008). The pyramidal image matcher has been adjusted to the requirements of the routines rad-TRAM and li-TRAM.

The issue of scale dependent cloud motion and development has already been discussed in detail in section 2.4.1. The motion of a large scale flow is often superimposed by the motion of small scale features. In order to resolve scale dependent motion patterns, image pairs from two consecutive time steps, $t - \Delta t$ and t , are analyzed in successively refined resolution levels, thus following a pyramidal scheme. Δt is the time increment between the image pairs.

In figure 3.2a and b an example for a simple moving structure is given. First, both dimensions of the two compared intensity maps, $A_{t-\Delta t}$ and A_t , are extended to a multiple of 2^N , with N being the number of the resolution levels of the pyramid. With (n_x, n_y) as the new dimensions of the extended intensity maps, the pyramidal image matching routine runs through stepwise increasing resolutions (from low to high):

$$\left(\frac{n_x}{N^2}, \frac{n_y}{N^2}\right) \Rightarrow \left(\frac{n_x}{(N-1)^2}, \frac{n_y}{(N-1)^2}\right) \Rightarrow \dots \Rightarrow (n_x, n_y). \quad (3.1)$$

For each resolution level a displacement vector-field \vec{V}_t is determined by successively shifting map $A_{t-\Delta t}$ to $A_{t-\Delta t}^s$ by the shifting vector $\vec{s}_{i,j}$ with

$$A_{t-\Delta t}^s = A_{t-\Delta t}(\vec{x} + \vec{s}_{i,j}). \quad (3.2)$$

The indices i and j represent the shift in the two dimensions and indicate integer steps from -2 to 2 pixels. All 25 computed shifted maps $A_{t-\Delta t}^s$ are compared with map A_t . For each map pixel \vec{x} the shift vector \vec{s}^{fit} , which assesses the best fit to transform $A_{t-\Delta t}(\vec{x})$ to $A_t(\vec{x})$, is stored in the displacement vector-field $\vec{V}_t(\vec{x})$. In this study the minimum of the low-pass filtered squared difference of the local intensities, i.e. radar

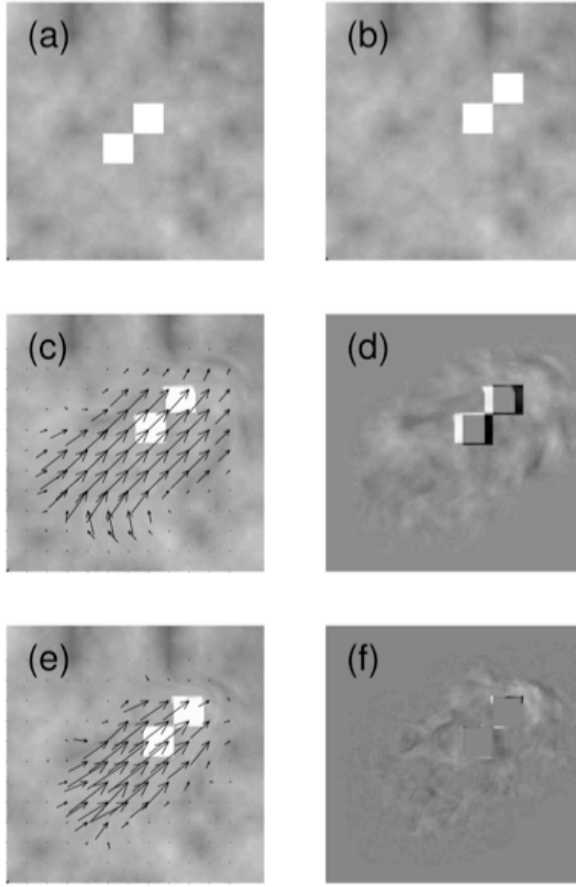


Figure 3.2: Pair of images (a) $A_{t-\Delta t}$ and (b) A_t showing two bright squares on a random background. (c) A displacement vector-field V_t is calculated for them on the highest pyramidal level and plotted on top of $\tilde{A}_{t-\Delta t}(\vec{x}) = A_{t-\Delta t}(\vec{x}) - V_t(\vec{x})$. Only 1 vector out of 100 is shown. (d) The difference field $\tilde{A}_{t-\Delta t} - A_t$. (e) The final displacement vector-field and (f) the final difference field $\tilde{A}_{t-\Delta t} - A_t$ is displayed after all pyramidal levels have been processed (taken from Zinner et al. (2008)).

reflectivity or lightning frequency, is used as quality criterion to define the best fit. This criterion is calculated for every pixel as the convolution

$$D_{loc} = (A_{t-\Delta t}^s - A_t)^2 \otimes K \quad (3.3)$$

with a rotational, normalized Gaussian kernel K . This method suppresses high frequency artefacts from rectangular filter edges (Mannstein et al., 1999). Out of the 25 member vector-fields those $\vec{s}_{i,j}$ are stored in \vec{V}_t which achieve the lowest value D_{loc} . If no extremum is found for a pixel \vec{x} , zero displacement is assumed at this location. The resulting displacement vector-field \vec{V}_t is smoothed and interpolated to the original map size by using a bilinear interpolation. Next the warped map $\tilde{A}_{t-\Delta t}$ is calculated as

$$\tilde{A}_{t-\Delta t} = A_{t-\Delta t} - \vec{V}_t. \quad (3.4)$$

Figure 3.2c shows the warped image $\tilde{A}_{t-\Delta t}$ and the displacement vectors \vec{V}_t after the uppermost pyramidal processing step. The test structure of the two adjacent squares is shifted to the approximate target position figure 3.2c in $\tilde{A}_{t-\Delta t}$. The values from $A_{t-\Delta t}$ are bilinearly interpolated to sample the values of $\tilde{A}_{t-\Delta t}$. $\tilde{A}_{t-\Delta t}$ is then used as starting point for the matching procedure of the next lower pyramidal level, replacing $A_{t-\Delta t}$ in equation 3.2. The resulting disparity vectors are successively added to the displacement vector-field \vec{V}_t until, in the end, the fully resolved image is matched. Finally, the pyramidal image matcher returns a displacement vector-field \vec{V}_t (figure 3.2e), which

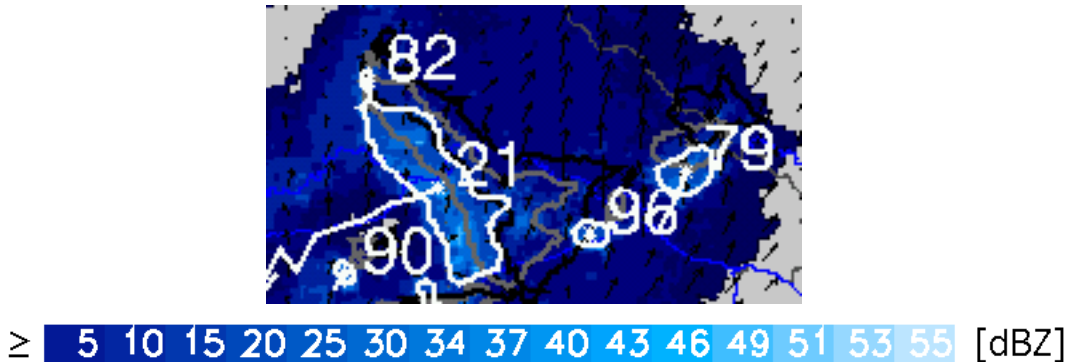


Figure 3.3: Example graph calculated with the routine rad-TRAM (see section 3.1.2) to illustrate the TRAM method. The black arrows represent the displacement vector-field calculated by comparing the current intensity map (shown) with the previous intensity map (not shown). Identified radar-cells are enclosed by white contours and their cell-centers, cell-tracks, and cell numbers are drawn in white. Spatial cell-prognoses for 10 min and 20 min are indicated by grey and black contours, respectively.

incorporates large scale movements as well as small scale movements, and the warped map $\tilde{A}_{t-\Delta t}(\vec{x})$ (figure 3.2f).

In order to obtain information on each pixel, not only the displacement vector-field \vec{V}_t is calculated to describe the forward direction $A_{t-\Delta t} \rightarrow A_t$, but also the displacement vector-field $\vec{\bar{V}}_t$ to describe the backward direction $A_t \rightarrow A_{t-\Delta t}$. Short-range cell nowcasts, which include cell displacements and shape deformation, are achieved by extrapolating current cell objects. The displacement vector-fields \vec{V}_t and $\vec{\bar{V}}_t$ are applied on the cell-maps C_t and $C_{t-\Delta t}$. The cell map is a bicolored mask, where only the cell area and position are marked on a zero background. New bicolored cell-prognoses maps, which have the information of the spatial cell prognoses for a lead-time of $d \cdot \Delta t$, are calculated by

$$\tilde{P}_{d \cdot \Delta t}(\vec{x}) = d \cdot (C_{t-\Delta t}(\vec{x}) - \vec{V}_t(\vec{x})) + (1 - d) \cdot (C_t(\vec{x}) - \vec{\bar{V}}_t(\vec{x})). \quad (3.5)$$

Figure 3.3 exemplifies the principles of the TRAM method. The illustrated example is calculated by the algorithm rad-TRAM on the basis of radar reflectivity data.

The highest pyramidal level N has been set to 2 in both tracking routines rad-TRAM and li-TRAM. 16 pixels are searched for pattern matching, since the search radius is 2^{N+2} . This is equivalent to a distance of 12 km or 9 km, depending on the direction. With this setting cell motions up to 140 km/h are assessed. The Gaussian kernel K has a diameter of 7 pixels (approximately 4.5 km) which ends in 28 pixels for the second, the highest, pyramidal level. The size of the Gaussian kernel has to be considered for analyses near the domain edges, if the motion field is included in the analyses data.

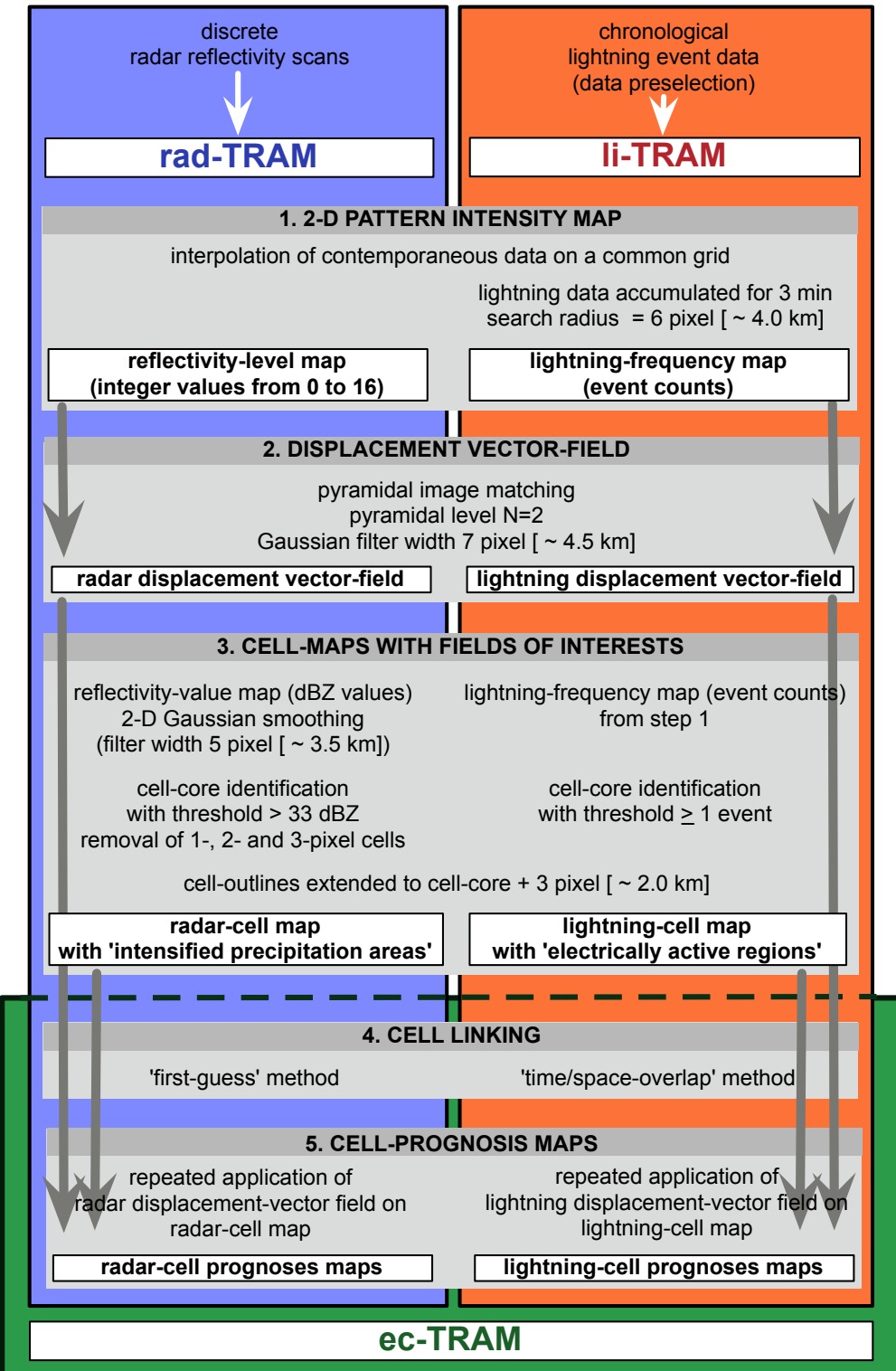


Figure 3.4: Procedural scheme of rad-TRAM and li-TRAM following the description on page 38.

3.1.2 Radar-Cell Tracker rad-TRAM

The algorithm rad-TRAM was developed to operate on DWD radar composite data (Kober and Tafferner, 2009), which provide radar reflectivities in 7 levels every 15 min on a $2 \times 2 \text{ km}^2$ grid. In this study, the algorithm was adapted to the finer resolved low-level precipitation scans of the DWD C-band Doppler Radar in Fürholzen. A map showing the radar site and the research domain is given in figure 3.2.5. This scan provides 17 reflectivity levels on a $1 \times 1 \text{ km}^2$ grid every 5 min (see section 3.5). The subsequent description follows the procedural list on page 38 and is illustrated on the left side in the scheme of figure 3.4. The selection of the final parameter settings, used in the routine rad-TRAM, are discussed in detail in section 4.1.

First an intensity map is built. Therefore, the reflectivity field is transposed to the finer resolved basic grid used in the ec-TRAM routine (see section 3.1.1). The value of the nearest pixel is allocated to the new grid points. The *reflectivity-level map* contains integer values ranging from 0 to 16. Then, based on this intensity map, a *radar displacement vector-field* is calculated using the pyramidal image matching method described in section 3.1.1.

To identify regions of intense precipitation, first the reflectivity levels are replaced by the respective radar reflectivity values. Before the resulting map is searched for radar-cells, it is convolved with a 5 pixels \times 5 pixels sized (approximately 3.5 km), normalized, rotational symmetric Gaussian filter to smooth the reflectivity patterns (see upper left panel in figure 3.5). Based on the smoothed *radar-reflectivity map*, coherent reflectivity areas of four or more pixels, which exceed a threshold of 33 dBZ, are identified as *radcells*. The cell-outlines are defined as the identified area plus three pixels (approximately 2.0 km) in every direction, so that cells which are too close are avoided (see upper mid panel of figure 3.5). Respective cell parameters are calculated. For every time step a bicolored [0/1] *radar-cell map* is generated where all identified *radcells* are marked with 1 on a zero background.

After that, the radar displacement vector-field is applied to the radar-cell map of the previous time step to calculate a '*first-guess*' cell map for the current time step. Following the terminology of section 3.1.1 and equation 3.4 the '*first-guess*' radar-cell map $\tilde{C}_{t-\Delta t}^R$ is calculated by

$$\tilde{C}_{t-\Delta t}^R = C_{t-\Delta t}^R - \vec{V}_t^R \quad (3.6)$$

with $C_{t-\Delta t}^R$ being the bicolored radar-cell map of the previous time step and \vec{V}_t^R being the radar displacement-vector field. The bicolored '*first-guess*' cell map contains the information about cell positions and cell shapes for the next (current) time step. Cell numbers from the previous time step are passed on to current cells, if a '*first-guess*' cell of $\tilde{C}_{t-\Delta t}^R$ and a current cell of C_t^R overlap (see upper right panel in figure 3.5).

If a newly identified cell has no spatial overlap with any '*first-guess*' cell, it is considered as undisturbed and independently developed. A new cell number is assigned and

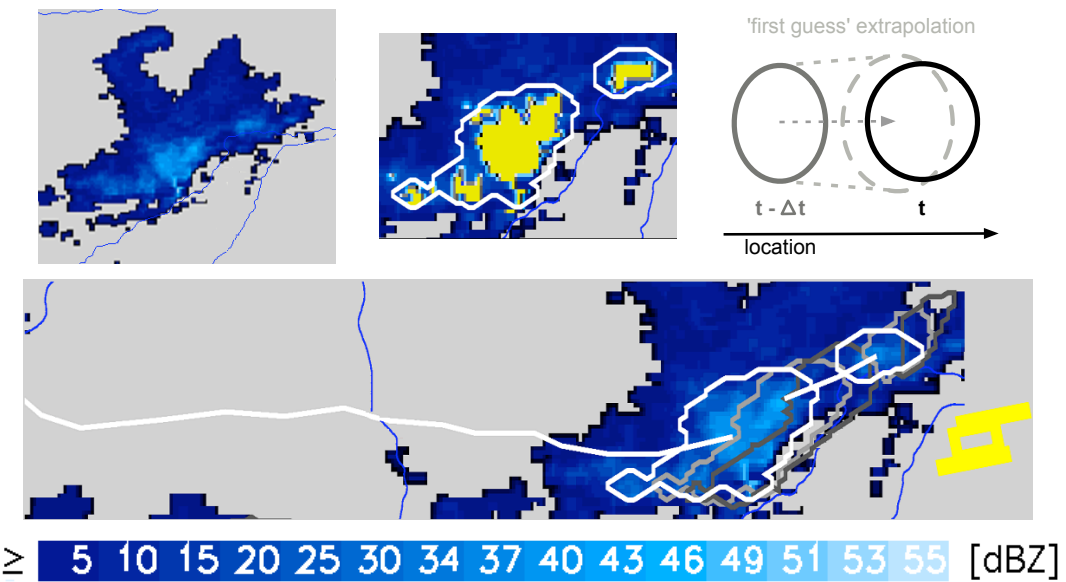


Figure 3.5: Procedural steps of the rad-TRAM algorithm. Upper left: Radar reflectivity map. Upper middle: *radcell* identification with values exceeding the threshold in yellow and cell outlines in white. Upper right: Cell tracking via 'first-guess' method. The radar-cell of the previous time step $t - \Delta t$ is grey colored, its extrapolation to the current time step t and the resulting 'first-guess' cell are light grey in dashed line style, and the radar-cell outline of the current time step t is black. The arrow illustrates the cell displacement with time. An overlap of a 'first-guess' cell with a current cell links cells from two consecutive time steps. Lower graph: Map detail of a track assessed by the routine rad-TRAM with current cell contours and cell tracks white colored. Cell nowcasts for 10 min and 20 min are in light and dark grey, respectively. The yellow symbol indicates Munich Airport.

a new cell log-file opened. If a 'first-guess' cell has no area overlap with any cell, it is considered as undisturbed dissipated and its log-file is closed. If there is more than one current cell overlapping with a previous cell, a cell splitting is assumed. The current cell with the largest cell area inherits the old cell number and continues the cell history. The cell splitting is marked as 'split' in its log-file. All smaller cells obtain new cell numbers and new log-files are opened. They are marked as 'split-born' to point out for later analyses that they are not undisturbed grown but emerged from a cell splitting. In the log-files of all cell participants of the process, the total number and a list with the cell numbers of the other participants are recorded. If more than one previous cell overlap with a current cell, a cell merging is assumed. The cell number of the previous cell with the largest overlapping area fraction is passed on to the current cell and the process is marked as 'merge' in the log-file. Those previous cells with minor cell overlaps are no longer tracked and their cell numbers disappear in the current time step. Before their log-files are closed, they are marked as 'merge-dissipated' to point out for later analyses that they did not dissipate undisturbed but vanished due to cell merging. Again, the total number and a list of the cell numbers of the other cells, involved in the process,

are saved in the cell log-files of all cell participants.

Nowcasts of cell position and shape of current cells for the next time steps are calculated from equation 3.7 by the repeated application of the radar displacement vector-field on the current bicolored [0/1] radar-cell map, thus following the method described in section 3.1.1. The cell prognoses are plotted on bicolored [0/1] *radar-cell prognoses maps*. The nowcast quality for lead times up to 30 min is discussed in section 4.2. A map detail showing a *radcell* object tracked by rad-TRAM is given the lower illustration of figure 3.5.

3.1.3 Lightning-Cell Tracker li-TRAM

The lightning-cell tracking algorithm li-TRAM operates on spatially and temporally clustered *lightning-frequency maps*. The right side of the scheme in figure 3.4 gives an overview of the individual procedural steps. The selection of the final parameter settings, used in the routine li-TRAM, are discussed in detail in section 4.1.

In a first step, the lightning data are preselected as described in section 3.2.1. The accumulated lightning data of 3 min are mapped on the basic ec-TRAM grid. Every discharge event is allocated to the nearest grid point (see upper left panel in figure 3.6). Lightning-frequency maps are derived by extending the discharge counts per pixel to circles with diameters of 7 pixels (approximately 4.5 km). Starting with encircling the lowest discharge count the circle of the highest discharge count is upmost (see upper mid panel in figure 3.6). The *lightning displacement vector-field* is calculated from two consecutive lightning-frequency maps using the pyramidal image matching method as described in section 3.1.1.

Coherent areas on the lightning frequency map with a 3 min discharge activity of 1 event or higher are then clustered to lightning-cells. The effective search radius to cluster discharge events to cells is 7 pixels (approximately 4.5 km). The cell outlines are extended by three pixels (approximately 2.0 km) in every direction (see upper mid panel in figure 3.6). Cell parameters are recorded. A bicolored [0/2] *lightning-cell map* is established, where lightning-cells are marked with 2 on a zero background. Every single event is a priori recorded as lightning-cell. The cells are selected later according to the needs of the posed analysis problem.

Lightning-cells are tracked using a method, which is called '*time/space-overlap method*' in the following (see upper right panel in figure 3.6). Every 2.5 min, discharge events of the last 3 min are used to cluster lightning-cells. The time step of 2.5 min has been chosen, because it divides the temporal resolution of the radar scan without remainder and therefore allows a comparison of time-coincident radar and lightning-cells in each ec-TRAM time step. The data accumulation interval of 3 min has been chosen, so that a persistent lightning-cell includes events, which are also used to identify the same cell in the previous time frame. This is found to be sufficient since additionally the time interval is so short that two consecutive cell contours generally overlap, because other-

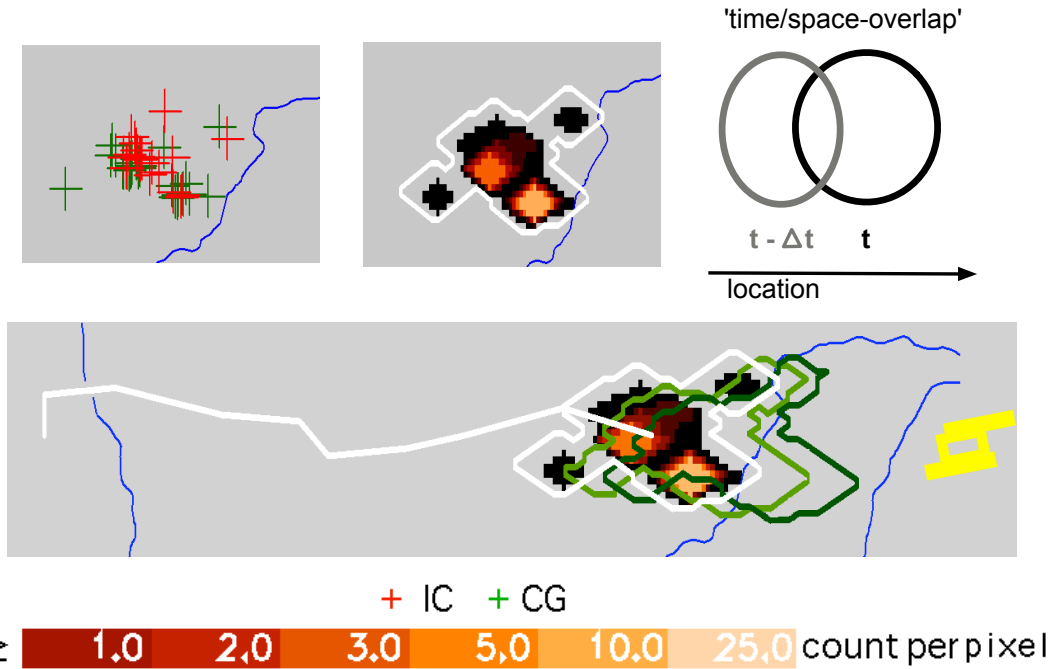


Figure 3.6: Procedural steps of the li-TRAM algorithm. Upper left: Discharge event map with 3 min lightning data. Upper middle: *licell* identification on the basis of a lightning frequency map. Cell outlines are white colored. Upper right: Cell tracking via 'time/space-overlap' method. The lightning-cell of the previous time step $t - \Delta t$ is grey colored, the lightning cell of the current time step t is black colored. The arrow illustrates the cell displacement with proceeding time. An overlap of a previous cell with a current cell links cells from two consecutive time steps. Lower graph: Map detail of a track assessed by the routine li-TRAM with current cell contour and cell track white colored. Cell nowcasts for 10 min and 20 min are in light and dark green, respectively. The yellow symbol indicates Munich Airport.

wise they would have to propagate faster than 120 km/h, which hardly occurs. Cells are tracked via spatial overlap of previous and current cells. Cell merging and splitting processes are handled in the same way as in the rad-TRAM algorithm.

Spatial cell nowcasts are calculated after equation 3.7 by the repeated application of the lightning displacement vector-field on the current bicolored [0/2] lightning-cell map. The results are bicolored [0/2] *lightning-cell prognoses maps*, which carry the information about cell displacements and shape deformations. The nowcast quality for lead times up to 30 min is discussed in section 4.2. A map detail showing a *licell* object tracked by li-TRAM is given in the lower illustration of figure 3.6.

3.1.4 Tracking Method ec-TRAM

Eccells are defined by the spatial overlap of coincident radar and lightning-cells. The method is schematically illustrated in figure 3.1. An example is given in figure 3.7. The

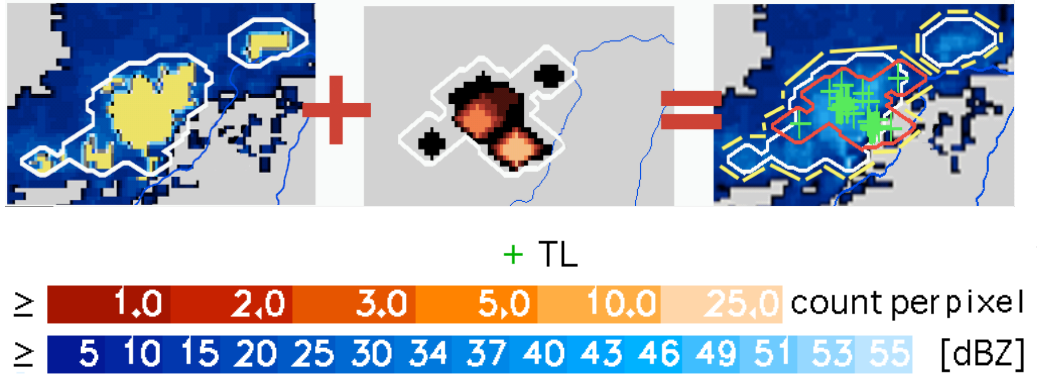


Figure 3.7: Illustration of the ec-TRAM method. Left: Radar-cells (white contours) identified by rad-TRAM (taken from figure 3.5). Middle: Lightning-cell (white contour) identified by li-TRAM (taken from figure 3.6). Right: Overlay of rad-TRAM and li-TRAM output with the *eccell* outlines drawn yellow in dashed line-style. The lower *eccell* consists of a radar-cell (white contour) and a lightning-cell (red contour). The upper *eccell* consists of a radar-cell only.

term coincidence is used to indicate, that the data accumulation interval to calculate lightning-frequency maps ends with the reported radar scan time. Following the terminology from section 3.1.1, with C_t^R as bicolored [0/1] radar-cell map (see section 3.1.2) and C_t^L as bicolored [0/2] lightning-cell map (see section 3.1.3) the *eccell* map C_t^E is calculated by

$$C_t^E(\vec{x}) = C_t^R(\vec{x}) + C_t^L(\vec{x}). \quad (3.7)$$

Consequently the values of C_t^E range from 0 to 3. Contiguous cell areas with values higher than zero are identified as *eccells*. The maximum value found within the *eccell* indicates the cell type. If the maximum value is 3, the *eccell* consists of more than one cell component. If the maximum value is 2, the *eccell* is a pure lightning-cell, and if the maximum value is 1, the *eccell* is a pure radar-cell. So depending on existing overlaps of *licells* and *radcells*, an *eccell* can consist of one cell type as well as any cell compound of radar and lightning-cells. The majority of the *eccells* are found to consist of one or two cell components. This is a consequence of the parameter adjustments for lightning and radar-cell identification, which were selected with focus to preserve reasonable and comparable cell areas. A detailed discussion to the parameter selection is given in section 4.

To track an *eccell* from one time step to the next, it is first looked for already identified tracks of lightning-cells and radar-cells, which are part of the current *eccell* complex. If such a track exists, the current *eccell* complex is connected to the previous *eccell* complex, where that cell track leads to. If more tracks exist, the track of that current cell with the largest area is used. If no track can be found to connect the current *eccell* to an *eccell* from the previous time step, the cell is considered as recently and undisturbed grown and a new cell number with a new cell log-file is assigned. If no track can be found to pursue an *eccell* of the previous time step to a current *eccell* the cell is considered as dissipated, the log-file is closed, and the respective cell number vanishes in the current

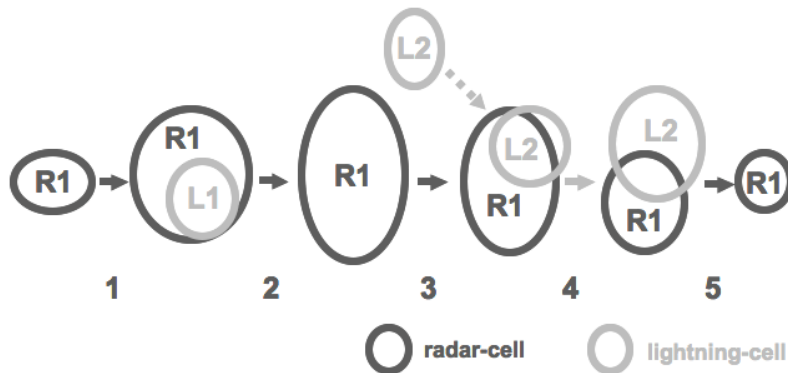


Figure 3.8: Schematic illustration of the tracking method used to follow *eccells* from one time step to the next. The method relies on already identified cell tracks for radar-cells and lightning-cells. In the scheme identified lightning-cells and lightning-cell tracks are drawn in light grey, radar-cells and identified radar-cell tracks in dark grey. The final *eccell* track is in full line style, the dismissed track is in dashed line style.

time step. And in case of any ambiguity, if more than one possible cell track is found, the cell with the largest area is chosen to pass on the *eccell* number. An example to illustrate the tracking method for *eccells* is given in figure 3.8. The exemplary cell track starts with radar-cell *R1*, where no cell track exists to link the cell *R1* with a previous cell. The track of radar-cell *R1* determines the *eccell* track for link 1, 2, 3, and 5 (indicated by the numbers below). In case of ambiguity the largest current cell is favored, as it can be seen in the scheme at link 3 and link 4. At link 3 the cell track of the smaller lightning-cell *L1* is dismissed (dashed grey line) and the cell track of the larger radar-cell *R1* is taken as current *eccell* track. At link 4 it is the cell-track of the bigger lightning-cell *L2* which determines the *eccell* track (indicated by the grey arrow).

Methods to generate *eccell* forecasts are proposed and discussed in section 4.3. But since they have not been the focus of this study, they were not implemented in the ec-TRAM algorithm so far.

3.1.5 Cell Database

The current and predicted cell contours of *radcells* and *licells* are saved in separate text files as a matter of memory size. The other radar-cell, lightning-cell, and *eccell* parameters are stored in a relational SQL database. The database currently consists of seven tables. Three tables record *licell* characteristics. One table records general *licell* parameters, such as cell area and cell displacement, one table records cell discharge characteristics, and another table records selected radar reflectivity values, which are found inside the *licell* contour. Two tables store *radcell* characteristics. Again, one table stores the general cell parameters, the other one stores selected radar reflectivity values. One table describes general cell features of *eccells*, like cell area, cell displacement, number of cell constituents and their area overlap. The last table links all those table entries, which belong to an *eccell* entry. So all tables are internally linked, which makes

various kinds of data combinations possible. More parameters than those, which are investigated within this work, were calculated and stored in the database. The database structure, linkage, and the tables with all recorded cell variables are described in detail in appendix A.4.

This method provides selective access to information about the whole *eccell* complexes and its structure as well as detailed information about every single cell compound. This leaves the possibility to investigate lightning-cells and radar-cells both, separately or in combination as *eccells*, and in case-studies as well as in statistical analyses.

3.2 Data Sources

3.2.1 Lightning detection network - LINET

Specification

Three-dimensionally resolved total-lightning data are provided by the European lightning detection network LINET (Betz et al., 2009a, 2007). LINET was developed at the University of Munich and put in operation by nowcast GmbH in 2006. Today the network consists of about 100 sensors in central Europe.

The system is operated in the VLF/LF regime with a frequency range of 5 – 200 kHz. The network provides three-dimensionally resolved discharge locations, discriminating routinely IC and CG events by calculating the discharge heights. Three-dimensional

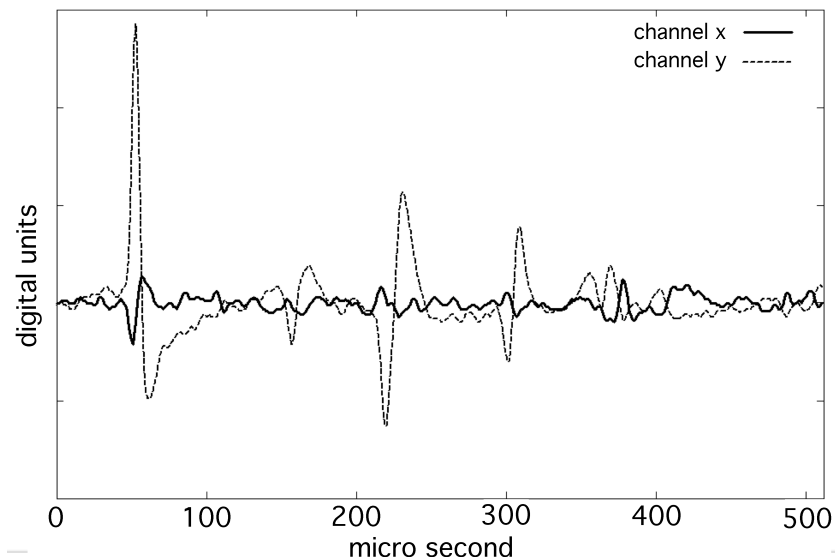


Figure 3.9: Example of a signal wave as it is recorded at a LINET sensor. The diagram shows the antenna signals at the two orthogonal antennas (channel x, channel y) in digital units versus the time in μ s. The time window used by the network is 512 μ s.

TOA calculations are used, altering the event location (latitude, longitude, altitude) and the event time in the fit routine (see section 2.3.1). Information about characteristic points in the raw signals are sent to a central processor, where they provide the input information for the fit routine. The information about the arrival angle of the incoming signal is additionally employed as a knock out criteria to remove implausible outliers. Plane, two-dimensional source localization is possible, if at least four sensors measure the event signal. A reliable separation of return strokes and cloud pulses is achieved if the closest sensor lies within a radius of 120 km to the discharge source. An example of an incoming signal, as it is recorded at the two orthogonal station antennas, is presented in figure 3.9.

In the central part of the network the two-dimensional location accuracy reaches a statistical average of approximately 150 m, depending on the location within the network and the sensor constellation which was used in the fit routine. Additionally, the height error is calculated for every altitude value. This error, too, depends strongly on the sensor constellation. The reliability of IC and CG data has been tested by systematic comparisons with radar cross-sections and lightning strokes in towers. A detailed description of the localization method and the network characteristics can be found in Schmidt (2007).

Data Preprocessing

Due to non-uniform sensor spacing discharge parameters show local sensitivity variations. To achieve a network insensitive thunderstorm monitoring with comparable cell life-cycles, lightning data are preprocessed. The following studies have been performed to assess the network sensitivity of important discharge parameters and to find methods to prevent network sensitive parameter changes due to the sensor spacing. All studies presented in this work are performed on the total discharge data set which was recorded during 50 thunderstorm days in summer 2008 in the research domain (see section 3.2.5).

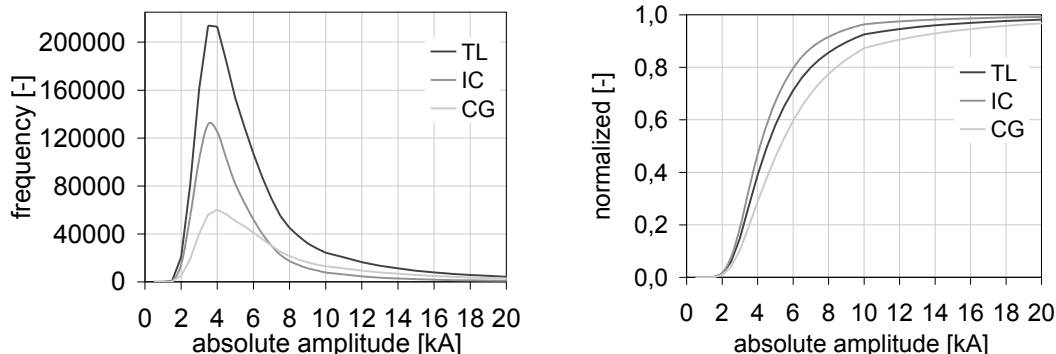


Figure 3.10: Frequency distribution (left) and normalized cumulative frequency distribution (right) of the absolute amplitude for TL, IC, and CG events of the complete lightning data set.

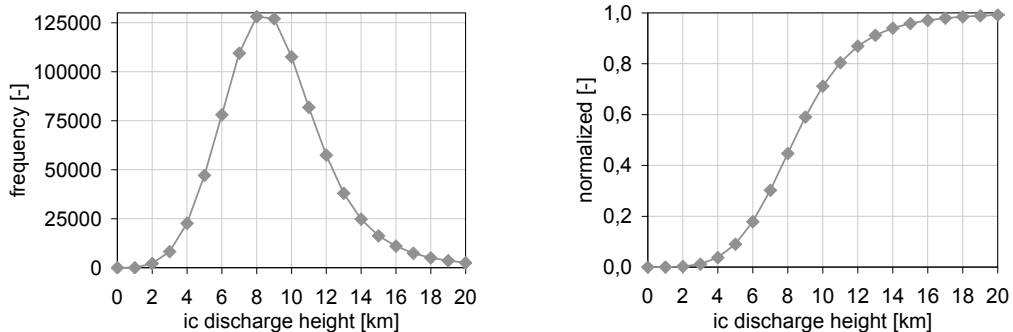


Figure 3.11: Frequency distribution (left) and normalized cumulative frequency distribution (right) of the IC discharge height of the complete lightning data set with amplitudes greater than 2.5 kA.

The lightning detection network LINET provides the lightning data categorized in three classes: one class includes the so called 'secure CG events', one class includes the so called 'secure IC events', and the last class includes those events which do not meet the criteria for a secure assignment. The classification criteria is a combination of location error and the distance to the closest sensor. The fraction of '*secure IC*' : '*secure CG*' : '*undefined*' was found to be 199 592 : 103 226 : 37 835 and expressed as percentage 60% : 30% : 10% in the total data set, which was used for the studies (after the preselection which is discussed later in this section). Based on these three classes, pure TL statistics in this study refer to the events of all three classes. The IC discharge statistics refer to those events, which passed the tests for secure IC events, and CG discharge statistics refer to those events, which passed the tests for secure CG events. As a consequence, the sum of IC events and CG events is not necessarily equal to the number of TL event. This is the reason why in the context of investigations about IC to CG relations both discharge characteristics are set in relation to their sum instead of the TL count.

Figure 3.10 presents the frequency distributions of the absolute amplitude for TL, IC, and CG events over the total-lightning data set. The distribution maximum is found between 3.0 kA and 3.5 kA. The frequency distribution for IC events is skewed to lower discharge amplitude than the distribution for CG. This characteristic is also supported by theory (Cooray, 2003).

Figure 3.11 presents the frequency distributions of the IC discharge heights for all IC events with absolute amplitudes higher than 2.5 kA. Most of the IC events are found between 8 km to 9 km altitude.

Sensitivity maps with the minimum detectable absolute discharge amplitude for different minimum amplitude thresholds are shown in figure 3.12. The sensitivity map calculated with the total data set is presented in figure 3.12a. It can be seen that the lowest amplitudes are recorded within the densest part of the sensor network and the minimum detectable amplitude increases with increasing distance R from the center of

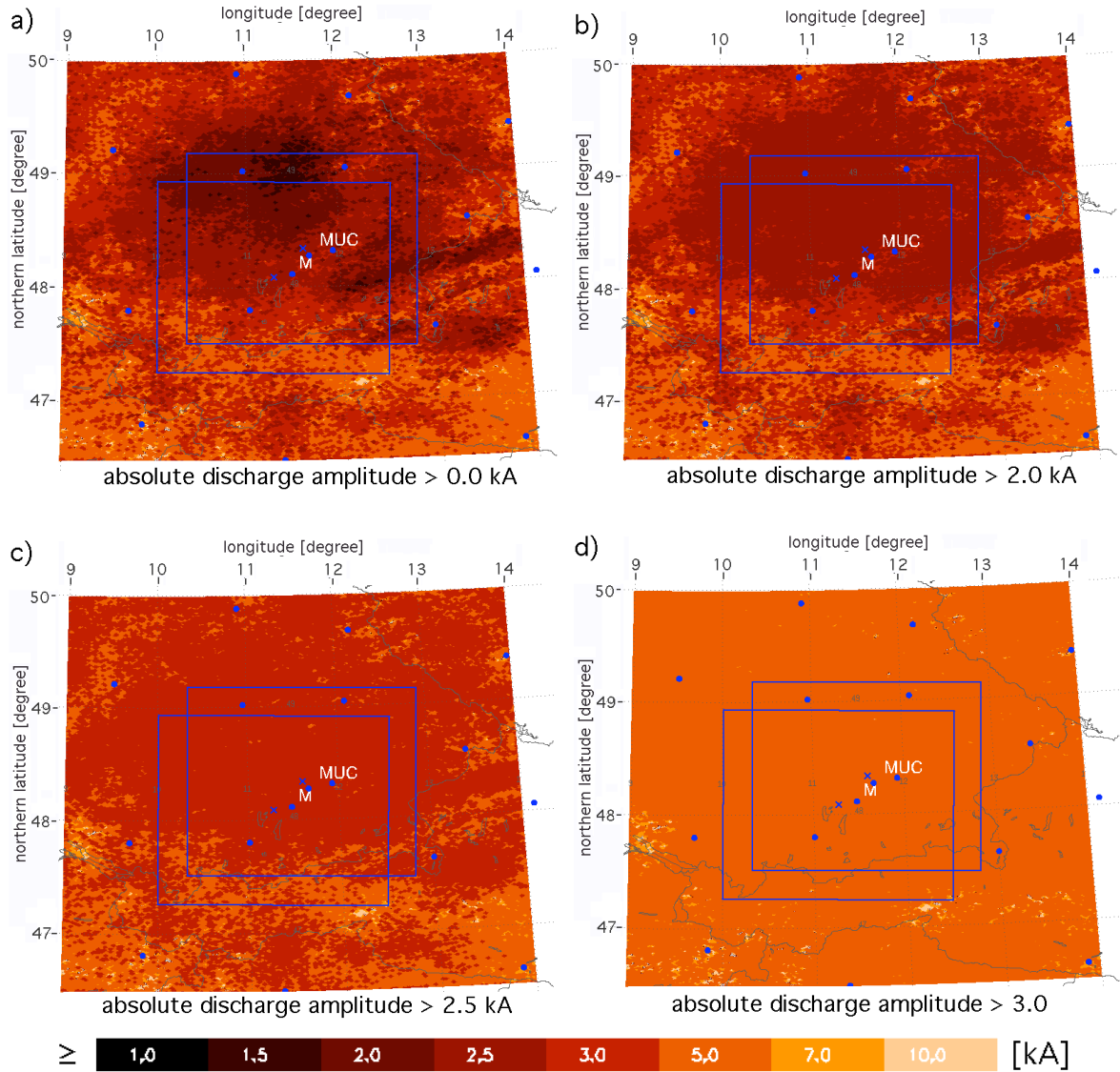


Figure 3.12: Sensitivity maps showing minimum absolute discharge amplitudes for different minimum amplitude thresholds. The upper right rectangle indicates the area coverage of the DWD radar in Fürholzen, the lower left rectangle approximates the coverage of the DLR radar POLDIRAD. The radar sites are marked with crosses in the centers of the rectangles. The sensor stations of the lightning detection network LINET are marked with blue dots. Munich is indicated by an M, Munich airport by the letters MUC.

the sensor network. This feature has already been observed (Betz et al., 2009a; Höller et al., 2009) and is attributed to the $1/R$ signal reduction of a propagating ground wave. The map reveals that the minimum detectable peak current ranges from 1 kA in the central part of the network to 3.0 kA in the southern parts of Germany. Figure 3.12b, figure 3.12c, and figure 3.12d are calculated with the same discharge data set but for discharge amplitudes greater than 2.0 kA, 2.5 kA, and 3.0 kA, respectively. Considering

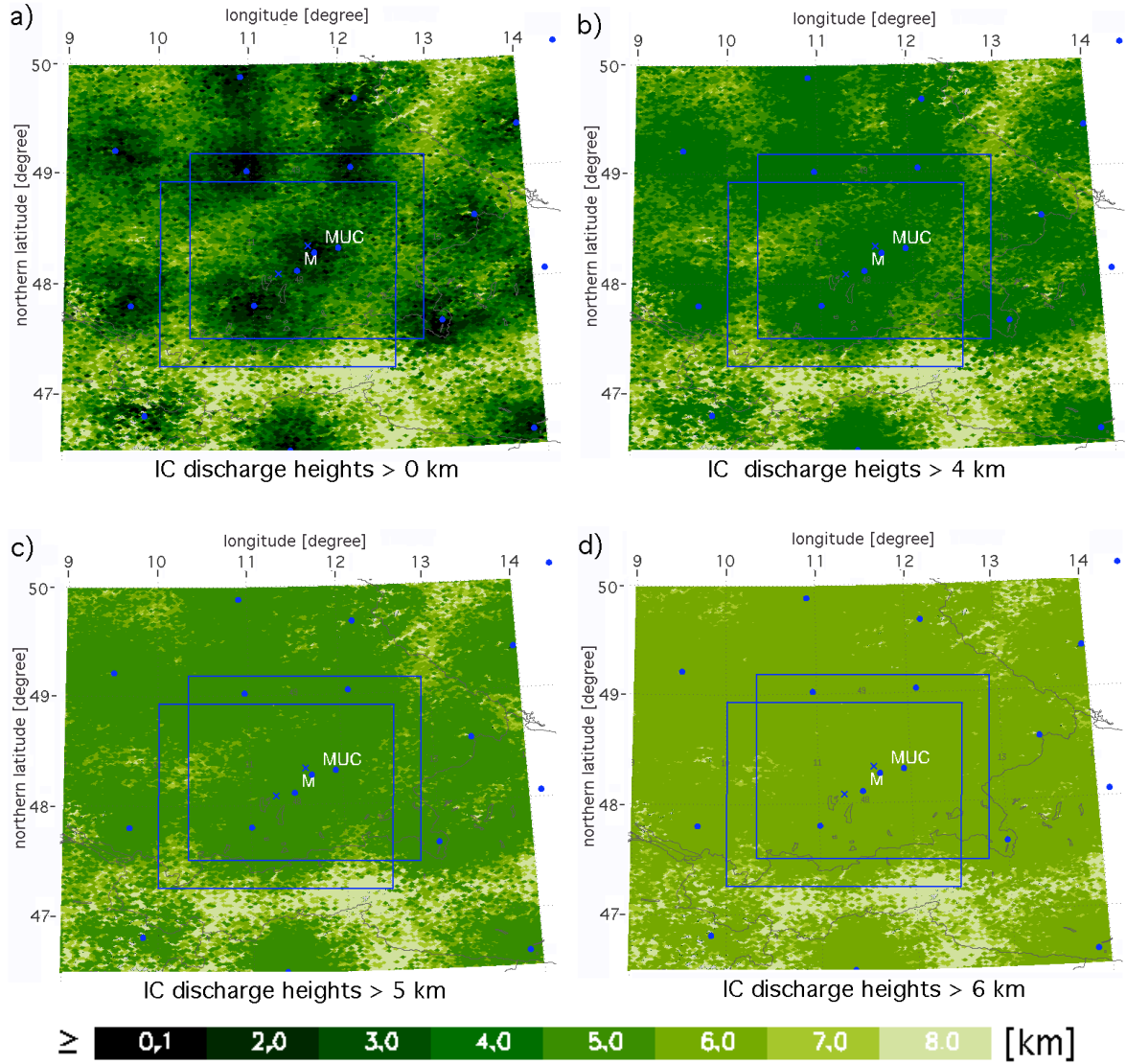


Figure 3.13: Sensitivity maps showing minimum IC discharge heights for lightning events with amplitudes greater than 2.5 kA and different minimum height thresholds. The labeling is the same as in figure 3.12.

the area coverage of the DWD radar in Fürholzen, which is indicated in the maps by the upper right square, a minimum amplitude of 2.5 kA was set for lightning discharges throughout the whole study. It can be read from the cumulative frequency distribution over the absolute discharge amplitudes, presented on the right side of figure 3.10, that still about 92 % of the CGs 90 % of the ICs remain in the lightning data set.

Sensitivity maps showing the minimum detectable IC discharge heights for different minimum IC discharge height thresholds are shown in figure 3.13. The IC discharge data set used for this study includes all IC events of the total-lightning data set with absolute discharge amplitudes of more than 2.5 kA. The sensitivity map, which is calculated without any minimum height threshold, is presented in figure 3.13a. It can be

seen that local minima appear around the sensor locations. This is a consequence of the fit method employed by the network LINET. Figure 3.13b, figure 3.13c, and figure 3.13d are calculated for IC discharge events of the complete IC discharge data set but with minimum discharge altitudes of 4.0 km, 5.0 km, and 6.0 km, respectively. Based on this sensitivity study a minimum IC discharge height of 5.0 km was introduced. This threshold is only applied, when IC discharge height characteristics are investigated. According to the IC height frequency distribution, presented in the right panel in figure 3.11, about 90 % of all IC events with absolute amplitudes higher than 2.5 kA are found in altitudes higher than 5 km and can be used for IC discharge analyses.

The need of a correction of systematic errors in maximum discharge height has also been investigated. But the sensitivity maps of this study are far less shaped than the sensitivity maps of the minimum detectable IC discharge heights. Height disparities become visible for discharge heights above 16 km. Since less than 5 % of the IC events are recorded at an height higher than 16 km and, additionally the pattern structure of the maps lacks a reasonable explanation, no maximum threshold for discharge heights was used in the preselection of the lightning data within this work.

Finally, a study has been performed to assess the spatial distribution of the IC and CG discrimination ability within the domain. The sensitivity maps are presented in figure 3.14. The data basis for the calculations includes the discharge events of the complete lightning data set with absolute discharge amplitudes greater than 2.5 kA. For the sensitivity maps presented in figure 3.14c and figure 3.14b, where the IC frequency has been investigated, only IC events recorded at an altitude of 5 km and higher were considered. The study contains a frequency distribution map for TL activity shown in figure 3.14a, for IC events shown in figure 3.14c, and for CG events shown in figure 3.14d. Finally the ratio of IC to CG occurrence, presented in figure 3.14b, was investigated. The ratio is supposed to give an impression of the local IC to CG detection efficiency within the domain, if an even occurrence of both discharge types can be assumed. In all four maps the maximum values are white colored. The lower the values, the darker is the red shade, zero values are in black. The graphs of figure 3.14 are generated to give a qualitative impression of the spatially distributed frequencies (or ratios in case of figure 3.14b) for the selected parameters. In order to preserve the range, which underlies the color shading in the graphs, the table in figure 3.14 lists the highest interval steps for each contour map in the figure, respectively. Frequencies (ratios) above these thresholds are white colored in the graphs.

All four maps reveal a rather spotty structure. Some of the 'hot spots' in the frequency map of the IC event of figure 3.14c could probably be explained, if the single events were tracked back to the lightning localization calculation itself. They might be due to a favorable sensor constellation. An enhanced occurrence of CG events might also be due to the orography or to exposed structures. An attempt to link the hot spots of CG occurrence with the topography revealed no reasonable correlation. Another possible explanation for the observed patterns might be, that few but very active thunderstorms with extreme characteristics in one or the other way are responsible for

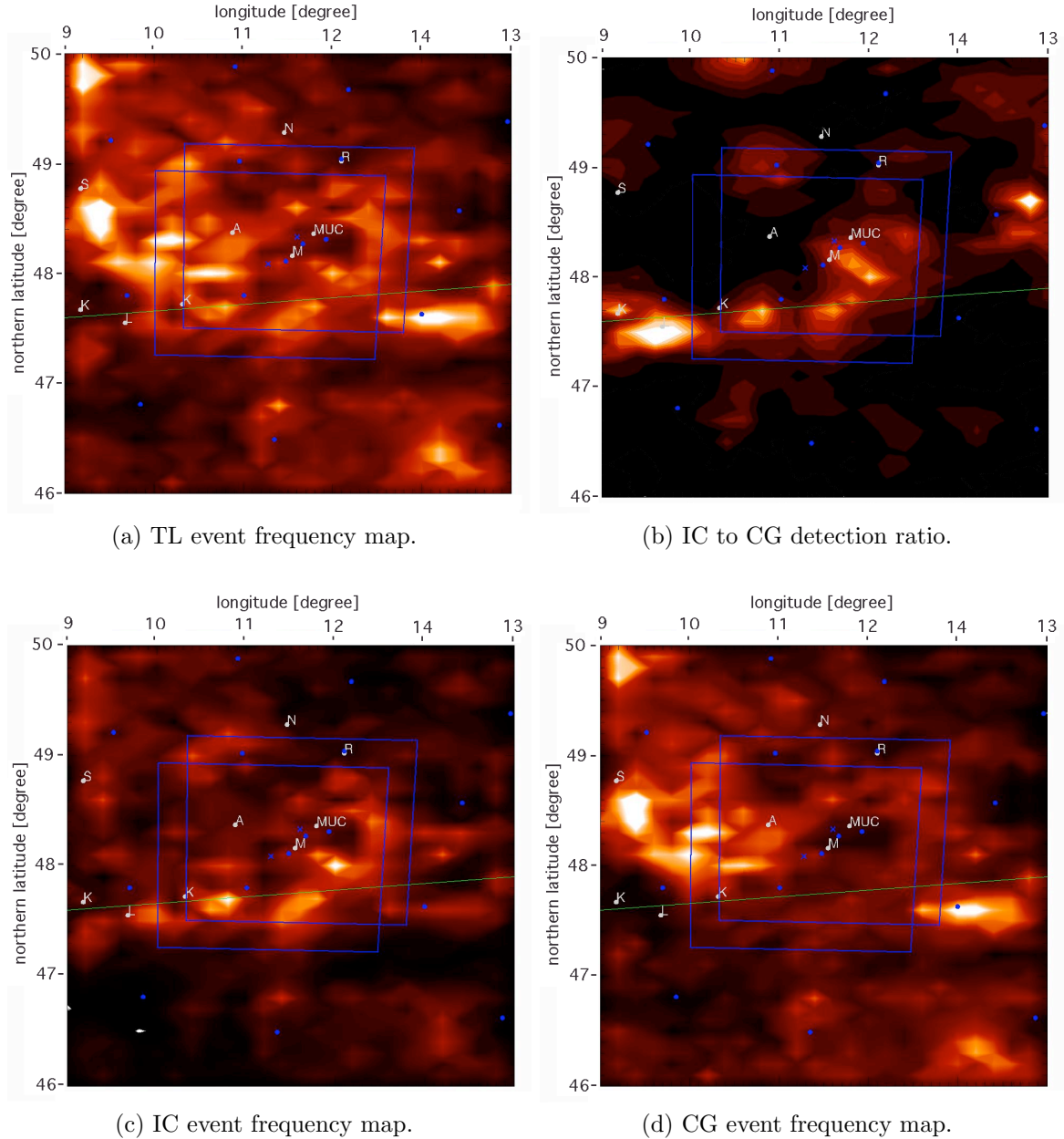


Figure 3.14: Relative sensitivity maps showing local (a) TL, (b) IC to CG, (c) IC, and (d) CG discharge occurrence for lightning events with amplitudes greater than 2.5 kA. High values are white, low values black shaded. The lower threshold for white shades are for (a) 5 500, (b) 3, (c) 3 300, and (d) 4 500. The table lists respective uppermost threshold of the contour levels. Values above these thresholds are white colored in the graphs. The lower the values, the darker the red shade. Zero values are black. The map labeling is the same as in figure 3.12. Major cities of south Germany are indicated by white letters (M - Munich, MUC - Munich Airport). The green line marks the northern edge of the alps.

the 'hot spot' characterisites in all four sensitivity maps.

Since no final conclusion can be drawn in this study, no corrections were introduced. But all selected case-studies discussed in section 5.1 were interpreted with respect to the maps given in 3.14. This could not be done for the statistical investigations discussed in section 5.2.

3.2.2 DWD Radar Fürholzen

Specification

The operationally available two dimensional low-level precipitation scan of the DWD C-band radar in Fürholzen provides the data basis for the automated cell tracking algorithm ec-TRAM. The DWD provides the low-level scan every 5 min on a $1 \times 1 \text{ km}^2$ grid. The radar reflectivity is given in 17 intensity levels numbered from 0 to 16 corresponding to the following reflectivity steps in dBZ: $< 5, 10, 15, 20, 25, 30, 34, 37, 40, 43, 46, 49, 51, 53, 55, 59, > 59$. The data underlay no quality control. The radar is situated approx. 20 km north of Munich at 48.3° latitude and 11.6° longitude. The scan covers $200 \times 200 \text{ km}^2$ (see figure 3.16).

Data Preprocessing

The cell identification threshold of 33 dBZ (see section 3.1.2) is found to be higher than the local detection limits in the domain. Radar-cells are identified all over the research domain, so that radar data are not preselected before inserted into the rad-TRAM routine. Within the routine, radar reflectivity patterns are smoothed with a two-dimensional Gaussian filter (see section 3.1.2).

3.2.3 DLR Radar POLDIRAD

Specification

The volumetric, polarimetric radar information was obtained by the DLR *polarization diversity Doppler radar* POLDIRAD (Schroth et al., 1988). POLDIRAD is a C-band research radar which is located at the DLR in Oberpfaffenhofen, approximately 30 km west of Munich (see figure 3.16). The radar is fully polarized which means that beside the two standard polarizations, horizontal and vertical, it can emit every possible superposition of the two polarizations including elliptical and circular polarized EM-waves. In this study only vertically and horizontally polarized beams were used. POLDIRAD measures the backscattered signal in two separated channels, the polar and the cross-polar channel. With this feature POLDIRAD is able to assess the polarimetric radar quantities ZDR and LDR (see section 2.3.2). A more detailed technical specification is given in M. (2007).

The hydrometeor scheme used in this work is based the decision tree method illustrated in figure 3.15. The scheme is a further development of a method which was

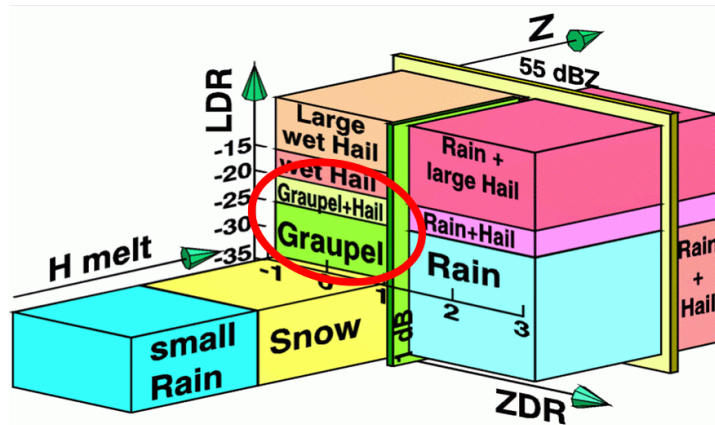


Figure 3.15: Hydrometeor classification described by Höller et al. (1994).

specifically developed for POLDIRAD by Höller et al. (1994). The method uses information about radar reflectivity, ZDR, LDR and the altitude of the melting layer. The capabilities of POLDIRAD were demonstrated in a number of projects, which investigated the formation and life-cycle of severe weather events (Höller et al., 1994; Dotzek et al., 2001)

Data Preprocessing

During the thunderstorm period 2008 the measurement strategy for POLDIRAD was focused to assess three-dimensional polarimetric radar information about thunderstorm structures over their life-cycle. Promising thunderstorms were tracked by radar scans and by eye and regularly scanned with *plan position indicator* (PPI) scans in several elevations and with *range height indicator* (RHI) scans with the purpose to complement ec-TRAM life-cycle patterns with three-dimensional radar information. The scheme presented in figure 3.15 was primarily used to retrieve the hydrometeor distribution in a thunderstorm. Because of attenuation effects, the radar scans were checked and corrected if necessary. Special emphasis was laid on a reliable graupel and hail information in the mixed phase layer and at the ground.

3.2.4 Satellite Data from cell tracking algorithm Cb-TRAM

To exploit the benefit of a combined usage of radar data, lightning data, and satellite data, the selected life-cycle diagrams, which were recorded by the ec-TRAM routine, were complemented by information provided by the satellite data-based algorithm Cb-TRAM (Zinner et al., 2008; Forster and Tafferner, 2009a). While the information from radar and lightning data can only be used for the tracking of already active thunderstorms, it is possible to detect potentially convective activity in an early state, before the onset of precipitation or lightning activity, using satellite data-based information.

The Cb-TRAM algorithm was developed at the DLR. It uses the high resolution visible (HRV), the infra-red $10.8\ \mu\text{m}$ ($IR_{10.8\mu\text{m}}$), and the infra-red $6.2\ \mu\text{m}$ (water vapor, $WV_{6.2\mu\text{m}}$) channels from the Meteosat-8 SEVIRI instrument. The update cycle is

15 min. The horizontal resolution is $1.5 \times 1.5 \text{ km}^2$ for the HRV channel and $5 \times 5 \text{ km}^2$ for the $IR_{10.8\mu\text{m}}$ and the $WV_{6.2\mu\text{m}}$ channels. Additionally, ECMWF model analyses are used to calculate the height of the tropopause based on the current temperature at every image pixel. ECMWF data are available daily at 0, 6, 12 and 18 UTC. The general working scheme of the Cb-TRAM tool is described on page 38.

The Cb-TRAM routine distinguishes three cell stages, 'convection initiation', 'rapid development', and 'mature thunderstorm'.

Stage 1: 'convection initiation' 'convection initiation' considers only rapid cloud developments, since not each cumulus will develop into a mature thunderstorm. Stage 1 identifies cloud objects which show a change in horizontal cloud extent in the HRV channel. An object consists of all connected pixels which show a cell area increase detected in the HRV channel, which is accompanied by any $IR_{10.8\mu\text{m}}$ cooling. For both channels the images calculated from two consecutive time steps are analyzed to assess the temporal changes.

Stage 2: 'Rapid development' Rapid vertical growth has to be detected in the thermal spectral range to assign the stage 'rapid development' to a cell object. So stage 2 is assigned to those cloud objects which show a rapid cooling in the $WV_{6.2\mu\text{m}}$ channel. Parts of cloud tops have to be detected to grow rapidly at heights at or close to the WV tropospheric background temperature, since this is usually an indication of clouds growing close to the strong inversions in the middle troposphere or at the tropopause level. Thereby the absolute temperature must not be too cold to fulfill the criteria to stage 3. Thunderstorm cells detected at this stage can already show hazardous intensity.

Stage 3: 'mature thunderstorm' 'Mature thunderstorms' indicate the convective cell cores of mature convective cells. The algorithm searches for areas which show a $WV_{6.2\mu\text{m}}$ temperature close to or lower than the temperature of the surrounding tropopause. To distinguish the more dynamic cell core from a possible cirrus layer, additionally a large local gradient of reflectivity in the HRV channel has to be detected to assign the cell to stage 3.

A detailed description of the algorithms with the exact detection criteria used in Cb-TRAM can be found in Zinner et al. (2008). The information used for the case-studies within this work were read from the log-files of time and space coincident Cb-TRAM cells.

3.2.5 Sampling Domain and Period

The operation domain for the radar tracker is limited to the area coverage of the DWD radar in Fürholzen. This domain covers $200 \times 200 \text{ km}^2$ around the city of Munich. The lightning tracker operates on a larger domain ranging from 47.4° to 49.2° northern latitude and from 10.3° to 13.0° longitude. This area belongs to the densest part of the lightning localization network LINET, where lightning detection is found to be most accurate (Höller et al., 2009; Betz et al., 2009a). Consequently the operation domain

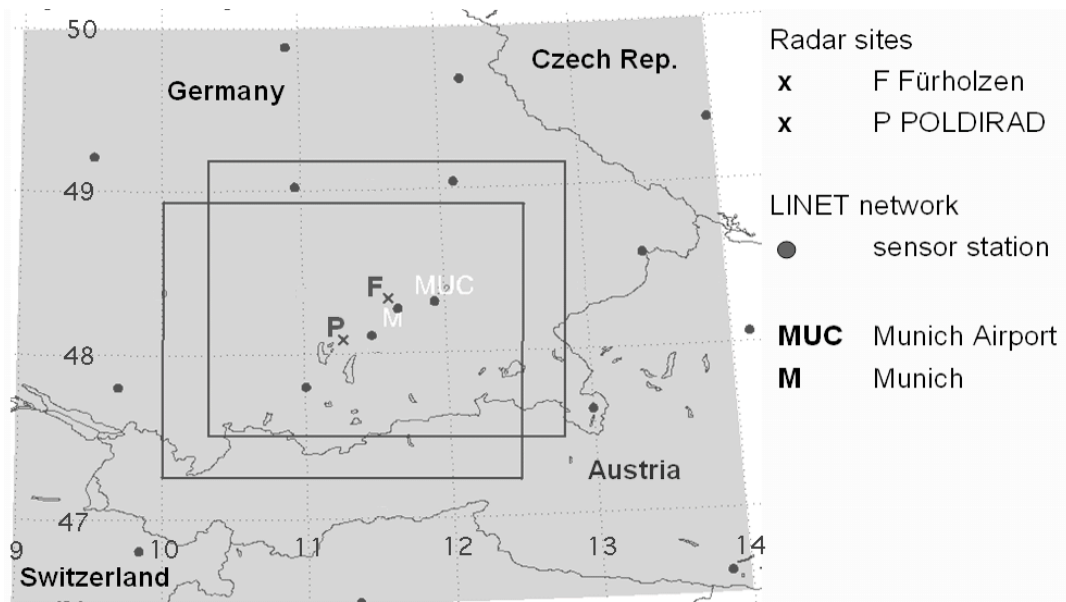


Figure 3.16: Map illustrating the sampling domain for this study. The upper right black rectangle indicates the area coverage of the DWD radar Fürholzen, the lower left black rectangle approximates the coverage of the DLR radar POLDIRAD.

for the ec-TRAM algorithm is restricted to the intersection of both domains, which is the area coverage of the DWD radar in Fürholzen. A map to illustrate the domain with radar sites and coverage as well as LINET sensor locations is presented in figure 3.16.

The area north of the Alps is well known for quickly developing and fast propagating thunderstorms. 50 thunderstorm days with all types of thunderstorm organization and all ranges of lightning activity were selected for the statistical part of this work. Two case-studies, one recorded on 25 June 2008, the other recorded on 22 August 2008, with persistent, heavy supercells were selected for a more detailed study of a thunderstorm life-cycle.

Chapter 4

Performance and Verification of the Thunderstorm Tracker ec-TRAM

In this chapter the principal approach of ec-TRAM to identify and track thunderstorms as so called *eccells* is verified. It is demonstrated, that the two-dimensional thunderstorm tracking method, developed for the ec-TRAM algorithm, assesses three-dimensional thunderstorm properties, which do not have to be tracked separately (see section 4.1). Furthermore, it is shown, that the *eccell* definition creates cell objects, which physically reasonable comprehend and describe thunderstorms. The physical meaning of the object *eccell* and its relation to the real object thunderstorm is discussed. It is shown, that the combined object *eccell* achieves a more detailed and comprehensive picture of a thunderstorm, than its single components *licell* or *radcell* alone could do. Furthermore, it is shown that the tracking method, employed in the ec-TRAM algorithm, is coherent and stable, outperforming thunderstorm tracking based on rad-TRAM or li-TRAM alone (see section 4.2).

The nowcast quality for cell location and cell extension achieved by rad-TRAM and li-TRAM are tested and found to be sufficient for this study (see section 4.3). It is also shown, that it is most likely to further improve the nowcast performance by tuning the calculation of the displacement vector field. However, a different approach to nowcast lightning-cells is proposed. Methods to derive cell nowcasts for *eccells* are suggested.

The chapter concludes with an overview of the cell database, which has been established with the ec-TRAM algorithm based on data, which were recorded during the thunderstorm period 2008 (see section 4.4). The general *eccell* composition is discussed as well as statistical distributions of selected cell parameter. Here, the area distribution of *licells*, *radcells*, and *eccells* are compared and the statistical occurrence of selected discharge parameters found in *licells* are presented.

Finally, the lifetime distributions for life-cycles assessed by the li-TRAM, rad-TRAM, and ec-TRAM tracking method are discussed. It appears, that two regimes, one including rather short-lived cells and one including more persistent cells, are reflected in all three lifetime distribution graphs. The composition of *eccell* life-cycles are discussed in

more detail. Herein, it is found that the vast majority (about 70 %) of considerably long lasting life-cycles, recorded with the ec-TRAM algorithm, start with strong ground precipitation and end with strong ground precipitation. A smaller fraction (about 20 %) start and end simultaneously with both, discharge activity and heavy precipitation at the ground. Only a minor part start and end with discharge activity. This is an important result, which contributes significantly to the general picture of a conceptual thunderstorm model.

4.1 Cell Identification with ec-TRAM

The definition of an *eccell* cannot be verified itself, since this is not possible for a definition as such. Instead, the hypothesis has been verified, that the application of the definition *eccell*, which includes chosen thresholds, results in a fast and reliable two-dimensional tracking method, which retains even three-dimensional thunderstorm properties, that do not need to be tracked separately.

First of all, the principal approach of ec-TRAM to correlate three-dimensionally spread lightning clusters with two-dimensional precipitation features at the ground via spatial overlap of *licells* and *radcells* (see section 3.1.4) has been verified. For that purpose, the three-dimensional reflectivity structure of several thunderstorms at different development stages and at different synoptic conditions have been overlaid by their electrical activity. An example is presented here. The thunderstorm was recorded on 25 June 2008. The storm developed in a surrounding which was characterized by high wind speeds and strong non-directional speed wind shear. The storm has been selected to demonstrate the successful performance of the ec-TRAM approach in difficult situations, when the falling precipitation is carried away from the upper cell core by strong winds. In figure 4.1 horizontal radar scans recorded at different elevation angles and a cross-section scan of the storm around 16:25 UTC are presented to illustrate the three-dimensional storm structure. All scans are complemented by lightning data from 2 min prior to 2 min after the radar scanning time. In order to demonstrate, that lightning-cells, which are identified on the basis of a plane projection of three-dimensional lightning data, can be attributed to the convective precipitation core at ground of the same thunderstorm via spatial overlap, discharge events are on purpose not sorted according to the radar inclination of the PPI scans shown in figure 4.1. It can be seen in the RHI scan presented in figure 4.1e, that IC discharges were recorded in the updraft region, which is indicated by high reflectivity values (red colors), and preferentially at the gradient from high to small reflectivity values and above (color gradient from orange to green). The ground scan and the cross-section scan show that CG events appear in the close vicinity of the high reflectivity ground pattern. The PPI scan sequence given from figure 4.1a to figure 4.1d, and especially figure 4.1a, illustrate clearly that TL activity is found mostly in regions of high reflectivities and therefore can indeed be associated with high reflectivity ground pattern of the same thunderstorm via spatial overlap. This correlation was found in the other example storms, too, including less active and less developed storms. With this result the ec-TRAM approach is considered as verified.

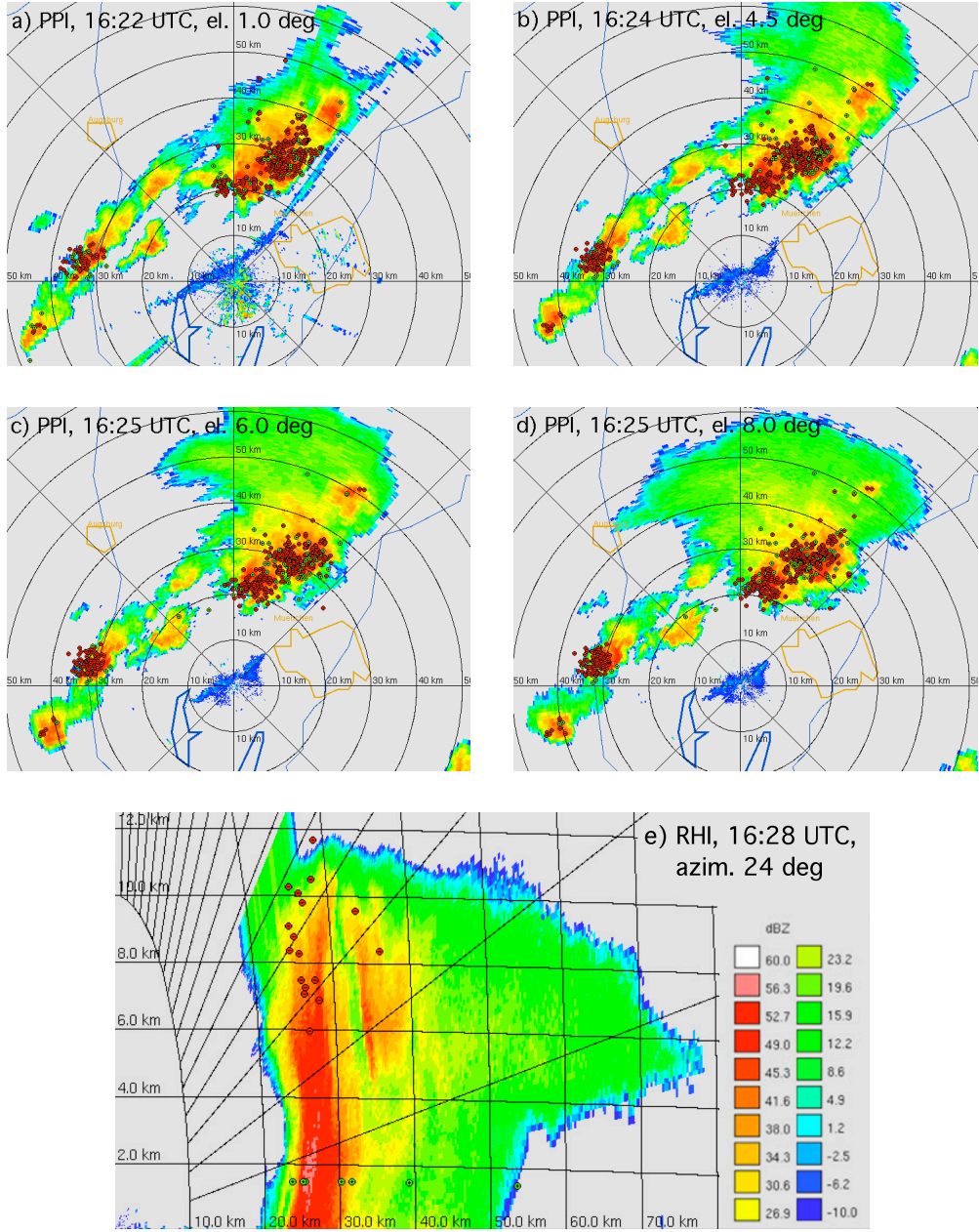


Figure 4.1: Reflectivity scans of the example storm recorded by POLDIRAD on 25 June 2008. Electrical discharge events recorded by LINET from 2 min prior to 2 min after the radar mapping times are illustrated as points. Red points indicate IC events, green points CG events. a to d) PPI scans recorded with different elevation angles. e) RHI scan. To visualize CG events they are plotted at 1.5 km height although, actually, a zero altitude is attributed to them.

With the principal approach to identify *eccells* verified, the following studies were performed to achieve proper cell definitions for radar and lightning-cells. The focus hereby is laid on three aspects. Firstly, it is aimed to achieve an efficient cell assignment, which means that as many cells as possible are attributed to cells of the other cell type. But

since the cell assignment-efficiency is sensitive to the cell area, it can artificially be improved by enlarging the cell area of one or of both cell types. So secondly, the efficiency of the cell overlap has been tested, to sort those cell definitions out which have a rich overlap. And finally, the performance of ec-TRAM and the physical plausibility of all three cell types, *eccell*, lightning-cell, and radar-cell has been visually verified.

Several parameter-sets to tune the cell-identification of *radcells*, *licells*, and therewith consequently the identification of *eccells*, were tested. They are listed in table 4.1. The other adjustments were not altered. The terminology, used here, follows the description of the procedural steps given in section 3.1 and summarized in the scheme of figure 3.4. In the case of radar-cell definition, different reflectivity thresholds to identify cell-cores were tested. They have been set with respect to the radar reflectivity intervals given by the provider (see section 3.2.2). Because the reflectivity-value map is smoothed with a Gaussian filter before the actual cells are identified, the thresholds are set 1 dBZ below or above the respective interval limits. In the case of lightning-cell definition, the data accumulation interval and the search radius were altered. The data accumulation times were set to allow the cell tracking via 'time-overlap' method (see section 3.1.3), which means that the accumulation intervals had to overlap when lightning-cells are defined in 5.0 min or 2.5 min time steps.

To assess the cell assignment-efficiency for a special set of cell identification parameters, the fraction of cells, which could not be assigned to time-coincident other cells was calculated. If σ_t^L is the number of lightning-cells at time step t , which can be assigned to one or more time-coincident radar-cells and $\bar{\sigma}_t^L$ is the number of lightning-cells at time step t , which cannot be associated to time-coincident radar-cells the cell-assignment efficiency for lightning-cells can be expressed as

$$E_{assign}^L = \frac{\sum_{t \in T} \bar{\sigma}_t^L}{\sum_{t \in T} (\sigma_t^L + \bar{\sigma}_t^L)}. \quad (4.1)$$

Hereby, T denotes the set of all available time steps. A zero value for E_{assign}^L indicates a perfect cell assignment, meaning that all lightning-cells were correlated with time-coincident radar-cells. In the worst possible situation, if no lightning-cell was assigned to a time-coincident radar-cell, E_{assign}^L achieves 1. Since this fraction lacks information about the assignment-efficiency from radar-cells to lightning-cells, the same calculations were done for radar-cells.

To achieve a measure of the cell overlap-efficiency, the following calculations were done for each parameter-set. In the case of lightning-cells, the fraction of non overlapping lightning-cell area to the total-lightning-cell area is calculated for each time step $t \in \tau$. τ comprises all those time steps, where radar and lightning-cell actually coexist. It is defined as subset of T with

$$\tau = \{t \in T : c_t^R \neq \{\} \wedge c_t^L \neq \{\}\}. \quad (4.2)$$

Following the terminology introduced in section 3.1.1, with C_t^L as the bicolored [0/2] lightning-cell map and \vec{X} as the set of pixel on the general map grid, the set of non-zero cell pixel c_t^L on the lightning-cell map at time step t is defined as

$$c_t^L = \left\{ \vec{x} \in \vec{X} : C_t^L(\vec{x}) = 2 \right\}. \quad (4.3)$$

Consequently, the set of non-zero cell pixel c_t^R on the bicolored [0/1] radar-cell map C_t^R at time step t is defined as

$$c_t^R = \left\{ \vec{x} \in \vec{X} : C_t^R(\vec{x}) = 1 \right\}. \quad (4.4)$$

The sets c_t^R and c_t^L , defined in equation 4.4 and equation 4.3, comprise those grid pixels, which are covered by radar and lightning-cells at time step t , respectively. The cell coverage-efficiency $E_{coverage}^L$ for lightning-cells can now be expressed as the fraction

$$E_{cover}^L = \frac{\sum_{t \in \tau} |(c_t^R \cup c_t^L) \setminus (c_t^R \cap c_t^L)|}{\sum_{t \in \tau} |c_t^L|}. \quad (4.5)$$

In equation 4.5 $|A|$ denotes the cardinality of a set A and $A \setminus B$ the difference between two sets A and B defined as $A \setminus B = \{x \in A : x \notin B\}$.

Since only time steps were used to compute E_{cover}^L , where radar and lightning-cells coexist, the optimum cell coverage achieves a zero value. This is the case, if all lightning-cells are totally covered by time-coincident radar-cells. The bigger the offset of overlapping cells, the higher E_{cover}^L gets. The worst case, which means no cell coverage at all, would be indicated by 1. Since this fraction does not give the cell coverage-efficiency for radar-cells, the same calculations were done for radar-cells.

To compare different cell identification parameter-sets, the two efficiency values for cell assignment and cell coverage are computed for the 25 June 2008 and plotted in diagrams with the lightning related values on the abscissa and radar related value on the ordinate. The results are presented in figure 4.1. The left-hand diagrams in figure 4.1 illustrate the cell assignment-efficiencies E_{assign}^R versus E_{assign}^L , the right-hand diagrams the area-coverage efficiencies E_{cover}^R versus E_{cover}^L . Generally, the closer a correlation point comes to the origin, the better the requirements are fulfilled. The favored correlation points are enlarged in all diagrams. In each row of figure 4.1 another onset time was set in relation to the radar mapping time for the lightning data accumulation. For the studies shown in figure 4.2a and figure 4.2b the accumulation time-interval ends with the corresponding radar mapping time. For the studies presented in figure 4.2c and figure 4.2d the accumulation time-interval starts at twice the time-interval prior to the respective radar mapping time, and for the studies of figure 4.2e and figure 4.2f the accumulation time-interval starts at half the time-interval prior to the respective radar mapping time. The diagrams in figure 4.2a and figure 4.2b compare the complete set of cell identification parameters as listed in table 4.1. The best eight parameter-sets of this study were used for the residual studies presented in the other four diagrams. Since the occurrence of lightning is a more reliable indication than strong precipitation at ground to identify thunderstorms, the main focus of this study is laid on a good lightning-cell performance. This can be identified in the correlation diagrams by low values on the

Table 4.1: Parameters for radar-cell and lightning-cell identification, which were tested for their cell assignment quality in the study presented in figure 4.2. The finally selected parameter setting is highlighted.

| <i>radcell</i> identification threshold | licell cell clustering | |
|---|------------------------|---------------------|
| minimum reflectivity | accumulation time | minimum distance |
| 29 dBZ, 33 dBZ , 41 dBZ | 3 min , 6 min | 6 km , 10 km |

abscissa.

Out from the correlation diagrams shown in figure 4.2a and figure 4.2b, four parameter pairs are considered as reasonable adjustments for cell identification. They correspond with radar-cell identification based on reflectivity thresholds of 33 dBZ and 41 dBZ and a lightning-cell definition based on accumulation times of 3 min and 6 min and a search radius of 6 km. The parameter-sets, which comprise a radar-reflectivity threshold of 29 dBZ and a search radius of 6 km, achieves also good values for both accumulation times. But the sets were rejected, because a reflectivity threshold of 29 dBZ is considered as too low to distinguish effectively separate convective precipitation cores, if they are embedded in stratiform rain regions. Instead, a reflectivity threshold of 33 dBZ is supposed to be low enough to detect the intense rain fields of thunderstorms in a quite early state and to be high enough to distinct separate precipitation cores in stratiform rain regions.

A search radius of 6 km was selected to identify coherent discharge regions in a storm, because it turned out that lightning-cells become disproportionately large in comparison with radar-cells defined by a 33 dBZ threshold, if they are clustered with a search radius of 10 km. A search radius of 6 km might occasionally miss outliers, but electrically active cores are identified well and enveloped by reasonable large cell contours. The temporal evolution of lightning-cell parameters during the life-cycle of six example thunderstorms has been compared for both data accumulation time-intervals (not shown). Since they revealed similar pronounced parameter variations this study did not influence the final determination of the cell identification parameter-set.

By comparing the diagrams of all three rows in figure 4.2 the time-interval to accumulate the discharge events for cell clustering is set, that it ends with the corresponding radar mapping time. Since the efficiency values for the lightning-cells did not change significantly for all three tested onset times, the improvement for the radar-cell assignment became the crucial factor for this decision.

To summarize the results of this study, a radar-reflectivity threshold of 33 dBZ is set, to identify intense ground precipitation as *radcells*, and an accumulation time-interval for lightning data of 3 min and a search radius of 6 km is set, to identify coherent discharge regions as *licells*.

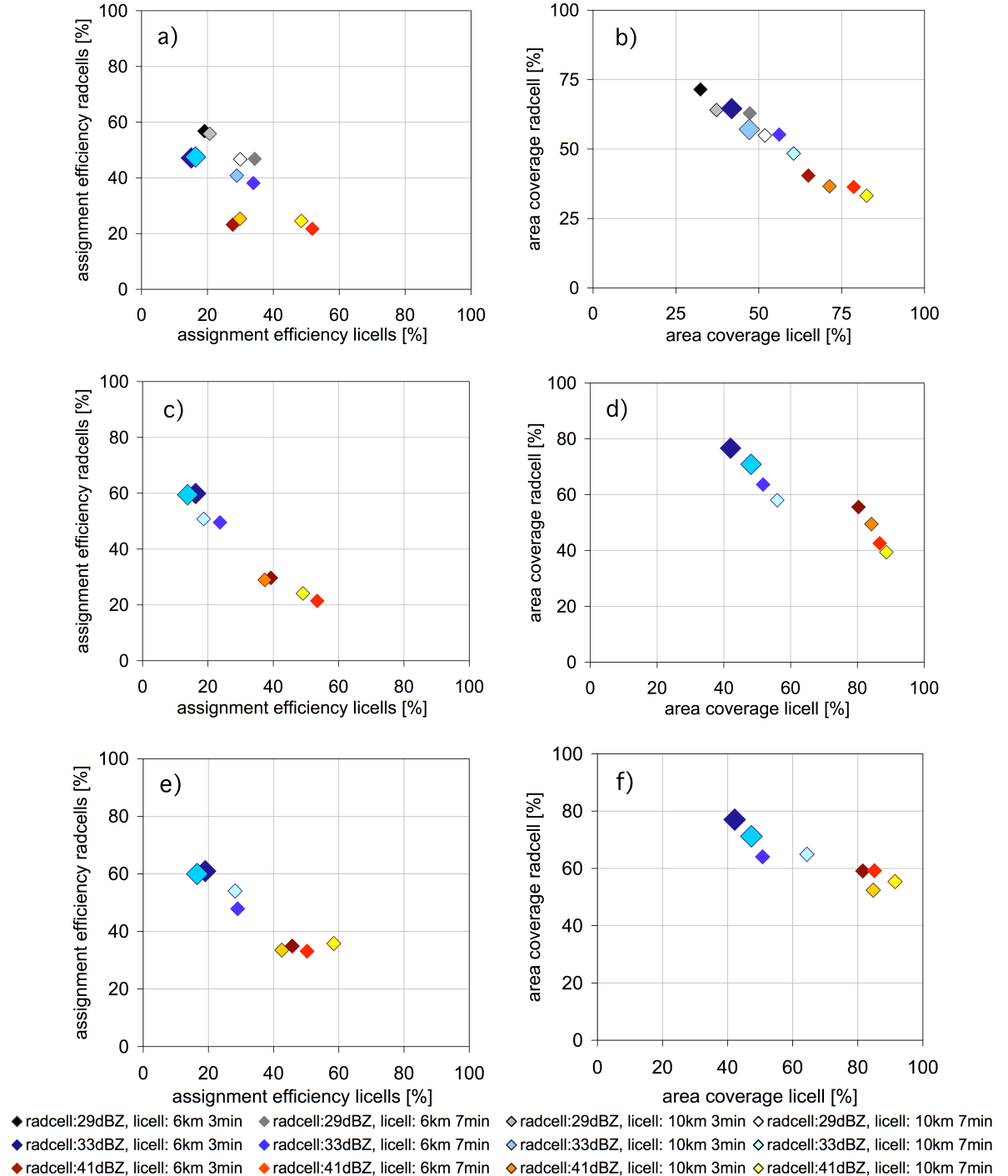


Figure 4.2: Correlation diagrams of cell assignment-efficiencies (left side) and cell coverage efficiencies (right side) in percent for selected cell identification parameters (listed in table 4.1) computed for 25 June 2008. The correlation points marking the two favored parameter pairs are highlighted. The label *radcell: 33, licell: 6 km 3 min*, for example, refers to the correlation of radar-cells identified by a reflectivity threshold of 33 dBZ and lightning-cells defined based on 3 min data accumulation and a search radius of 6 km. The lightning data accumulation time-interval ends with the radar mapping time (a, b), starts at twice the accumulation time interval prior to the radar mapping time (c, d), starts at half the accumulation time prior to the radar mapping time (e, f).

4.2 Cell Tracking with ec-TRAM

The performance of the cell tracking algorithm ec-TRAM is illustrated by an example storm which was tracked and monitored by the ec-TRAM algorithm on 15 May 2008. To illustrate the coherent and reasonable storm tracking achieved by the ec-TRAM approach, figure 4.3 shows key snapshots of two time sequences of the example thunderstorm. The snapshots demonstrate, that the algorithm monitors a thunderstorm in its entirety, which can be composed of one or more single components. The total storm cell history indicates, too, that the ec-TRAM approach is justified. The cell records show, that the cell constituents behave as an entity and obviously influence each others development, since throughout the complete life-cycle cells merge and split. Exemplarily the two time sequences, presented in figure 4.3, are chosen to illustrate this statement graphically. The entire life-cycle is discussed in the following.

To give insight into the information fusion of *licell* and *radcell* to an *eccell*, table 4.2 on page 72 shows an excerpt of the respective database entries of the same storm, which is shown in figure 4.3. The storm evolution is completely assessed, as entity as well as in the superposition of every single component. In this example a cell tracking based on rad-TRAM or li-TRAM alone would have failed to track the storm completely as it will be shown in the next paragraph.

It can be seen in table 4.2 that every table entry (row) is marked by a unique id. The first three cell attributes (columns) store the cell date, cell time, and cell number. This information links unambiguously those database entries, which belong to one *eccell* track. It can be seen in the table that the example storm, recorded as *eccell* number 13, was recorded on 15 May 2008 from 12:35 UTC to 14:55 UTC. The next two cell attributes refer to the *eccell* composition. A cell, which consists of only one *radcell*, is labeled 'rad', a cell, which consists of only one *licell*, is labeled 'li', and a cell, which consists of both cell types, is labeled 'ec'. The column 'first_entry' shows the cell type of the first cell entry and does not change throughout the whole cell life-time. The column 'last_entry' shows the actual cell type for every time step and finally the cell type of the last cell entry. It can be seen that the example storm consisted for the first 15 min and at 14:30 UTC of only one *radcell*. During the rest of its lifetime the storm consisted of a combination of both cell types. The next two attributes, named 'sum_licell' and 'sum_radcell', record the number of *licells* and the number of *radcells*, which compose the actual *eccell* complex. The actual cell numbering of the single *eccell* constituents are listed for *licells* as 'nr_licell' and for *radcells* as 'nr_radcell'. Beside the cell numbers, the unique respective cell entry 'ids' (identify numbers) are stored. The 'ids' link the *eccell* to the original cell entries of its cell constituents, which were recorded by the rad-TRAM and li-TRAM algorithms and stored in separate tables (see section 3.1.5 and appendix A.4). From the time history of the columns 'nr_licell' and 'nr_radcell' it can be seen, that the li-TRAM algorithm would have failed to track the storm from time-step 12:55 UTC to 13:00 UTC (*licell* number 11 disappears) and at 14:30 UTC, whereas the rad-TRAM algorithm would have lost the track from time-step 14:00 UTC to 14:05 UTC (*radcell* number 9 disappears). This can be noted from the table as at

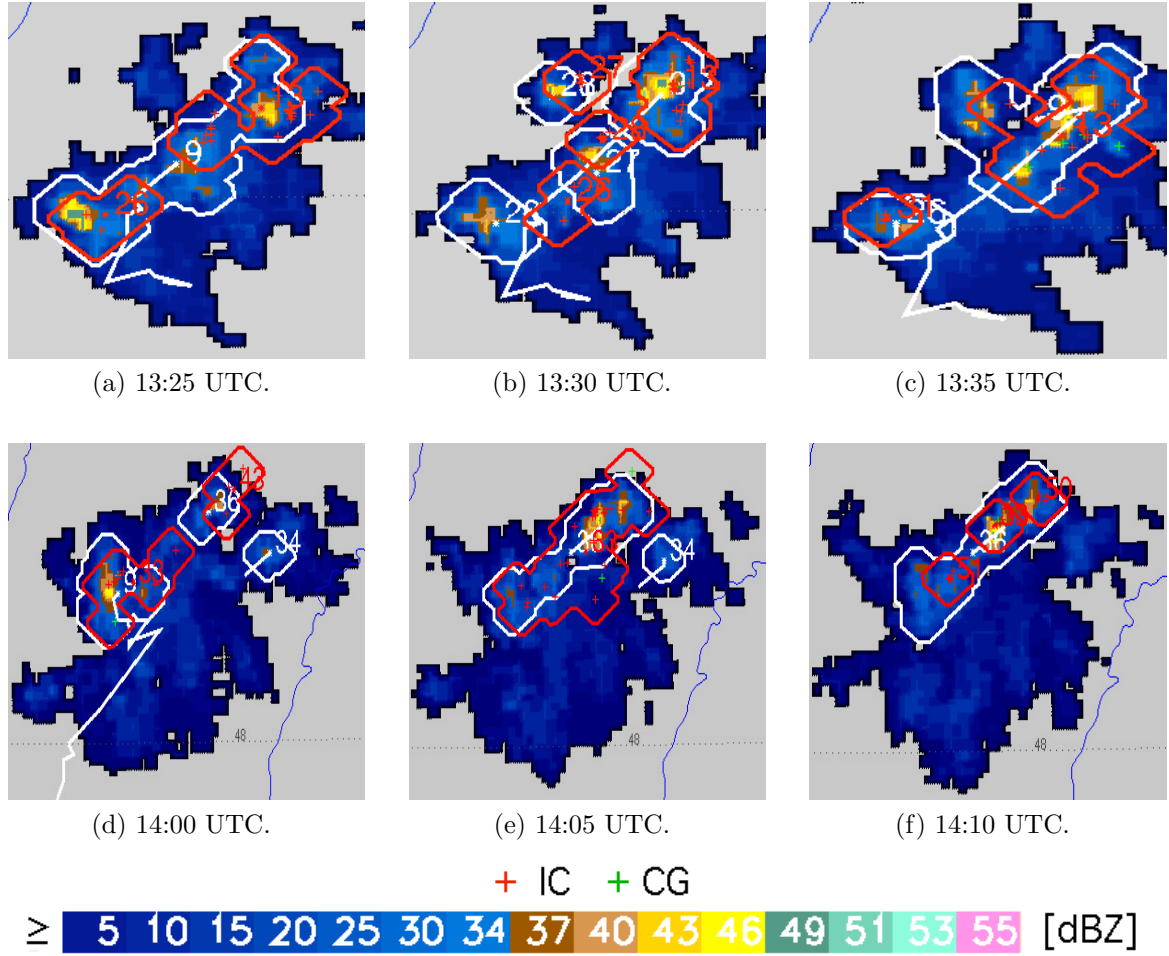


Figure 4.3: Ec-TRAM snapshots showing two time sequences of the example storm recorded on 15 May 2008. Cell contours, cell centers, cell numbers, and, for *radcells* only, cell tracks are marked. *licell* parameters are colored red, *radcell* parameters white. Electrical discharge events of 3 min are indicated by crosses, CG events by green crosses, IC events by red crosses.

13:00 UTC and 14:30 UTC no lightning-cell number is pursued to the subsequent *eccell* entry and at 14:00 UTC no radar-cell number is pursued to the next time-step. The ec-TRAM visualization confirms this statement. At those times the respective cell records were closed and new ones opened, which means that the corresponding cell-tracks are indeed interrupted. The interruption of the radar-cell track is graphically illustrated in the upper time sequence of figure 4.3.

The example also illustrates that the tracking object *eccell* is able to consider the whole storm complex, which can consist of more than one lightning or precipitation core. The database entry at 13:30 UTC clearly highlights that point, since the cell consists of no less than four *licells* and four *radcells* at this time (see figure 4.3b and table 4.2). The respective time sequence of ec-TRAM maps, presented in the upper

graphs of figure 4.3, illustrates a general problem of a proper cell identification. It can be seen from the color shading of the radar-reflectivity, that a radar-cell can include several internal cores. This makes clear that a proper cell definition always depends on the purpose and the interpretation on the cell definition. Since the evolution of the cell complex illustrates, that the *eccell* components are close enough to influence each other, this case study is taken as indication, that the object *eccell* comprises physically reasonably active discharge and precipitation regions of a thunderstorm. It has to be pointed out, that with the approach of ec-TRAM the way to look at thunderstorms changed from more or less single cores of a storm to core complexes. The example cell has been selected, because it undergoes an unusual unsteady cell evolution, so that the strengths as well as the shortages of ec-TRAM can be discussed. It has to be pointed out, that the complexity of this case study is the exception and not the rule. The majority of *eccell* life-cycles undergo a much smoother cell evolution, which makes it yet easier for ec-TRAM to achieve a complete picture of the storms' evolution.

The storm track of *eccell* number 13 from the 15 May 2008 illustrates exemplarily that the ec-TRAM approach achieves a more coherent cell tracking than it would be done based the algorithms rad-TRAM or li-TRAM alone. To validate this statement the lifetime distributions of all cell tracks recorded during 2008 by the three tracking routines li-TRAM rad-TRAM, and ec-TRAM were calculated (see figure 4.4). To facilitate a comparison, the three distribution functions are plotted as box-and-whisker plots, which are complemented by the mean lifetimes. A description of the box-and-whisker plots used in the present work is given in appendix A.2. Since the focus of this study is laid on a comparison of higher lifetimes, a threshold of a minimum lifetime duration of 35 min is set. This has been done to avoid that too short cell tracks dominate the distribution and hinder a proper comparison by distorting the statistical values to small values. But shorter lifetimes do exist since the algorithms assess and track special thunderstorm features and not the thunderstorms in its entireties. The full lifetime frequency distributions are shown in figure 4.8 on page 78. Figure 4.4a illustrates the lifetime distributions for cell tracks which were completely recorded within the research domain. Cell tracks which pass the domain, enter the domain and end there, or start in the domain and leave it are excluded from the calculation. It can be seen that the lifetime distribution of *licell* tracks is shifted to shorter values, whereas the lifetimes of *radcell* and *eccell* tracks have similar distributions. Another study, presented in figure 4.4b, was performed which considers all cell tracks, considering complete as well as incomplete tracks, due to domain limits. While for *licell* and *radcell* tracks the lifetime distributions do not change significantly in comparison to the statistic shown in figure 4.4a, the lifetime distribution for *eccell* tracks is clearly shifted to higher values.

Since only complete life-cycles are considered in the first study, it is possible that lifetime distributions are restricted to shorter values due to the limited research domain. Although this result cannot be considered as a final proof, it indicates that tracks achieved by the ec-TRAM approach would gain, probably significantly, longer cell tracks and higher lifetimes, if life-cycles were not truncated by the domain margin. This result in combination with the proof of a physically reasonable cell tracking from the previous

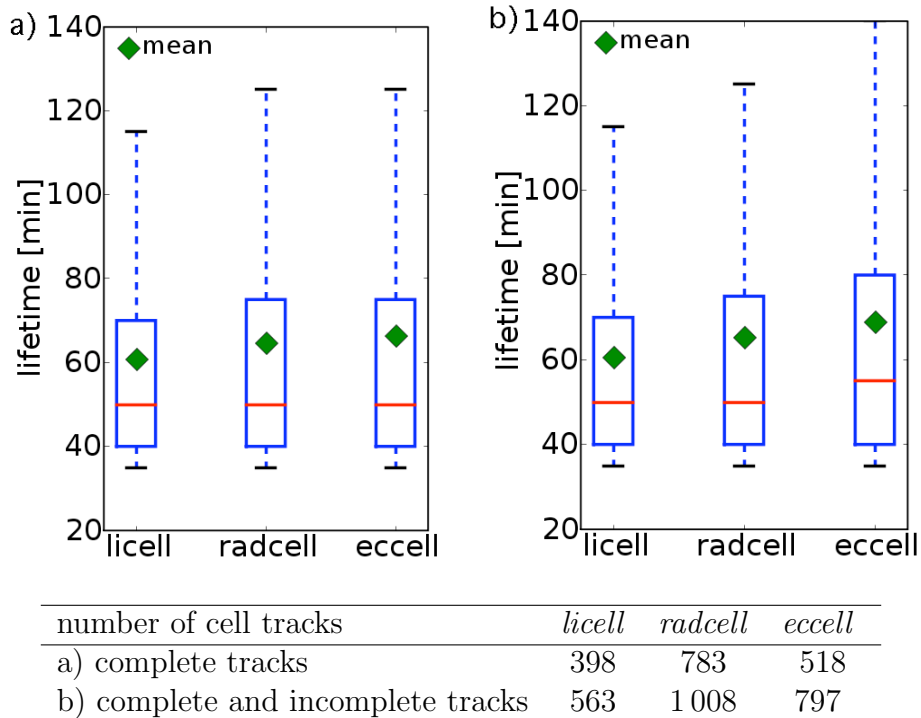


Figure 4.4: Comparison between frequency distributions of cell lifetimes calculated by the tracking algorithms li-TRAM (licell), rad-TRAM (radcell), and ec-TRAM (eccell) based on the complete data set recorded during the summer season of 2008. The minimum duration is set to 35 min (see text). The median, the 25th and the 75th quantile are plotted as red-blue box-and-whisker plots and the respective mean lifetimes are added as green diamonds (see appendix A.2). The respective number of life-cycles is listed in the table below. (a) Distributions for cells which are entirely recorded from growth till dissipation in the domain. (b) Distributions for all recorded life-cycles including complete and incomplete life-cycles.

study, demonstrates, that the ec-TRAM approach indeed achieves a more coherent and accurate cell tracking.

Table 4.2: Selected database entries for *eccell* number 13 from 15 May 2008. Cell entries shown in figure 4.3 are emphasized.

| id number | time [UTC] | first_entry | last_entry | sum_licell | sum_radcell | nr_licell | nr_radcell | figure |
|------------|--------------|-------------|------------|------------|-------------|-----------------------|----------------------|--------------------|
| 27 | 12:35 | rad | rad | 0 | 1 | | 9 | |
| 35 | 12:40 | rad | rad | 0 | 1 | | 9 | |
| 42 | 12:45 | rad | rad | 0 | 1 | | 9 | |
| 48 | 12:50 | rad | ec | 1 | 1 | 11 | 9 | |
| 56 | 12:55 | rad | ec | 1 | 1 | 11 | 9 | |
| 63 | 13:00 | rad | ec | 1 | 1 | 13 | 9 | |
| 69 | 13:05 | rad | ec | 2 | 1 | 13, 17 | 9 | |
| 76 | 13:10 | rad | ec | 3 | 1 | 13, 17, 21 | 9 | |
| 82 | 13:15 | rad | ec | 2 | 1 | 13, 25 | 9 | |
| 89 | 13:20 | rad | ec | 2 | 2 | 13, 26 | 9, 23 | |
| 94 | 13:25 | rad | ec | 2 | 1 | 13, 26 | 9 | figure 4.3a |
| 98 | 13:30 | rad | ec | 4 | 4 | 13, 26, 27, 28 | 9, 26, 27, 28 | figure 4.3b |
| 104 | 13:35 | rad | ec | 1 | 1 | 13 | 9 | figure 4.3c |
| 110 | 13:40 | rad | ec | 2 | 2 | 13, 33 | 9, 32 | |
| 116 | 13:45 | rad | ec | 3 | 1 | 33, 13, 39 | 9 | |
| 123 | 13:50 | rad | ec | 2 | 1 | 33, 39 | 9 | |
| 129 | 13:55 | rad | ec | 1 | 1 | 33 | 9 | |
| 134 | 14:00 | rad | ec | 1 | 1 | 33 | 9 | figure 4.3d |
| 141 | 14:05 | rad | ec | 1 | 1 | 33 | 36 | figure 4.3e |
| 149 | 14:10 | rad | ec | 3 | 1 | 33, 50, 51 | 36 | figure 4.3f |
| 154 | 14:15 | rad | ec | 1 | 1 | 50 | 36 | |
| 162 | 14:20 | rad | ec | 1 | 1 | 50 | 36 | |
| 165 | 14:25 | rad | ec | 1 | 1 | 50 | 36 | |
| 171 | 14:30 | rad | rad | 0 | 1 | | 36 | |
| 175 | 14:35 | rad | ec | 1 | 1 | 60 | 36 | |
| 179 | 14:40 | rad | ec | 2 | 2 | 60, 64 | 36, 49 | |
| 186 | 14:45 | rad | ec | 1 | 1 | 64 | 49 | |
| 193 | 14:50 | rad | ec | 1 | 1 | 64 | 49 | |
| 202 | 14:55 | rad | ec | 1 | 1 | 64 | 49 | |

4.3 Cell Nowcasting and Nowcast Quality with ec-TRAM

The verification parameters *probability of detection* (POD), *false alarm ratio* (FAR), and *critical success index* (CSI) are used to evaluate and compare the nowcast quality of cell position and cell extension assessed by li-TRAM and rad-TRAM by comparing the nowcasts computed from past data with actual measurements. The definition of the verification parameters are given in appendix A.3.

The left diagram in figure 4.5 illustrates the nowcast quality as a function of forecast time achieved by the algorithm rad-TRAM. The continuous lines refer to cell nowcasts calculated from radar data provided by DWD radar in Fürholzen. It can be seen in the diagram that for a twenty minute nowcast the POD falls below 50 % whereas the FAR exceeds the 50 % mark already for a forecast time of ten minutes. A comparison reveals that cell nowcasts based on this data source have a poorer skill than cell nowcasts calculated on base of the larger scaled German radar composite data, which are shown as dashed lines in the left diagram of figure 4.5. Rad-TRAM was originally optimized for the German radar composite which operates on a 15 min and $2 \text{ km} \times 2 \text{ km}$ time-space resolution, before it was transposed to radar data provided by the radar in Fürholzen which offers a higher time-space resolution. The comparison suggests, that the nowcast accuracy for *radcells* based on high resolution radar data can be improved by optimizing the calculation of the displacement vector field. Since cell nowcasts for a forecast time of 5 min are found to be good enough to track precipitation cores (see section 3.1.2), this work has been delayed.

The right diagram in figure 4.5 illustrates the nowcast quality as a function of forecast time for cell nowcasts calculated by li-TRAM with different parameter settings for the displacement vector field calculation (see section 3.1.1). Different pyramidal levels, and thus different resolution steps, and different Gaussian filter widths have been tested. A comparison between the two settings suggests, that the nowcast accuracy can be further improved by adjusting the calculation settings of the displacement vector field. But in contrast to radar or satellite data based cells, lightning-cells are discrete objects with high temporal fluctuations and which are not embedded in more slowly evolving larger scale patterns. Therefore it might be principally better to use an extrapolation method based on pure cell tracking instead of area tracking (see section 2.4.2) to further improve the nowcasts quality for lightning-cells. Since it was not needed for the cell tracking method (see section 3.1.3), further efforts to improve the nowcast quality were delayed.

A possible method to calculate spatial nowcasts for *eccells* is, to apply the more reliable displacement vector field, calculated by li-TRAM or rad-TRAM, on the *eccell* objects to extrapolate *eccells* as entities. Another possibility is, to combine the two independent nowcasts of *radcells* and *licells* to compose *eccell* nowcasts in the same manner as it is done for actual *eccells* (see section 3.1.4). The focus of the present work is on the development of the ec-TRAM method, its application for thunderstorm tracking and the interpretation of cell parameter time series. Subsequent studies may

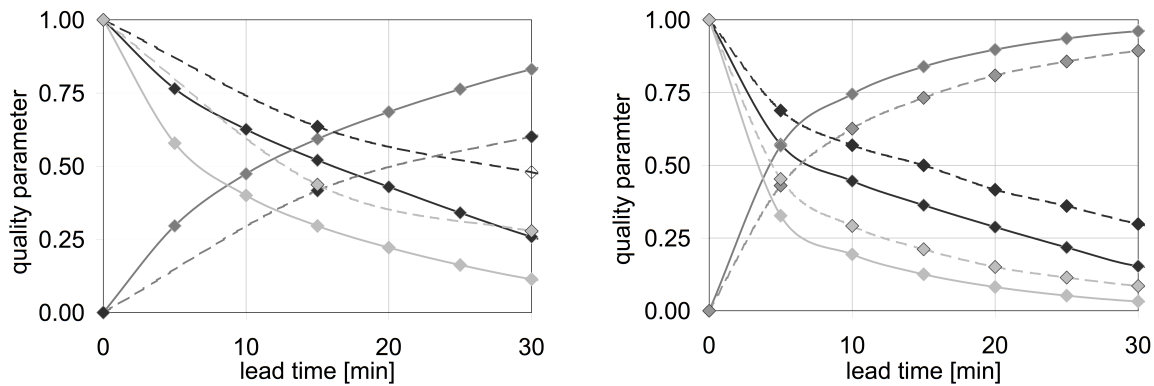


Figure 4.5: Comparison of nowcast quality parameters POD (dark grey lines), FAR (medium grey lines), and CSI (light grey lines) for cell predictions as a function of the forecast. Left: Rad-TRAM nowcast quality - DWD composite data (dashed lines) and DWD radar Fürholzen data (continuous lines). Right: Li-TRAM nowcast quality - dashed lines and continuous lines refer to different parameter settings in the calculation of the displacement vector field.

investigate the potential of nowcasting methods based on the *ecell* concept. The final method to calculate spatial nowcasts for *ecell* objects will depend on the method used to assess and nowcast cell trends.

The verification parameters used here were chosen to compare the nowcast quality of the algorithm ec-TRAM with a previous study which was performed for the rad-TRAM and Cb-TRAM algorithm (Kober and Tafferner, 2009). Furthermore, they represent a widely used method to assess the quality of thunderstorm nowcasting tools. But the information content about nowcast quality is restricted, because all three parameters penalize every not correctly forecast pixel systematically and thus lead to rapidly decreasing nowcast quality with increasing forecast time. They do not consider the distance between the nowcast pixel and the observed cell. Consequently, only correct nowcasts but not 'good' nowcasts are rewarded. Additionally the quality value depends strongly on the pixel size, which has to be considered when the nowcast quality between different nowcasting tools is compared. So it is strongly recommended to choose a more suited verification method before efforts are done to improve the nowcast quality.

4.4 Statistical Analyses of Selected Cell Parameters

The following paragraphs present a statistical analysis derived from the database, which has finally been established with the ec-TRAM routine. The complete database is generated with data, which have been collected during the thunderstorm period in 2008. For the calculations only cells, having complete life-cycles within the research domain, were used. Each cell is considered as solitary object and not in context with its cell history. The minimum cell area was set to 25 km^2 , which removes *licells* containing one

single event and insignificant *radcells*.

20 455 complete *eccells* were recorded by ec-TRAM for the 50 thunderstorm days selected during the thunderstorm season in 2008, 10 410 *licells* were recorded by li-TRAM, and 23 688 *radcells* were recorded by rad-TRAM. Out of the 20 455 *eccells* 26 % are cell complexes consisting of a combination of *radcells* and *licells*, 15 % consist of solitary *licells*. Although no *radcell* could be attributed, precipitation below the radar-cell identification threshold of 33 dBZ is possible. The remaining 60 % consist of solitary *radcells*. The fact, that no *licell* could be attributed, indicates that indeed no electrical activity was detected for the precipitation-cells. About 40 % of the total area of *eccell* complexes belong to overlapping regions. 76 % of the cell area of those *licells*, which can be attributed to time-coincident *radcells*, overlap with *radcells* and 53 % of the cell area of those *radcells*, which can be attributed to time-coincident *licells*, overlap with *licells*. This is very good agreement with the cell assignment study, presented in figure 4.2b, which is based on one example day.

73 % of those *eccells*, which comprise both, *radcell* and *licell* components, consist of exact one *radcell* and exact one *licell*. 16 % consist of one *radcell* and two or more *licells* with 2.4 *licells* per *radcell* on average. Another 5 % consist of one *licell* and two or more *radcells* with 2.1 *radcells* per *licell* on average. The residual 6 % of all *eccells* consist of a conglomerate of two or more *licells* and two or more *radcells*.

To give an idea about the magnitude range of the most important cell parameters, statistical analyses over the complete data set have been performed. The cell data have been selected using the same criteria as in the previous study. The results are illustrated by means of mean, 25th, 50th, and 75th quantile in figure 4.6 and 4.7. A comparison of the area frequency distributions between *radcells*, *licells*, and *eccells* is illustrated in figure 4.6. It can be seen, that the frequency distributions for *radcells* and *licells* have similar characteristics with a mean value around 100 km^2 . The mean area of *eccells* is found to be almost twice the size, averaging around 200 km^2 , which is reasonable, since only those *eccells* were considered in this study, which consist of two or more subcells. A comparison between the full area distributions, given on the right panel of figure 4.6, reveals that *radcell* areas appear more compact and shifted to lower values, than *licell* areas, whereas the frequency distribution for *eccell* areas is distorted to higher values. The maximum area recorded for *eccells* is 2500 km^2 , and 2000 km^2 for both, *radcells* as well as *licells*. The area distributions vary widely from day to day. Mean values range between 90 km^2 and 250 km^2 for *licells*, between 50 km^2 and 150 km^2 for *radcells*, and between 50 km^2 and 200 km^2 for *eccells* (not shown).

Frequency distributions for selected discharge parameter in *licells* were established based on the complete data set calculated by li-TRAM. For the calculations the same selection criteria as in the previous studies were used to select the cell data. The discharge values refer to a whole *licell*, which means they comprise a discharge activity of 3 min. The resulting distribution characteristics are presented in figure 4.7. It can be seen in figure 4.7a that the TL discharge activity averages around 24 events per cell.

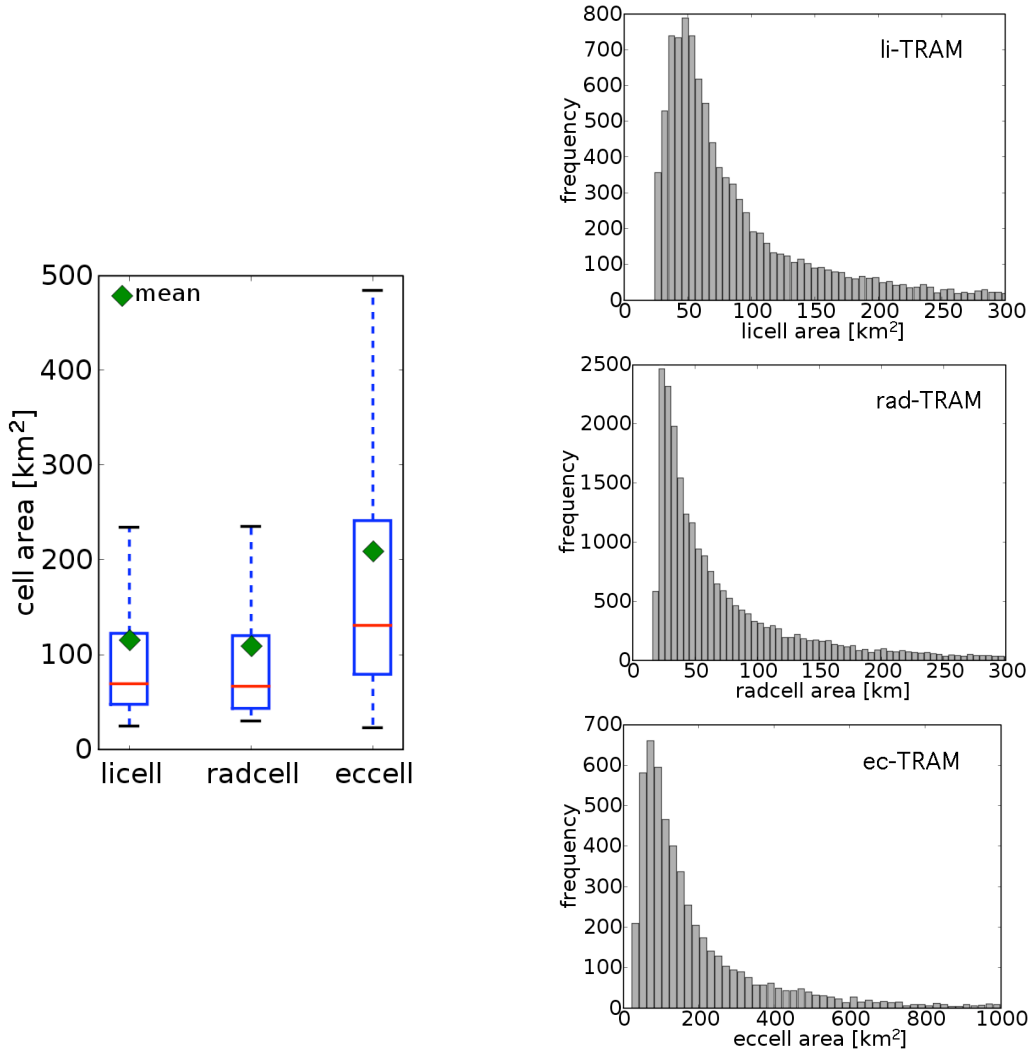


Figure 4.6: Comparison between area frequency distributions calculated by the tracking algorithms li-TRAM (licell), rad-TRAM (radcell), and ec-TRAM (eccell) based on data recorded during the thunderstorm period of 2008. Left panel: The 25th, 50th, and 75th percentile of the area distribution with cell areas of 25 km^2 and more is plotted as red-blue box-and-whisker plot (see appendix A.2). Right panel: Full area frequency distributions without a minimum threshold for *licells* (top), *radcells* (middle), and *eccells* (bottom).

The median value is found to be significantly lower at about 8 events per cell. 50 % of all cells recorded by the li-TRAM routine, exhibit a discharge activity between 5 and 18 events per cell. It can be concluded from the high offset found between median and mean, that few but high outliers exist. The maximum TL activity is found to be 950 events per cell. A high daily variation of the mean value ranging between less than 10 and 80 events per cell is found (not shown).

The frequency distribution of the TL discharge density per *licell*, shown in figure 4.7b, appears more compact than the distribution of the TL discharge activity. This indicates

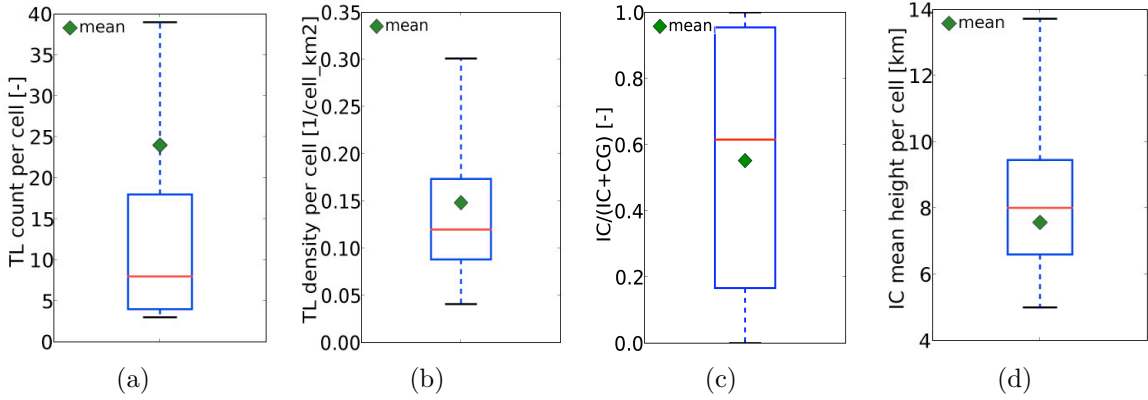


Figure 4.7: Frequency distributions for selected discharge parameters computed based on 10 264 *licell* entries. The medians, 25th, and 75th percentiles of the distribution are plotted as red-blue box-and-whisker plot (see appendix A.2). a) TL count per cell, b) TL density per cell area, d) IC percentage in relation to the total discharge activity (sum of IC and CG discharges) per a cell, and c) IC mean height per cell.

that the outliers, found in the TL activity distribution, generally correlate with corresponding large cell areas. The average density is found to be 0.15 km^{-2} and the median 0.12 km^{-2} . The maximum density found in the records is 1.1 km^{-2} . The daily means range widely between 0.1 km^{-2} and 2.5 km^{-2} (not shown).

Next, the IC contribution to the TL activity has been investigated. In this study the term TL refers to the sum of IC and CG events of a *licell* (see section 3.2.1). The selection criteria for the cell data are the same as in the previous studies. The distribution is illustrated in the graph presented in figure 4.7c. It can be seen, that the mean IC fraction in a *licell* is about 55 %. The median is found to be higher at 60 %. 50 % of all *licells* have an IC percentage between 20 % and 95 %. The IC occurrence generally outranges the CG occurrence, which is expected when considering the general IC to CG ratio in the lightning data (see section 3.2.1).

To investigate the height distribution of IC mean discharge heights per cell only cell data with discharge heights of 5 km and more were used. The distribution function is illustrated in figure 4.7d. The mean discharge height per cell averages around 7 km , the median discharge height is found to be higher around 8 km . The low distance between mean and median indicates that few and not especially high outliers exist. 50 % of all IC discharges are found at an altitude between 7 km and 9 km . This finding confirms the plausibility the altitude information of the lightning data, since it is expected that the vast majority of the discharge occur in the cloud. The daily means are found to range significantly between 7 km and 10 km (not shown).

In the following studies the tracking performance of the algorithms ec-TRAM, rad-TRAM, and li-TRAM are discussed and compared based on the complete data set

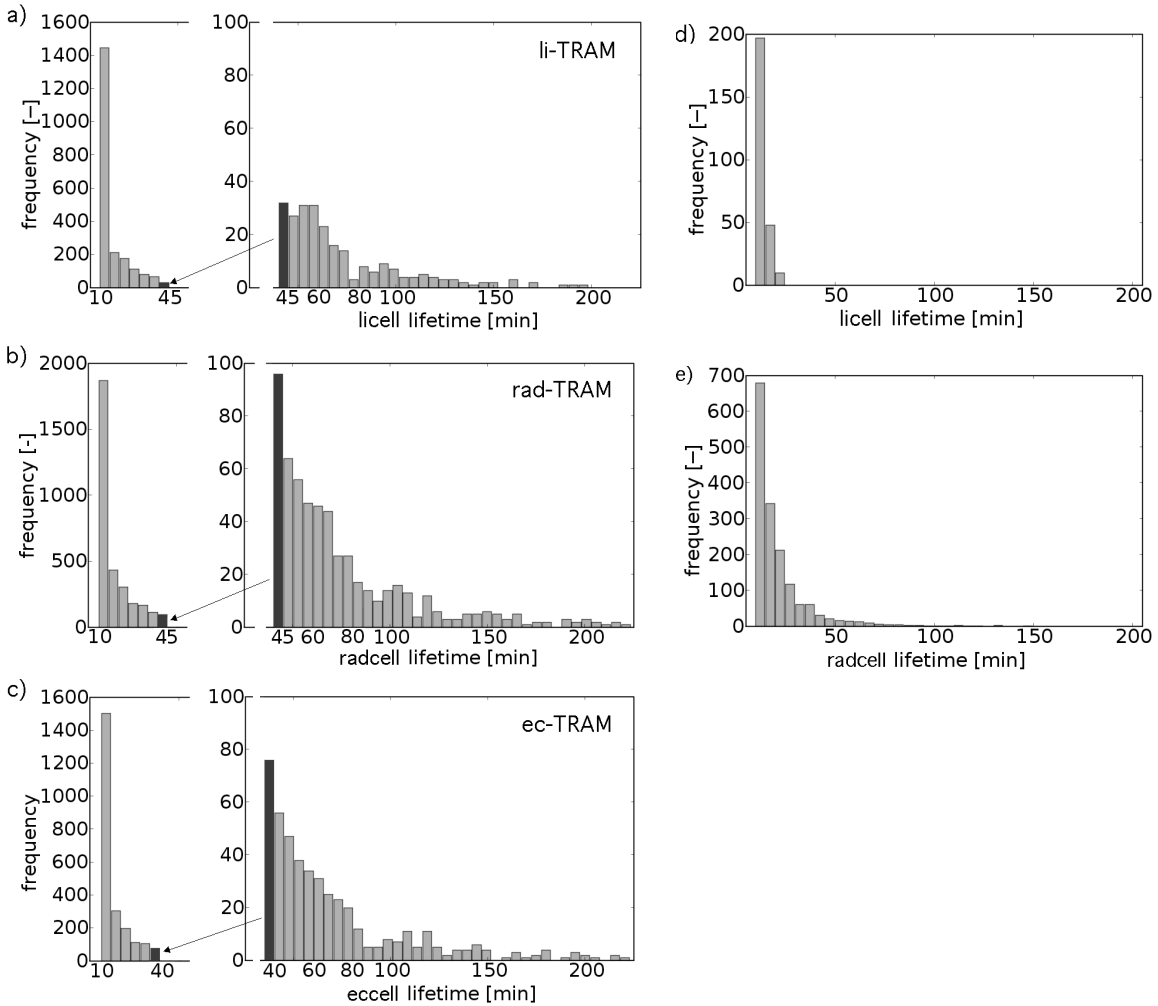


Figure 4.8: Left panel: Cell lifetime frequency distribution for (a) *licells* recorded by li-TRAM, (b) *radcells* recorded by rad-TRAM, and (c) *eccells* recorded by ec-TRAM for data from 50 thunderstorm days in 2008. The number of solitude cell entries is for li-TRAM 6 080, rad-TRAM 4 565, and ec-TRAM 3 480. For all distributions the frequency of cells with lifetimes up to 55 min is shown on separate scales. Right panel: Cell lifetime frequency distribution (full life-cycles) for pure (d) *licells* and pure (e) *radcells* recorded by ec-TRAM for data from 50 thunderstorm days in 2008.

collected during the thunderstorm period in 2008. In section 4.2 the average duration of *licell* tracks was found to range around 60 min, for *radcell* tracks and *eccell* tracks to range around 65 min (see figure 4.4a), if the minimum lifetime is set to 35 min. The distribution diagrams show, that the latter two distributions are more extended towards higher values. The median is found to be about 50 min for all three distributions. The full lifetime distributions, illustrated in the right panel of figure 4.8, reveal that the frequency of cell tracks generally decreases exponentially with increasing lifetime. In the figure the frequency distributions for lifetimes up to 40 min and 45 min and for lifetimes longer than that are shown on separate scales in order to visualize the distributions for higher lifetimes, where the count statistic becomes lower. The vast majority of cell-cycles

is found to have short lifetimes of less than 35 min in all three distribution functions. The large number of cells with lifetimes of 5 min and 10 min (one and two cell records, respectively) might be explained by sporadic cells and procedural artefacts. Generally the fact, that the algorithms assess and track only special thunderstorm features and not the thunderstorms in their real entireties might contribute to the large number of cells with very short lifetimes. But also interrupted cell tracks or split cells contribute to the large number of life-cycles found with such short lifetimes. Low organized and rather short-lived but comparably frequent single-cells might be represented in the well populated lifetime regime up to 80 min and 90 min. Although the sample size becomes poor for higher lifetimes, it appears that another regimes starts at that point for all three cell types, *licell*, *radcell*, and *eccell*. This regime starts with lifetimes of 80 min and 90 min and finally passes into scatter due to an obvious lack of statistical relevance. This second regime could be built by other, more persistent types of thunderstorm organization, such as multi-cells and supercells. Further investigations are needed, to verify this conclusions.

In the following studies the life-cycle characteristics of cells recorded by the ec-TRAM algorithm are investigated in more detail. Additionally to the investigations about the total set of cell tracks derived by the ec-TRAM algorithms, the lifetime frequency distribution of cells, which are tracked by the algorithm ec-TRAM but which consist only of *licells* or *radcells* throughout their whole lifetime, were performed. The resulting lifetime frequency distributions are presented in figure 4.8d and figure 4.8e, respectively. In the case of pure *licell* tracks, obviously only very short-lived cells with lifetimes less than 20 min cannot at all be related to time-coincident *radcells*. Whereas pure *radcell* tracks are found with lifetimes up to 70 min. Considering the distribution function shown in figure 4.8a, this shows that all cell tracks recorded by the tracking algorithm li-TRAM with lifetimes longer than 15 min can be related to cells recorded by the tracking algorithm rad-TRAM. Regarding cell tracks recorded by the rad-TRAM algorithm, obviously a larger part of *radcell* tracks with lifetimes up to 70 min cannot be attributed to time-coincident *licells*. From this finding it is concluded, that the majority of lightning-cell tracks which last for 20 min or longer goes along with intense ground precipitation, whereas a large part of intense precipitation cells with durations up to 70 min exist without exhibiting a single discharge throughout their whole lifetime.

For the following studies the minimum duration of *eccell* life-cycles is again set to 35 min. Here, the term *licell* is used, if the *eccell* consists of only one *licell*, the term *radcell* is used, if the *eccell* consists of only one *radcell*, and the term *eccell* is used, if the cell entry consists of both cell types. Table 4.3, 4.4, and 4.5 summarize the results.

It is found that for 4427 *eccell* entries, which belong to 305 life-cycles recorded by the algorithm ec-TRAM, 52 % of the single entries (not the life-cycles) consist of *eccells*, 46 % of pure *radcells* and 2 % of pure *licells* (see table 4.3). The large fraction of pure *radcells* can be explained by the rather low detection threshold of 33 dBZ, which detects precipitation cells well before convective rain. The occurrence of pure *licells* might be explained by outliers, which could not be attributed to the main discharge region. The

Table 4.3: Percentage of cell types for *eccell* life-cycles with lifetimes of 35 min and longer for a total 305 life-cycles with 4427 entries. Here, the term *licell* refers to *eccells*, which consists of only one *licell*, the term *radcell* refers to *eccell*, which consist of only one *radcell*, and the term *eccell* refers to *eccells* which consist of both cell types.

| cell type | <i>eccell</i> | pure <i>radcell</i> | pure <i>licell</i> |
|------------|---------------|---------------------|--------------------|
| percentage | 52 % | 46 % | 2 % |

Table 4.4: Percentage of the first cell type change, recorded after the cell develops, calculated for *eccell* life-cycles with lifetimes of 35 min and longer with a total set of 383 life-cycles. The terminology follows table 4.3.

| birth cell type | <i>eccell</i> | | <i>radcell</i> | | <i>licell</i> | |
|---------------------|----------------|---------------|----------------|---------------|---------------|----------------|
| change to cell type | <i>radcell</i> | <i>licell</i> | <i>eccell</i> | <i>licell</i> | <i>eccell</i> | <i>radcell</i> |
| percentage | 20 % | 4 % | 72 % | 0 % | 5 % | 0 % |

Table 4.5: Percentage of the last cell type change, recorded before the cell dissipates, calculated for *eccell* life-cycles with lifetimes of 35 min and longer with a total set of 392 life-cycles. The terminology follows table 4.3.

| dissipation cell type | <i>eccell</i> | | <i>radcell</i> | | <i>licell</i> | |
|-----------------------|----------------|---------------|----------------|---------------|---------------|----------------|
| change from cell type | <i>radcell</i> | <i>licell</i> | <i>eccell</i> | <i>licell</i> | <i>eccell</i> | <i>radcell</i> |
| percentage | 17 % | 3 % | 68 % | 0 % | 12 % | 0 % |

very short lifetimes found for pure *licell* tracks, discussed with figure 4.8d, confirm this statement.

Investigating the character of cell type changes within cell-tracks, it is found that of 383 cell tracks, 24 % start as an *eccell*, where 20 % change later to a pure *radcell* and 4 % change later to a pure *licell*. 72 % of the 383 cell tracks start as a pure *radcell* and change later to an *eccell* and only 4 % start as pure *licell* and change later to an *eccell* (see table 4.4). Regarding the last cell type change before the cell dissipates, it is found that in 392 cell tracks, 20 % end as an *eccell*. Here, 17 % change from a pure *radcell* to an *eccell* and 3 % change from a pure *licell* to an *eccell*. 68 % of the 392 cell tracks change from an *eccell* to a *radcell* before they dissipate, and 12 % change from an *eccell* to a pure *licell* (see table 4.5). This study illustrates, that the vast majority (about 70 %) of considerably long life-cycles, recorded with the ec-TRAM approach, start with intense ground precipitation and end with intense ground precipitation. A smaller fraction (about 20 %) start and end simultaneously with discharge activity and strong precipitation, and a minor part start and end with discharge activity. These are important results which contribute significantly to the general picture of the conceptual model.

Chapter 5

Evaluation of Convective Life-Cycles from Thunderstorm Cell Tracker ec-TRAM

In the following chapter, the information content of the new approach of data fusion, provided by the tracking algorithm ec-TRAM, is illustrated in life-cycle diagrams, showing the temporal evolution of selected cell parameters from two example thunderstorms (see section 5.1). By complementing the time-diagrams with information about the three-dimensional storm structure, derived from radar data and satellite data, it is demonstrated, that the cell parameter evolution recorded by the ec-TRAM algorithm can be interpreted in terms of underlying physical processes. But compared with the conceptual model, introduced in section 2.2, the authentic life-cycle diagrams reveal a much more complex behaviour.

Despite the complex evolution the cell parameters reveal in single storm cases, general strong correlations are found in investigations, where every cell record is considered individually and not in context of its cell history. Strong positive correlations between discharge activity, discharge height, and lightning cell area are found in statistical analyses over the total thunderstorm data set (see section 5.2.1). Two regimes can clearly be distinguished in the correlation diagrams and fit functions are given for each correlation graph and both regimes. The first regime is characterized by more compact, well-defined lightning cells with cell areas of less than 160 km^2 and a discharge activity of less than 30 counts per cell. A final explanation requires further investigations, but it is assumed that this regime includes 'simply structured' cells, which consist of a well-outlined cell core with a well-defined electrically active region. The second regime, characterized by less compact, larger and not so well-outlined areas with more intensive discharge characteristics, is supposed to consist of cells with more complex cell structures. Those cell structures might include several electrically active cell cores and/or an attached trailing-stratiform regions, like mesoscale convective systems and other multi-cell complexes. Regarding the two regimes identified in the lifetime frequency distribution (see discussion to figure 4.8 on page 4.4) and the two regimes identified in the correlation diagrams, it seems likely that the two correlation regimes and the two lifetime regimes

reflect the same thunderstorm feature. They might stem from the different types of storm organizations, single cells on the one hand and multi- and supercells on the other hand (see section 2.2.2). This would be a highly important result, which could link storm intensity with storm persistence and might open new possibilities for thunderstorm nowcasting. Therefore this matter is discussed in detail in section 5.2 and further investigations are suggested in chapter 6.

Finally it is investigated, if the occurrence of in-cloud activity is a useful warning parameter in the ec-TRAM approach. It is found that the majority of lightning-cell life-cycles start with *licells* which consist of IC events as well as CG events (see section 5.2.2). Despite the low temporal resolution of 5 min of this study, which is induced by the ec-TRAM approach, the time-lag distribution is clearly skewed to positive values, which indicates that more lightning-cells start with cell entries, which comprise only IC events, than with cell entries, which comprise only CG events. However, it turns out that in this approach preceding in-cloud activity is no reliable warning parameter for subsequent CG flashes.

5.1 Case-studies

The temporal evolution of two thunderstorms is selected for a detailed analysis. Both storms were chosen, because they had long and comprehensive life-cycles with well distinguishable cell stages and pronounced discharge characteristics and, furthermore, they were well tracked by POLDIRAD. An overview of selected storm-cell parameters is given in table 5.1. Both storms do not represent the statistical average, discussed in section 4.4. They are larger, more persistent, and exhibit more intensive lightning activity than the average storm. But they are good examples to learn about cell parameter evolutions and correlations in different storm development stages.

Time-series of selected cell parameters, which are recorded by the ec-TRAM algorithm, are complemented by three-dimensional polarimetric radar data (see section 3.2.3) and satellite data based cell information provided by the cell tracker Cb-TRAM (see section 3.2.4). They are illustrated in figure 5.1. The so called precipitation intensity is introduced to assess the precipitation extent per area and time of a cell. It is calculated for *licells* and for *radcells* separately as the total precipitation from a cell divided by the

Table 5.1: Selected cell parameters for the thunderstorm case-studies from 25 June 2008 and 22 August 2008 computed by the ec-TRAM algorithm. All values are given per cell, which means for 3 min data accumulation in the case of *licell* parameters.

| date | lifetime | <i>licell</i> | <i>radcell</i> | <i>eccell</i> | TL | IC height | IC height |
|----------|----------------------|---------------------|---------------------|---------------------|-----|-----------|-----------|
| | | | | | | mean area | mean |
| 20080625 | 145 min | 330 km ² | 290 km ² | 400 km ² | 108 | 10 km | 9 km |
| 20080822 | 380 min (205 min) | 275 km ² | 315 km ² | 390 km ² | 84 | 9 km | 9 km |

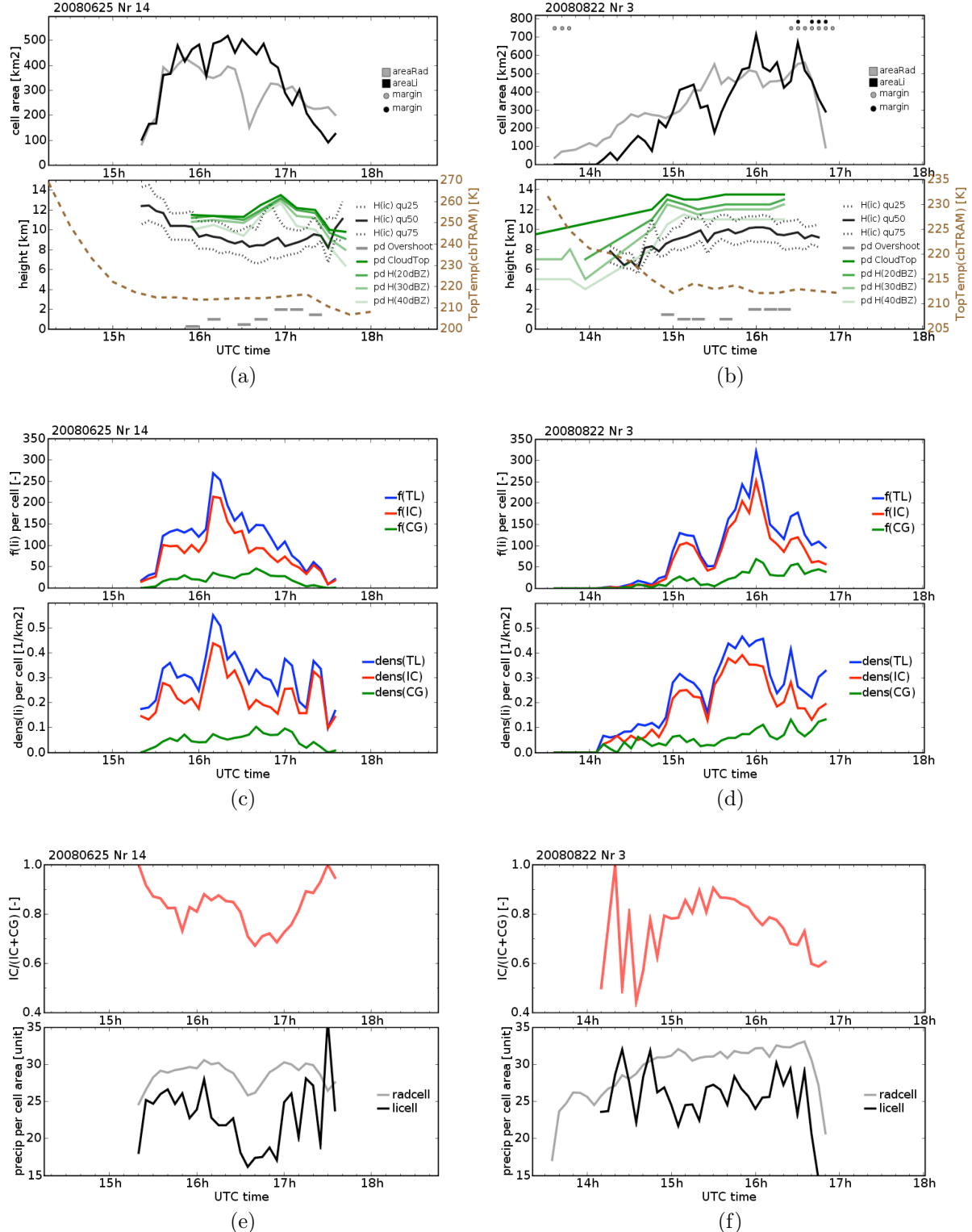


Figure 5.1: Lifetime-diagrams of selected parameters for thunderstorm case-studies from 20080625 to 20080822.

cell area. The precipitation amount is calculated by a formula, which was derived to estimate thunderstorm rainfall on the base of radar reflectivity (Jones, 1956). Because of the well-known uncertainties of this method, the precipitation intensity is only interpreted in qualitative terms and not taken as reliable quantitative measure.

The first case-study is a supercell, which propagated in easterly direction south of Munich on 25 June 2008. The whole life-cycle lasted over 150 min and was completely recorded by the ec-TRAM algorithm. The second case-study is another supercell which traversed the same domain in north-easterly direction on 22 August 2008. For this cell the first development stage was assessed by POLDIRAD and by LINET. The onset of electrical activity was also recorded by ec-TRAM. The storm was monitored for 205 min till into its mature stage before it left the domain. Both examples seem to experience a cell splitting. One cell splitting is clearly observed in the radar cell track, the other one suggested by the lightning data.

Case-study of 25 June 2008

The 25 June 2008 case is characterized by several heavy thunderstorms. The thunderstorm activity starts in south Germany in the mid-afternoon. The DWD surface analysis and the Munich sounding indicate that a prevailing zonal flow moves over a warm surface airmass, which induces high *Convective Available Potential Energy* (CAPE) values of about 1000 J/kg. Strong, unidirectional 0 – 6 km bulk shear winds of more than 20 m/s favors the development of well organized storms. The skew T-log p diagram of the Munich sounding at 12 UTC and a map illustrating the accumulated lightning activity for that day are presented in figure 5.2.

The left side of figure 5.1 shows the life-cycle diagrams of the example storm. The first reflectivity core with a maximum reflectivity of 33 dBZ is detected at 15:04 UTC in the volumetric radar scan at 4 km height (not shown in the time-diagrams). It is possible that the cell has been triggered by the outflow boundary of an older cell with which it merges around 15:40 UTC. The cell merging is reflected in a sudden increase of all extensive cell parameters and, interestingly, in discharge density, too. The next volumetric radar scan at 15:15 UTC shows a maximum reflectivity of 50 dBZ at 5 km above ground (not shown in the time-diagrams). 5 min later, at 15:20 UTC, the cell appears for the first time in the ec-TRAM data as the radar reflectivity field at the ground exceeds the threshold of 33 dBZ and lightning activity starts coincidentally. Graupel and hail are detected in the mixed-phase layer at 4 km height five minutes prior to the first electrical discharge. The electrical activity of the storm starts with IC events during an enhanced cell growth. The first CG event is recorded 5 min after the first IC event. The ratio of IC to CG discharge activity ranges widely between 2 and 40 during the whole life-cycle. At 15:25 UTC hail is observed near the ground. At 16:30 UTC a cell splitting is observed in the ground precipitation patterns and the volumetric radar data. 15 min prior to the cell splitting TL discharge frequency and density increase significantly by a factor of two, mostly due to an enhanced IC discharge activity. After the cell splitting the main electrical activity shifts to the right moving cell and then di-

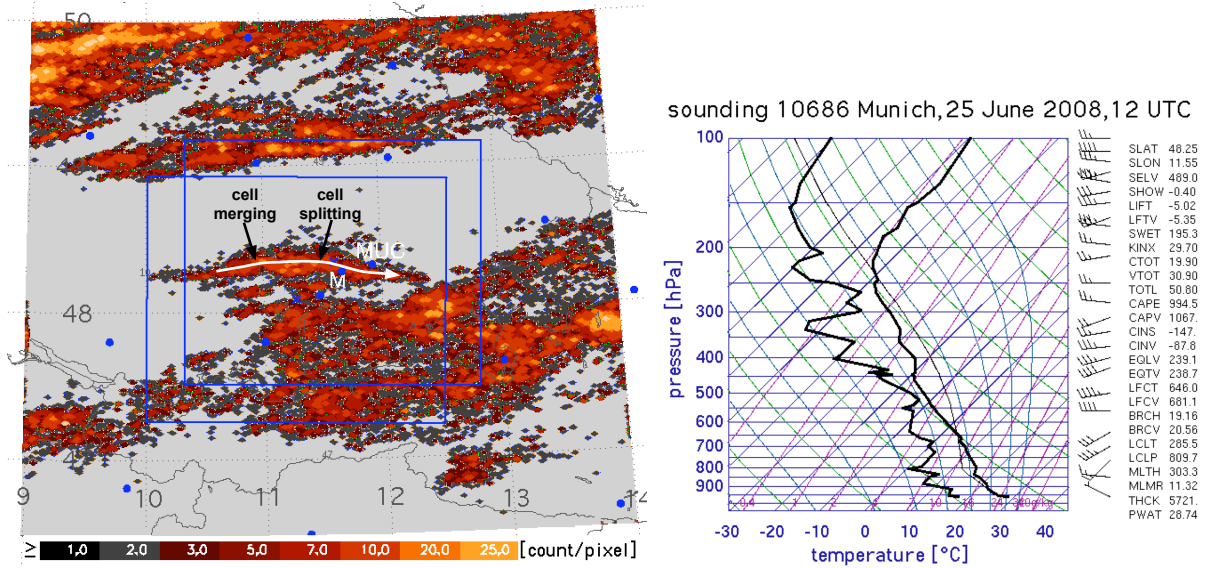


Figure 5.2: Example day 25 June 2008. Left: li-TRAM map with maximum lightning frequency per pixel for 3 min data accumulation. Right: skew T-log p diagram of Munich sounding at 12:00 UTC.

minishes while the precipitation intensity of the radar cell increases again until it reaches earlier values. At 16:35 UTC the hail at the ground changes to heavy rain. Lightning activity finally stops after 140 min. The radar cell persists until it merges at 16:45 UTC.

The synoptic condition with high CAPE and low directional but high absolute wind shear is considered supportive to cell splitting processes (Klemp, 1987). According to theory the increase of discharge frequency, which is observed just before the cell splits, might be due to an updraft intensification. The time-coincident increase of the IC fraction supports this theory. As the cell splits, the downdraft is supposed to increase. But a significant intensification in precipitation intensity at the ground is neither observed in the precipitation intensity referred to *licell* outlines nor in that referred to *radcell* outlines. The CG fraction increases after the cell splitting, which might be due to a ceasing updraft as the cell dissipates. Only just before the cell dissipates, the IC fraction increases again correlated to the final increase in electrical discharge cell density.

After the cell splitting, when the storm already decays, two significant peaks in TL and IC discharge density are observed at 17:00 UTC and 17:20 UTC. The peaks are not significant in discharge frequency. But at the same time a new development of an overshooting top as well as a spontaneous increasing in iso-reflectivity heights is observed in the vertical reflectivity patterns, shown as grey and green lines in figure 5.1a. It seems that, at the times of discharge intensification, the storm experiences short vertical cell growth, while the cloud size continuously shrinks. Figure 5.3 compares the storm cross sections right after the storm splitting and during a phase of later updraft intensification. They show the different structures. The first one has a high reflectivity core with a broad precipitation area and lightning incidents are widely spread. The other one has

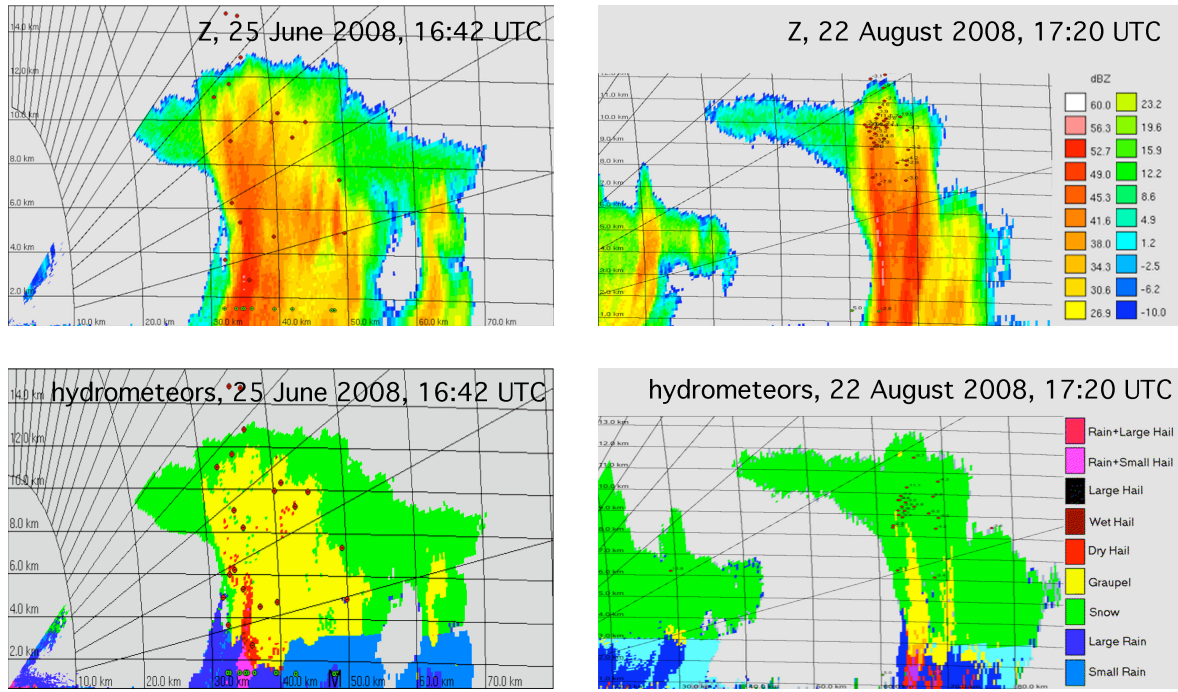


Figure 5.3: POLDIRAD RHI scans from the example storm from 25 June 2008 right after cell splitting at 16:42 UTC and at the time of updraft intensification at 17:20 UTC. Upper graphs show reflectivity maps. Lower graphs show the respective hydrometeor classification after Höller et al. (1994).

a high reaching reflectivity core and a significant overshooting top but a narrow storm structure and lightning events occur compact.

The mean discharge heights, shown in figure 5.1a reveal the exact opposite behaviour as it would be expected by the actual stage of knowledge (Demetriades et al., 2004). While the cell grows, the mean discharge height decreases, whereas it increases when the cell dissipates. It has been found in previous studies, that two discharge regions exist at different heights in the thunderstorm updraft (Proctor, 1991; Lund et al., 2009). It is possible, that in the final stage, as the lower cloud part decays, the discharge activity shifts to the upper discharge region in the cloud. But still the discrepancy, found in the development stage, cannot be interpreted in terms of physical understanding. But it can probably be explained by local sensitivity variations in IC and CG detection (see section 3.1.3), since the cell path enters a region of possible low IC detection efficiency.

The Cb-TRAM algorithm records the cell as 'rapid developing' for the first time at 14:35 UTC. At 15:15 UTC the Cb-TRAM algorithm classifies the cell stage as 'mature thunderstorm', right in accordance with the onset of lightning activity (note that lightning data are not used in the Cb-TRAM algorithm). The dashed, brown line in figure 5.1c illustrates the temporal evolution of cloud top temperature as recorded by the Cb-TRAM routine. A temperature decrease from 270 K to 215 K precedes the onset

of lightning and rain by 1 h. After that, the temperature remains stable during the rest of the cell lifetime, until the Cb-TRAM cell merges with another cell at 17:30 UTC. The cell merging can be seen in a new temperature drop.

Case-study of 22 August 2008

On 22 August 2008 a high-level trough connected with a low-level cold front approached south Germany from the north-west, inducing strong south-westerly flow. Moderate CAPE values of about 500 J/kg and strong unidirectional 0 – 6 km bulk wind shear up to 30 m/s support the development of two well organized thunderstorms, which propagate through the south of Germany in north-easterly direction. Beside the two vigorous storms, some weak and short-lived cells are recorded in the area. To give an overview of the thunderstorm day, the skew T-log p diagram of the respective Munich sounding at 12 UTC and a map, which illustrates the accumulated lightning activity of that day, are presented in figure 5.4. The respective storm time-series are presented on the right side of figure 5.1. The example storm is not completely assessed by the ec-TRAM algorithm. Marked as grey and black points in figure 5.1b are those record times when the storm cell is cut by the domain margin to indicate that respective cell parameters are not reliable.

The DLR radar POLDIRAD monitors the development of a prefrontal precipitation line in the outlines of the alps (Lech valley) around 13:00 UTC, which propagates in north-eastern direction toward Munich. The southernmost cell develops to a persistent cell, whereas the other cells either have merged with the major cell or dissipated by the time the system enters the ec-TRAM domain. At 13:40 UTC the ec-TRAM routine monitors the storm system for the first time as a single *radcell* with peak reflectivity values around 50 dBZ. The first signs of graupel and hail appear at 14:05 UTC in an altitude of 4 km above ground, the first two isolated lightning events, an IC and a CG discharge, are recorded at 14:15 UTC. Low, fluctuating discharge frequencies up to 5 events per cell are recorded until 14:45 UTC. At 14:45 UTC finally significant discharge activity starts, which is reflected in discharge frequency and discharge density patterns of figure 5.1d. First hail at the ground is recorded at 14:26 UTC in the POLDIRAD scan. The temporal evolution of radar iso-reflectivity heights, illustrated as green lines in figure 5.1b, indicate a cell growth right from the beginning of the cell record which results in an overshooting cloud top. The overshooting is well in coincidence with the onset of significant electrical activity. After the extensive cell growth the iso-reflectivity heights remain almost constant until the cell leaves the domain. The mean IC discharge height per cell, also shown in figure 5.1d, reveals similar patterns. The temporal evolution of the mean height can be interpreted here, unlike the example from 25 June 2008. Neglecting the first scattered discharge activity, the mean height increases steeply from 7 km to almost 10 km as the just developing storm undergoes an extensive cell growth. It approaches its maximum height in the mature stage of the thunderstorm, and then decreases slightly again until the cell leaves the domain. The overshooting top, deduced from POLDIRAD cross section scans, correlate well with lightning activity. POLDIRAD data might have helped to explain the break observed in several cell parameters around

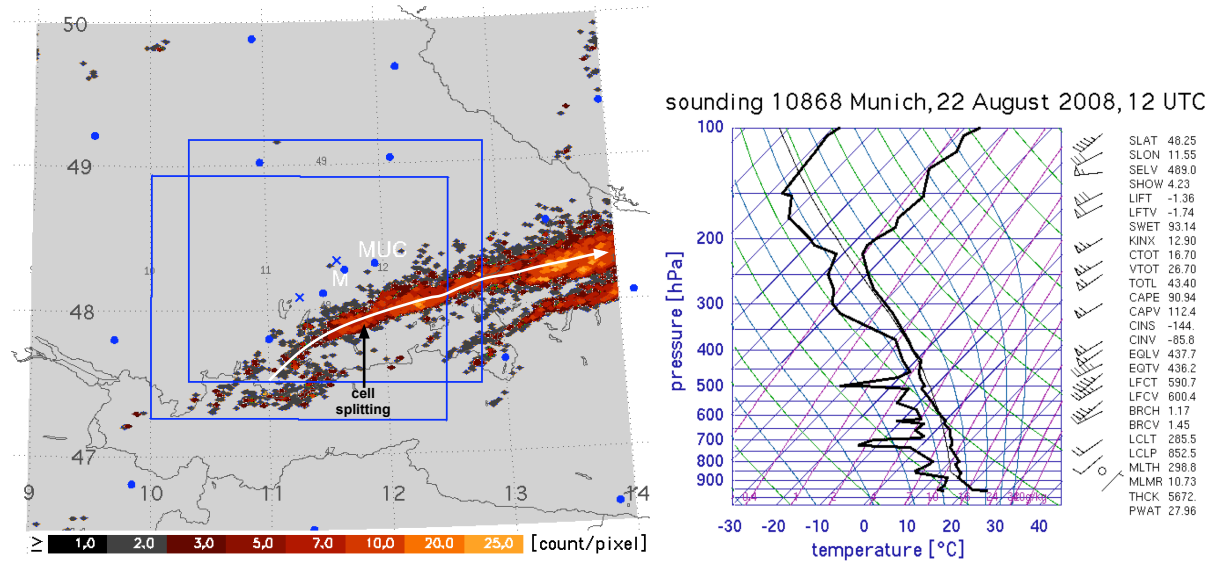


Figure 5.4: Example day 22 August 2008. Left: li-TRAM map with maximum lightning frequency per pixel for 3 min data accumulation. Right: skew T-log p diagram of Munich sounding at 12:00 UTC.

15:30 UTC, but there exist no data at that time. The time sequence of ec-TRAM maps (not shown) illustrates, that the respective *licell* starts to grow at 15:15 UTC with discharges evenly spread over the cell area. At 14:40 UTC the cell suddenly becomes very compact. At the same time and for the next 10 min a bend to the right is observed in the *licell* track. By the time the cell develops more vigorous electrical activity, it follows again the undisturbed *radcell* track. It can be seen in figure 5.1d, that the jump appears as a sudden drop and a steep recovering observed in *licell* area, discharge frequency, and discharge density. The jump appears also in the cell mean IC discharge height and goes along with a ceasing overshooting top, as it can be seen in figure 5.1b. Comparing these patterns with the case-study from 25 June 2008 a cell splitting seems likely. The cell leaves the domain at 16:24 UTC.

In comparison with the previous example, the *licell* area of this cell reveals in general a more unsteady behaviour. But the jumps in *licell* area correlate well with discharge frequency and cloud top overshooting, and therefore seem reliable. If the scatter before the onset of significant discharge activity is neglected, the IC to CG relation, presented in figure 5.1f, reveals a similar behaviour as the other example cell, which further supports the assumption of a cell splitting. The IC fraction increases during the growing phase while the CG fraction increases after the time, when cell splitting is assumed to occur. The different time delays between the break observed in the cell parameters and in the IC to CG fraction, in the two case-studies might be explained by the observation, that the cell splitting starts in the upper cell core. Therefore, it would be expected to appear first in the elevated lightning patterns and later in the precipitation pattern at ground. Again the precipitation intensity, calculated for the *radcell* outlines, increases as the cell develops until it leaves the research domain. The precipitation intensity,

calculated for the *licell* outlines, fluctuates strongly. Just like in the case-study from 25 June 2008, an increasing fraction of CG events is observed at later cell stages. The final storm stage has not been assessed, since the cell leaves the domain, which prohibits further interpretation.

The temporal evolution of the cloud top temperature, derived from the corresponding Cb-TRAM cell, shows a steep decrease 30 min prior to the first discharge event. Then the temperature decreases less steep as the first isolated discharges are recorded and stabilizes, when significant discharge activity starts. Like in the previous example the Cb-TRAM algorithm catches the convective initiation. It classifies the cell as 'rapid developing' for the first time at 13:30 UTC. At 14:15, 10 min prior to the first isolated electrical discharges and 35 min before significant lightning activity starts, the cell stage changes to 'mature cell' .

Both example storms reflect the hypothetical life-cycle pattern, discussed in section 2.2, quite well. In both storms extensive vertical cell growth and hail and graupel occurrence in the mixed-phase layer of the cloud precede the onset of significant lightning activity by 5 to 10 minutes. A general correlation between cell growth and lightning activity is found together with an increase of the IC fraction in TL activity. Although an interruption, which is attributed to a cell splitting, is reflected in both lifetime-diagrams, the rain intensity per radar cell shows the general tendency to increase as the cell ages, while a general increase in the CG fraction of TL activity is observed at the same time. This suggests a correlation between convective precipitation intensity and hail occurrence at the ground and CG flash rates as it could be expected by theory (Rutledge and MacGorman, 1988; Carey and Rutledge, 1996; Lopez and Aubagnac, 1997). A clear correlation between IC mean discharge height per cell and cell stage can be identified for the 22 August 2008 case. This correlation is in agreement with previous studies (Demetriades et al., 2004). Lightning network configuration effects seem to play a role for the correlation between IC mean discharge height per cell and cell stage for the case-study from 25 June 2008. The satellite data-based algorithm Cb-TRAM assesses the convective initiation of the thunderstorm approximately 30 min prior to the first electrical discharges. But the algorithm does not provide information about cell evolution once the cloud top has reached the tropopause.

5.2 Statistical Results

5.2.1 Lightning-Cell Parameter Correlations

The principal existence of selected cell parameter correlations, which are suggested by the case-studies in the previous section, were further investigated in statistical analyses and discussed now. The calculations are performed based on the total thunderstorm data set. For the following studies every cell entry is used discrete and not in context with its life-cycle. Cells, which are not totally recorded in the domain but cut by the margin, are neglected. The results are plotted in correlation graphs. Graphs, prepared to visualize the parameter correlation functions, are presented in figure 5.5. They show

the mean values of finely resolved accumulation steps. The corresponding fit functions are listed in table 5.3. To illustrate the distribution scatter around the correlation means, box-and-whisker plots were computed for a coarser resolution and presented on linear axes in figure A.3 and figure A.5 in the appendix. The underlying count statistics are given also given in the appendix A.5 in figure A.6 and figure A.6. Once more it is pointed out, that all cell parameters refer to cell objects as identified by the algorithm li-TRAM (see section 3.1.3). The term 'per cell' indicates, that lightning data are still accumulated for 3 min and not normalized to any time unit. It is specially mentioned, if the discharge frequency is normalized to 1 min.

The graphs, presented in figure 5.5, illustrate the correlation statistics between *licell* area and discharge counts per *licell* (figure 5.5a), *licell* area and discharge density per *licell* (figure 5.5b), *licell* area and cell mean discharge height of IC events (figure 5.5c), and discharge counts per *licell* and IC cell mean discharge height (figure 5.5d). If reasonable, TL and IC discharge activities were investigated separately.

A break in the correlation functions, which apparently separates two cell regimes, is clearly visible in all four correlation graphs shown in figure 5.5. The cell parameters, which define the transition point, are listed in table 5.2. The break point corresponds consistently in all correlation diagrams to a *licell* area of about 160 km^2 (figure 5.5a, figure 5.5b, and figure 5.5c) and the corresponding discharge activity of about 20 (IC events) and 30 (CG events) counts per cell (figure 5.5a). The dependence of the cell area on the discharge activity can be seen in the linear correlation graphs, presented in the appendix A.5 in figure A.3a and figure A.3b. The appearance of the correlation function changes abruptly from one regime to the other. At the transition to higher cell-parameter values the inclination of the correlation functions decrease and the mean values abruptly start with significant scatter.

The correlation graphs will be discussed separately and in detail first and interpreted all together afterwards. The strictly monotonic increasing correlation found between the *licell* area and the mean TL discharge count per *licell*, presented in figure 5.5a (and figure A.3a), follows an exponential function until the area reaches about 160 km^2 which correlates with approximately 30 TL counts per *licell*. At this point the exponential correlation curve breaks. After that, the correlation means increase less steep and reveal more extensive scattering. The correlation between *licell* area and mean IC discharge count, presented in figure 5.5a (and figure A.3b), reveals similar pattern but at lower discharge activities and with steeper inclinations. The transition point is found at a *licell* area of 160 km^2 which corresponds with a IC discharge activity of about 20 counts per *licell*.

The correlation means between *licell* area and TL discharge density per *licell*, illustrated in figure 5.5b (and figure A.3c), can be directly deduced from the correlation between *licell* area and *licell* discharge counts per *licell*. It can be seen, that the correlation function starts at a comparably high cell discharge density and decreases first steeply until it reaches a minimum value at a cell area of about 70 km^2 . Then the correlation curve increases again, but less steeply than it decreases before the minimum.

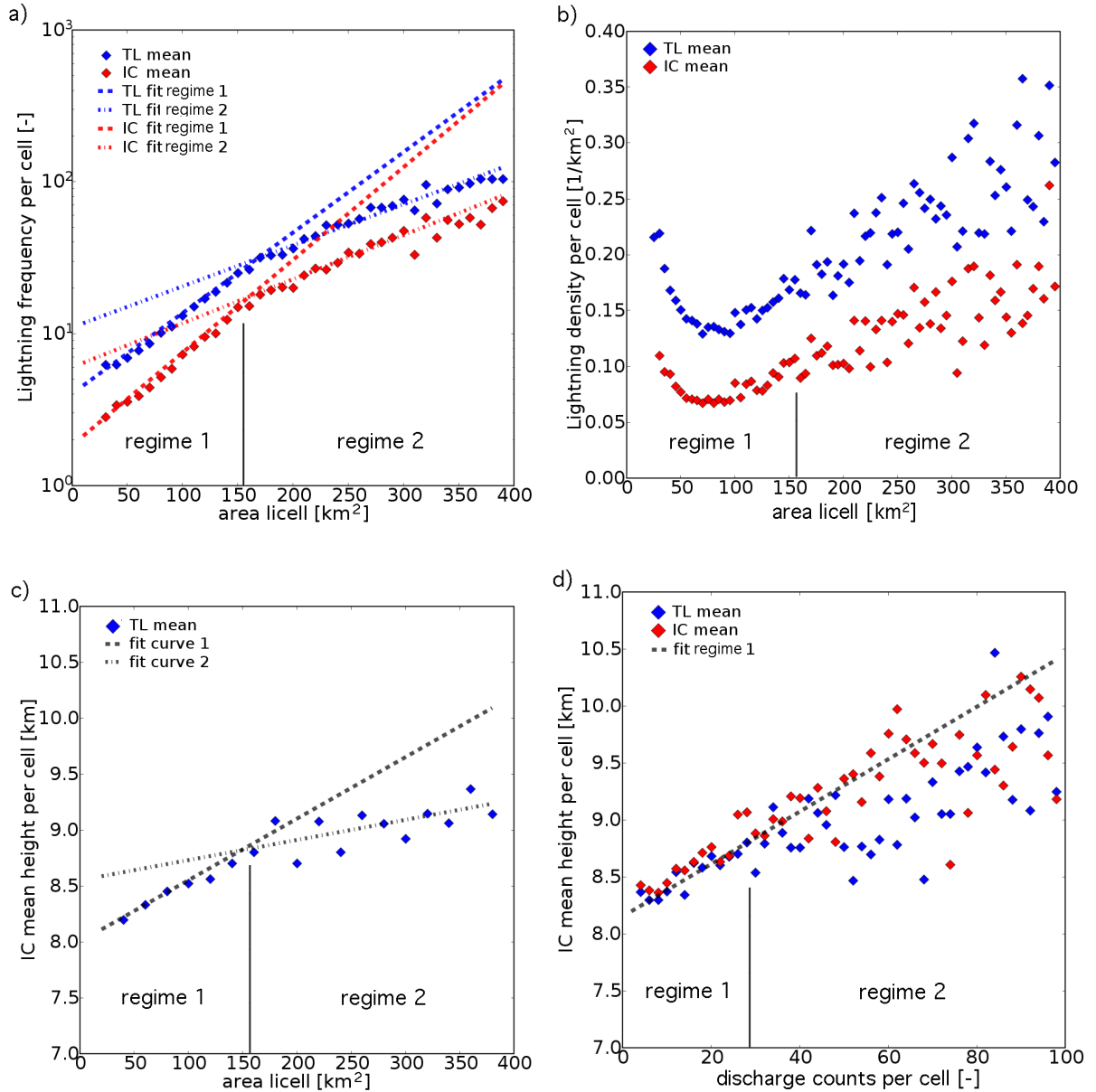


Figure 5.5: Correlation plots with fit functions for (a) TL and IC discharge frequencies per *licell* versus *licell* area, (b) TL and IC discharge density per *licell* versus *licell* area, (c) IC mean discharge height per *licell* versus *licell* area, and (d) IC mean discharge height per *licell* versus TL and IC discharge frequencies for total data set recorded during summer 2008.

The break around 160 km^2 can be seen in the sudden onset of scatter. Similar pattern at lower discharge density values are found in the correlation graph between *licell* area and mean IC discharge density per *licell*, as illustrated in figure 5.5b (and figure A.3d). In this correlation, too, the minimum discharge density is found at a corresponding cell area of approximately 70 km^2 and the scatter of the mean values increases abruptly for

Table 5.2: Characteristic *licell* parameters, which mark the transition point from cell regime 1 to cell regime 2 computed per *licell*, which comprises 3 min lightning data (first line) and per *licell* object normalized to 1 min discharge frequency (second line).

| cell area | TL frequency | IC frequency | IC mean discharge height |
|---------------------|--------------|--------------|--------------------------|
| 160 km ² | 30 | 20 | 9 km |
| 160 km ² | 10 1/min | 7 1/min | 9 km |

cell areas larger than 160 km².

The strictly monotonic increasing correlation, found between *licell* area and IC mean discharge height, illustrated in figure 5.5c (and figure A.3e), follows closely a linear relationship until a cell area of 160 km² and a discharge height just below 9 km. After that the inclination decreases and significant higher scattering starts abruptly.

Another strictly monotonic increasing correlation is found between TL discharge count and the IC mean discharge height per *licell*. The respective graphs are presented in figure 5.5d (and figure A.5a). It can be seen in figure 5.5d that this correlation generally exhibit more scatter than the previously discussed parameter correlations. But still, a break point in the correlation line can be identified at around 20 to 30 counts per *licell* with a corresponding IC mean discharge height just below 9 km. At this point the correlation means leave the linear fit function and start a more significant scatter. The correlation between IC discharge activity and the IC mean discharge height per *licell* shows the same characteristics, only that the mean height is slightly drawn to higher values. This result indicates, that the higher the mean discharge height of IC activity, the higher is generally the discharge frequency and the higher is the IC fraction in TL activity. In an attempt to correlate this finding with the updraft strength (or more correct with the charge separation efficiency) the line of arguments is, the more vehement the updraft, the higher is the general discharge activity and the higher is the IC fraction in TL activity on the one side, and the more vehement the updraft, the higher is the electrically active core and therewith the mean discharge height on the other side.

In both correlation characteristics, discussed for IC mean discharge heights, the mean height seems to approach asymptotically an upper limit. This can be explained by the existence of the natural upper border at the tropopause.

Table 5.3: List of fit functions retrieved from correlation diagrams of figure 5.5. Fit functions are given per *licell*, which comprises 3 min lightning data, and per *licell* normalized to 1 min discharge activity (in parentheses).

| | y-value | x-value | fit function | |
|----------|---|---------------------------------|---|-------------|
| regime 1 | area <i>licell</i> / [km ²] | TL discharge count per cell | $y = 4.03 \cdot 10^{0.0053x}$ ($y = 1.34 \cdot 10^{0.0053x}$) | figure 5.5a |
| | area <i>licell</i> / [km ²] | IC discharge count per cell | $y = 1.84 \cdot 10^{0.0061x}$ ($y = 0.61 \cdot 10^{0.0061x}$) | figure 5.5a |
| | area <i>licell</i> | IC mean discharge height / [km] | $y = 0.0055x + 8.00$ | figure 5.5c |
| | TL and IC discharge count per cell | IC mean discharge height / [km] | $y = 0.023x + 8.15$ ($y = 0.069x + 8.15$) | figure 5.5d |
| regime 2 | area <i>licell</i> / [km ²] | TL discharge count per cell | $y = 11.00 \cdot 10^{0.0027x}$ ($y = 3.67 \cdot 10^{0.0053x}$) | figure 5.5a |
| | area <i>licell</i> / [km ²] | IC discharge count per cell | $y = 6.0 \cdot 10^{0.0029x}$ ($y = 2.0 \cdot 10^{0.0061x}$) | figure 5.5a |
| | area <i>licell</i> / [km ²] | IC mean discharge height / [km] | $y = 0.0018x + 8.55$ | figure 5.5c |
| | TL and IC discharge count per cell | IC mean discharge height / [km] | no fit | figure 5.5d |

Regarding the underlying count statistics, presented in figure A.6, it can be excluded that the existence of a break point in the correlation graphs is only due to poor statistics.

For now, a possible explanation of the two cell regimes can only be suggested. Since the cell area and the corresponding discharge activity at the transition point are higher than the seasonal mean values (compare graphs in figure 5.5, figure 4.6, and figure 4.7), it is suggested that the two regimes belong to different thunderstorm organizations. The first regime would include the most frequent type of thunderstorm organization - single cells - which are rather simple structured, with a well-defined updraft and a well-outlined electrical active core. During the development stage, the IC discharge height increases in correlation with increasing storm size (storm height and storm area). The cell area and the discharge activity increase further, when a downdraft develops, because lightning spreads into the downdraft region. But the discharge density decreases, because the main driving processes for charge separation in the cloud are still restricted to the updraft region, while the downdraft region does not contribute to the process. So the efficiency of the driving processes, which lead to lightning discharges, does not increase to the same degree, as the cell area does, which results in a decreasing discharge density per cell. During the dissipation stage, the discharge activity decreases again, together with a decreasing cell area and a decreasing IC mean discharge height. The second regime could include less frequent, more complex thunderstorms, like mesoscale convective systems or other multi-cell systems, which are generally larger and exhibit higher discharge activities than single cells. Those cells might experience the same development phase as the cells of regime one. But then they develop a more complex and more consistent mature phase, with two or more coexisting active cores. The less well-defined cell outlines would then explain the sudden onset of scatter in the correlation graphs. The scatter might also be induced, or emphasized, when lightning activity spreads into attached stratiform regions (Carey et al., 2005). The mean discharge height of IC events would increase with cell size due to generally more effective updrafts in the self-sustaining systems. Due to the natural border at the tropopause, an upper boundary still exists, which flattens the correlation function.

Since both cell regimes cannot only be identified in cell parameters, which are dependent of the cell definition, but also in a cell parameter, which is totally independent of the cell definition, namely the IC discharge height, a procedural artefact can be excluded as a reason. The two cell regimes, found in the cell parameter correlation graphs (see figure 5.5), and the two lifetime regimes, found in the lifetime frequency distribution (see figure 4.8), might be caused by the same storm property, namely the thunderstorm organization. If this is true, storm duration and storm properties can be linked and the linkage might be useful for thunderstorm nowcasting to classify a storm and attribute nowcast-relevant storm features, like persistence, intensity, and others to the storm prediction. But clearly, further investigations are needed, to verify this interpretation. Possible approached are suggested in chapter 6.

5.2.2 Time Lagged IC and CG Discharge Activity

The usability of the onset of IC discharge activity as operational warning parameter for subsequent CG strokes in the ec-TRAM approach was tested. For this study it was tested, whether the composition of the cell object, computed by li-TRAM, consists of only IC events (pure IC lightning-cells), IC and CG events (mixed lightning-cells), or only CG (pure CG lightning-cells) events. The time difference between pure IC cells and pure CG cells was used to compute the lead time frequency diagram shown in figure 5.6. Only 'secure IC events' and 'secure CG events' were used in the calculations (see section 3.2.1). If a cell-cycle starts with TL activity, but no CG or IC event is recorded, the cell-cycle was dismissed. Only cell tracks recorded by the li-TRAM algorithm were used, which last 15 min and longer. All *licells*, which were used for the investigation, had to be completely in the domain. 1294 cell tracks could be used for this study. The lead time T_{lead} , found in a cell life-cycle, was computed as following:

If the first recorded lightning-cell entry of a life-cycle consists of only IC events, the time step to the first subsequent lightning-cell of that life-cycle, which includes also CG events, is calculated as positive lead time. If the first recorded cell entry consists of only CG events, the time step to the first subsequent lightning-cell, which includes also IC events is calculated as negative lead time. If the first recorded lightning-cell entry consists of IC as well as CG events, the lead time is set zero.

It can be seen in the lead time distribution, that the majority of the *licell* life-cycles start with both IC and CG events. But the distribution is clearly skewed to positive lead times. Neglecting the zero values 62 % of the life-cycles are found to have positive lead times with an average lead time of $+6.7\text{ min}$ and 38 % negative lead times with an average lead time of -6.4 min . The mean lead time, including zero values, is found to be 1.7 min. The study has also been performed with *licell* tracks which last 10 min or more. The resulting lead times are drawn closer to zero, but they do not differ significantly

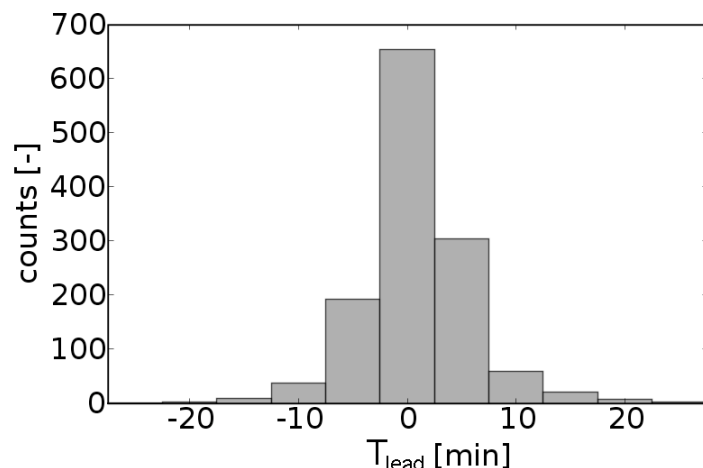


Figure 5.6: IC lead time distribution for *licell* tracks equal or longer than 15 min. 1294 cell cycles were investigated.

from the values given above. It becomes evident, that in this approach a reliable pre-warning time for CG strokes on basis of preceding IC discharge activity cannot be given.

The median lead time of zero minutes are most likely due to the coarse temporal resolution of 5 min, but the general low lead times might be reliable. Obviously, the temporal resolution, induced by the tracking approach, is not practical for detailed physical investigations. But it is still a promising result, that in spite of this rough limitation the lead time distribution is already skewed to positive lead time values. A finer temporal resolution would reveal a clearer picture of a usable prewarning time for CG strokes.

Chapter 6

Conclusion and Outlook

In this work the potential and usability of highly accurate, three-dimensionally resolved lightning data for thunderstorm tracking and very-short term prediction of storm evolution (nowcasting) has been examined. The benefit of total-lightning information for future thunderstorm nowcasting tools has been examined both separately and in combination with information derived from highly resolved two-dimensional conventional and three-dimensional polarimetric radar and satellite data. The new cell tracking algorithm ec-TRAM has been developed especially for this purpose (see section 3).

All studies are based on data, which were recorded during the summer season 2008 in southern Germany (see section 3.2.5). Total-lightning information has been provided by the novel European VLF/LF lightning detection network LINET. During the observation period the measurement strategy of the DLR radar POLDIRAD has been set to assess the three-dimensional storm evolution. The radar provides three-dimensional polarimetric information which allows for a hydrometeor classification.

This work demonstrates that independently treated total-lightning information is a highly useful data source for thunderstorm nowcasting. In the ec-TRAM approach three-dimensional information about storm structure can be combined with a two-dimensional cell tracking. Short-term variations in discharge characteristics capture the momentary storm dynamic and are useful parameters for predicting subsequent storm evolution and storm events, such as cell splitting. In combination with other commonly used data sources, e.g conventional and polarimetric radar data and satellite data, a more complete picture about the storm state and evolution is derived, which can be used to classify the storm type and assess the storm state (see section 2.2).

Ec-TRAM Set-Up and Performance

The ec-TRAM approach identifies, tracks, and monitors convective ground precipitation fields and electrically active regions of thunderstorms independently in a high temporal and spatial resolution. For each time step, the information of both cell types, lightning and precipitation cells, are combined to new cell objects by using the spatial overlaps of contemporarily identified cell contours (see section 3.1.4). The new cell objects are then tracked based on previously recorded lightning and radar-cell tracks. This approach

proved to be useful, because both cell types are closely and independently tracked. Furthermore, the combined cell information complement but do not affect each other. The cell information management is set up as a relational database, so that general cell information about the cell complexes as well as detailed information about the single cell components remain selectively accessible for later analyses.

It is found in case-studies as well as in statistical studies, that the ec-TRAM approach creates meteorologically reasonable cell objects, which are capable to assess a complex thunderstorm structure in whole as well as in its individual cell components (see section 4.1). Three-dimensional information about the structural storm evolution can be deduced from the total-lightning information. The cell tracking method employed in the ec-TRAM routine is shown to be coherent and outperforming the cell tracking based on radar or lightning data only (see section 4.2). Due to the high temporal resolution of 5 min the ec-TRAM algorithm resolves short-term storm developments and reveals a detailed picture of thunderstorm evolution.

Because of the more fluctuating lightning patterns, cell tracking based on lightning data appears more irregular in comparison to cell tracking based on more steadily evolving precipitation patterns. This putative disadvantage is found to be compensated in the tracking method of the ec-TRAM approach. All lightning-cell tracks with lifetimes of 25 min and longer can be linked to simultaneously occurring radar-cells. Thus, the tracking of electrical discharge cells becomes more comprehensive in the combined tracking approach of ec-TRAM (see section 4.4). Further comparative analyses reveal that cell tracking, based on radar data alone, misses 25 % of the lightning-cells. It cannot be concluded straight forward that a thunderstorm nowcasting based on radar data alone would have totally missed these 25 %. But it can be concluded that a significant fraction of lightning information is lost, when lightning occurrence is not identified independently and tracked separately as it is done in the ec-TRAM approach.

The limited quality values, which are found for spatial cell nowcasts of the algorithms rad-TRAM and li-TRAM, might be attributed mostly to the high spatial resolution. Due to the pixel wise comparison, which is used to compute the forecast quality parameters, POD, FAR, and CSI will underestimate the forecast quality. But the study also shows, that an improvement is most likely to be achieved for both algorithms by tuning the calculation of the displacement vector field, which is employed to extrapolate the cell positions. Still, the more appropriate approach of pure cell tracking instead of the currently employed area-tracking method is suggested to compute the cell nowcasts for lightning-cells in li-TRAM. However, the current nowcast quality has been sufficient, since the objectives of this work concentrate on cell tracking.

Ec-TRAM Evaluation

Two case-studies, recorded on 25 June 2008 and on 22 August 2008, were selected and complemented with three-dimensional polarimetric radar data and cloud top temperature profiles, derived from satellite data, to obtain a more detailed picture about storm structure, hydrometeor formation, and storm growth (see section 5.1). The principal

existence of a general conceptual scheme can be supported. Both lifetime diagrams are in good agreement with previous observations (see section 2.2). Although principal parameter evolutions are indicated by the life-cycle diagrams of the two case-studies, the cell parameters show a far more complex behaviour in detail. This is not surprising, considering the large number of case-studies, which are described in the literature. They accentuate the individuality of each thunderstorm life-cycle. The short-term fluctuations, which superimpose the long-term trends in the parameter evolutions, are found to reflect the momentary storm dynamic.

Both thunderstorms show hail and graupel formation in the mixed phase layer 5 – 10 min prior to the onset of electrical discharges. This correlation is consistent with the currently accepted theory of charge separation in thunderstorm updrafts with ice phase (Dash et al., 2001; Saunders, 2008) and has already been found in previous studies (Bringi et al., 1997; Jameson et al., 1996; Dotzek et al., 2001; Altaratz et al., 2001). Investigating the warning parameters provided by the DLR algorithm Cb-TRAM, which tracks thunderstorms based on Meteosat-8 SEVIRI data (see section 3.2.4), growing thunderstorm cells and acute warnings have already been identified prior to the first recorded lightning incidents. In case of the storm from 25 June 2008 a growing cell has been detected 45 min and an acute thunderstorm warning has been given 45 min before the first lightning incident has been recorded. In case of the storm from 22 August 2008 a growing cell has been recorded 30 min prior to the first lightning incidents and acute warnings have been given 10 min in advance.

Beginning IC discharges, instead, are found to be no reliable warning parameter for subsequent CG flashes in the ec-TRAM approach (see section 5.2.2) as it might be concluded from other studies (MacGorman et al., 2006; Demetriades et al., 2004; Bringi et al., 1997; Williams et al., 1987). A study has been performed, which considers the temporal evolution of the composition of the aggregated cell objects recorded by li-TRAM (pure IC lightning-cell, pure CG lightning-cell, mixed lightning-cell), not every single discharge event. It is found that the vast majority of lightning-cells consist of both lightning types, when they are recorded for the first time. But despite the low temporal resolution of 5 min, which is dictated in this study by the temporal resolution of ec-TRAM, the frequency distribution diagram shows the clear tendency, that electrical discharges start preferentially in the cloud. Considering only those cell tracks, which start either as pure IC cell or as pure CG cell, it is found that 62 % start as pure IC cell and 38 % as pure CG cell. The study clearly disqualifies a CG stroke warning based on preceding IC incidents for this approach. However, it is remarkable that a lightning localization method, which operates in the VLF regime, shows a preference in the lead time distribution even at this low temporal resolution.

The IC flash rate is found to correlate generally well with cell growth (see section 5.1). This finding could be consistent with the correlation found in previous studies (Williams et al., 1987; Motley et al., 1996) between graupel volume suspended in a vigorous updraft, indicating storm intensification, and IC flash rate. The temporal evolution of the mean IC discharge height reveals ambiguous patterns. In the case-study from 22 August

2008, the mean height is found to increase from an altitude of 8 km to an altitude of 10 km with cell maturity. In the dissipation phase the altitude decreases again to 9 km. This is consistent with other observations (Demetriades et al., 2004). The behaviour is also reasonable, if it is assumed, that in-cloud discharges are primarily bound to special regions in the cloud, where the potential differences are highest. The discharge height is then supposed to follow the vertical motion of those regions. In the other case-study the mean IC discharge height starts at high altitudes, sinks with cell maturity and increases again as the cell dissipates. It is possible that in this case the configuration of the lightning detection network does affect the lightning information (see section 3.2.1).

The rain intensities, found for the radar-cells, and the CG contribution to TL discharge frequency show in general a positive correlation. Both parameters increase with cell age. A positive correlation between descending small hail below the height of the negatively charged graupel region and CG flashes was already found in previous studies (Lopez and Aubagnac, 1997; MacGorman et al., 1989). It was also observed, that peaks in storm outflows lag or coincide with maxima in the CG flash rate and hail rate (Carey and Rutledge, 1996) and that the majority of negative CG events are located in the convective precipitation region (Rutledge and MacGorman, 1988). It is suggested by these observational studies and by discharge modeling (Mazur and Ruhnke, 1998; MacGorman et al., 2001) that the subsiding hail/graupel core produces the electric bias, which is needed to initiate the downward propagating channel leader of a CG flash. As a consequence of the descending hail/graupel core intensified precipitation at low levels would be expected, as observed in the case-studies.

Two lifetime regimes, separated by lifetimes between 80 and 90 min, can be identified in all three lifetime frequency distributions for cell-tracks computed by the algorithms rad-TRAM, li-TRAM, and ec-TRAM on the basis of the total cell data set (see section 4.4). The regimes most likely reflect the persistence of different thunderstorm organizations. It is suggested, that short-lived single-cells contribute to the short-lived regime and the well organized, more persistent organization forms of multi-cells and supercells contribute to the long-lived regime.

Strong correlations between selected lightning-cell parameters were found in statistical analyses over the total thunderstorm data set (see section 5.2). In this study, every cell record was investigated isolated, detached from its evolutionary history. Very strong positive correlations are found between cell area and TL as well as IC discharge activity per cell (discharge frequency and discharge density), between cell area and IC mean discharge height per cell, and between TL as well as IC discharge activity per cell (discharge frequency and discharge density) and mean IC discharge height per cell. Two cell regimes can be identified in all five correlation diagrams (figure 5.5). The two cell regimes are consistently separated in all correlation diagrams by a characteristic cell area of about 160 km^2 and the corresponding discharge frequencies between 20 and 30 counts per cell for both, TL and IC discharges. The transition between the regimes is throughout sharp. The first regime is characterized by small, compact, and well-defined cells. The second regime is characterized by larger, less compact and apparently not

so well-defined cells. For both regimes the correlation curves can be parameterized (table 5.3). While the slope of the fitting line of the correlation function changes, significant scattering starts abruptly with the second regime.

The correlation diagrams contain no time information about storm developments. So for the present, possible reasons to explain the two regimes can only be suggested. The following explanation still has to be verified. Since both, the cell area and the corresponding discharge activities at the transition point, are higher than the seasonal mean values (compare graphs of figure 5.5, 4.6, and 4.7), it is suggested that the two regimes belong to different types of thunderstorm organizations.

The first regime might include rather simply structured thunderstorms. These thunderstorms develop a well-defined updraft region, so that the lightning-cells are compact and sharply outlined. The mean IC discharge height increases in correlation with cell growth. The contemporary decreasing discharge density might be explained with the development of a downdraft. While both, the cell area and the discharge frequency further increase, because lightning might spread into the downdraft region, the efficiency of the driving processes for charge separation and lightning activation, being primarily restricted to the updraft region, does not increase to the same degree as the area. Consequently the discharge density would decrease. But the small cell areas might argue against this explanation. During the dissipation stage, the discharge frequency decreases again, together with a decreasing cell area. Since IC discharges can as well continue in the upper parts of the cloud, the mean IC discharge height does not necessarily need to decrease. The suggested features are consistent with the conceptual scheme presented section 2.2 and have been discussed in detail in section 2.2.1.

The second regime might include larger, more complex thunderstorm systems, such as MCS (mesoscale convective systems) and multi-cell organizations, which generally exhibit higher discharge rates. Those cells might live through the same growing phase as the cells of regime one. But they develop several coexisting thunderstorm cells in their mature phase. This could explain the more irregularly shaped cell outlines and the abrupt onset of scatter, which are observed in the correlation diagrams. The scatter might also be induced, or amplified, when lightning events spread into attached stratiform regions (Carey et al., 2005; Lund et al., 2009). The mean IC discharge height per cell still increases steadily with storm size and discharge frequency in the second regime, despite the natural upper boundary in the tropopause. A study found that storm cells with stronger updrafts have higher mean lightning flash origins than storms with weaker updrafts (McCormick et al., 2002). This could explain the observation, provided it can be said that well organized storms generally develop more vigorous updrafts than single cells. Clearly, further investigations are needed to explain the true origin of the two regimes.

Recommended Studies and Outlook

To resolve internal intensity centers of electrical discharges and precipitation, relative thresholds could be introduced to the fixed thresholds, which are currently used to identify lightning-cells and radar-cells. A more detailed picture about storm structure and storm complexity could be obtained. This information might be a useful indicator to classify the storm organization.

Furthermore, the highly resolved two-dimensional radar data could be complemented by three-dimensional radar data. Volumetric radar scans are currently operationally available every 15 min. The low temporal resolution inhibits the monitoring of small-scaled, rapid thunderstorm developments. But still, additional three-dimensional information about the storm structure can be derived and long-term trends assessed.

To verify the interpretation of the two lifetime regimes found in the lifetime distributions (see section 4.4), it is suggested to test, whether the long-lived regime consists preferentially of multi-component ec-TRAM cell objects which comprise three or more sub-cells.

To verify the interpretation of the two cell regimes found in the correlation diagrams (see section 5.2), it is proposed to investigate the correlation functions of selected case-studies with respect to their form of storm organization. Furthermore, the absolute and the relative frequency of both cell regimes in thunderstorm life-cycles could be examined with respect to their development stage. For this study it might be reasonable to investigate the first period, as the thunderstorm develops, and the last period, as the thunderstorm dissipates, separately on linear axis, and the total life-cycles of completely recorded thunderstorms on a normalized time scale. It might also be reasonable to distinguish between the two lifetime regimes discussed in section 4.4. The interpretation holds, if short-lived cells are found primarily within the first regime throughout their whole lifetime and if the second regime appears mostly in the mature state of long-lived cells.

By computing a statistical mean of thunderstorm life-cycles the general existence and the reliability of a conceptual scheme could be verified for the ec-TRAM approach. For this study, it might be reasonable to investigate the first period and the final period of a thunderstorm life-cycle separately and on a linear time scale. Then, it can be examined, whether the development and the dissipation stage follow general rules. To investigate the existence of a general conceptual scheme, completely recorded life-cycles could be averaged on a normalized lifetime scale. It will be reasonable to distinguish between cell life-cycles from different lifetime regimes, which are found in the lifetime frequency distribution (see section 4.4).

It would be an important finding for thunderstorm nowcasting, if it is possible to relate storm parameters, like storm size, intensity, discharge characteristics, and storm persistence with storm organization. If it is further found that reliable norm life-cycles exist for different storm types, specified conceptual schemes could be used to assist the

storm prediction and complement the spatial nowcasts with information about general storm characteristics and the expected danger potential, once the storm type is assessed.

Apart from that, the existence of fit functions, which describe the correlations so remarkably clear, could probably improve current lightning discharge parameterizations. The fit functions can be used either as a benchmark for current lightning parameterization concepts, or they might be directly used in climate models. In any case, a comparison with other lightning parameterizations could be done, since some parameterization functions are based on cloud extension (Price and Rind, 1992) or precipitation (Allen and Pickering, 2002). Furthermore, a function, which describes the IC to CG ratios based on CG events could be derived and probably be compared with other relations, such as the relation given by Price and Rind (1993). A reliable function to calculate IC events as a function of CG flashes would be especially useful, since almost all long-range lightning localization networks record primarily CG flashes according to their own specification. For all comparative studies it has to be considered that lightning parameterization routines generally calculate lightning flashes. The correlation functions presented in this study rely on lightning events as they are recorded by LINET. They have not been clustered to flashes yet (see section 3.2.1).

Parts of the ec-TRAM algorithm will be implemented in the operational nowcasting tool wxFusion, which is currently developed at the DLR within the DLR project '*Weather and Flying*'. The mutual benefits of a combined usage of the algorithms ec-TRAM and Cb-TRAM are demonstrated in section 5.1. Cb-TRAM assesses the early stages of thunderstorm development and nowcasts the first lightning events, while ec-TRAM monitors the further thunderstorm development after the first lightning events occurred. A combined tool could assess both, convection initiation as well as small-scale storm developments. A further improvement in nowcast quality can be expected with the upgrade of the current conventional radar network to a polarimetric radar network, which is planned in Germany for the next years by the DWD. Furthermore, it is planned to employ ec-TRAM as steering aid for the DLR radar POLDIRAD to support a systematic, targeted, and some time probably automated thunderstorm tracking.

Appendix A

Appendix

A.1 Definition of Radio Wave Frequency Bands

Table A.1: List of frequency bands used for radio waves according to International Telecommunications Union (ITU) radio regulations.

| Designation | | Frequency | | Wavelength | |
|-------------|--------------------------|-----------|-------------|------------|--------------|
| ELF | extremely low frequency | 3 Hz | to 30 Hz | 100 000 km | to 10 000 km |
| SLF | superlow frequency | 30 Hz | to 300 Hz | 10 000 km | to 1 000 km |
| ULF | ultralow frequency | 300 Hz | to 3000 Hz | 1 000 km | to 100 km |
| VLF | very low frequency | 3 kHz | to 30 kHz | 100 km | to 10 km |
| LF | low frequency | 30 kHz | to 300 kHz | 10 km | to 1 km |
| MF | medium frequency | 300 kHz | to 3000 kHz | 1 km | to 100 m |
| HF | high frequency | 3 MHz | to 30 MHz | 100 m | to 10 m |
| VHF | very high frequency | 30 MHz | to 300 MHz | 10 m | to 1 m |
| UHF | ultrahigh frequency | 300 MHz | to 3000 MHz | 1 m | to 10 cm |
| SHF | superhigh frequency | 3 GHz | to 30 GHz | 10 cm | to 1 cm |
| EHF | extremely high frequency | 30 GHz | to 300 GHz | 1 cm | to 1 mm |

A.2 Definition of Box-And-Whisker Plot

A box-and-whisker diagram is a simplified graphical description of a frequency distribution and consists of five characteristical points (compare with figure A.1). The definition of the box is uniform. The bottom and the top of the box mark the 25th and the 75th percentile (lower and upper quartile, respectively) and their distance illustrates the interquartile range (IQR). The line in the box illustrates the 50th percentile (median). Whereas the definition of the box is clear, the definition of the whiskers differ. In the box-and-whisker graphs presented within this work, the lower whisker represents the lowest datum, which is found within $1.5 \times \text{IQR}$ below the lower quartile, and the higher whisker represents the highest datum, which is found within $1.5 \times \text{IQR}$ above the upper quartile. Data, which lie outside the whiskers, may be considered as outliers

and are plotted separately as crosses. They are not always shown. In this study, the box-and-whisker plots are further complemented by the mean value, indicated by green diamonds.

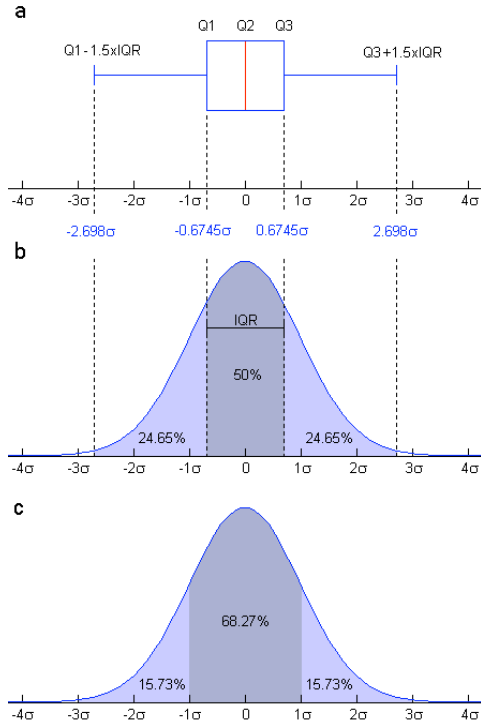


Figure A.1: Descriptive illustration of a box-and-whisker plot (a), derived for a normal probability distribution with a variance of σ (b and c). Q1, Q2, and Q3 denote the 25th, the 50th, and the 75th percentile, respectively, and IQR marks the interquartile range (graphic taken from Wikipedia (2010)).

A.3 Verification Methods for Dichotomous (Yes/No) Forecasts

A dichotomous forecast is a yes/no forecast and a dichotomous observation yes/no observation. The four combinations of yes/no forecasts and yes/no observations are

hit - event forecast to occur which did occur

miss - event forecast not to occur which did occur

false alarm - event forecast to occur which did not occur

correct negative - event forecast not to occur which did not occur.

To verify this type of forecast a contingency table, that shows the frequency of yes/no forecasts and occurrences is set up as

A large variety of categorical statistics are computed from the elements in the contingency table to describe particular aspects of forecast performance. The quality parameter used in this study are explained in the following. The explanation is taken from the homepage of The Centre for Australian Weather and Climate Research and can be found at www.cawcr.gov.au/projects/verification.

| | | observation | | |
|----------|--------------|---------------------|--------------------|---------------------|
| | | yes | no | total |
| forecast | yes | hits | false alarms | <i>forecast yes</i> |
| | no | misses | correct negatives | <i>forecast no</i> |
| | total | <i>observed yes</i> | <i>observed no</i> | <i>total</i> |

Table A.2: Example of a contingency table used for dichotomous forecast verification.

POD - Probability of Detection

The probability of detection (POD) answers the question of what fraction of the observed yes events were correctly forecast. It is defined as

$$\frac{'hits'}{'hits' + 'false alarms'}. \quad (\text{A.1})$$

The POD ranges from 0 to 1. A perfect score would achieve 1. The POD is sensitive to hits but ignores misses. The value is sensitive to the climatological frequency of the event and good for rare events. Since the POD can artificially be improved by issuing more yes forecasts to increase the number of hits it is reasonable to use it in combination with the false alarm ratio (below).

FAR - False Alarm Ratio

The false alarm ratio addresses the question of what fraction of the predicted yes events actually did not occur, thus were false alarms. The FAR is defined as

$$\frac{'false alarms'}{'hits' + 'false alarms'}. \quad (\text{A.2})$$

The FAR ranges from 0 to 1. A perfect score would achieve 0. The FAR is sensitive to false alarms, but ignores misses. The value is sensitive to the climatological frequency of events and good for frequent events. It should be used in conjunction with the probability of detection (above).

CSI - Critical Success Index

The critical success index, also called threat score, gives answer to the question of how well did the forecast yes events correspond to the observed yes events. The CSI is defined as

$$\frac{'hits'}{'hits' + 'misses' + 'false alarms'}. \quad (\text{A.3})$$

The CSI ranges from 0 to 1. A perfect score would achieve 1. The CSI measures the fraction of observed and/or forecast events that were correctly predicted. It is sensitive to hits and penalizes misses and false alarms. The CSI depends on the climatological frequency of events becoming poorer for rarer events.

A.4 SQL Database

A.4.1 Tabular Structure and Linkages

All cell parameters derived by ec-TRAM are stored in a relational database with *structured query language* (SQL) used as management system. The cell parameters of every identified cell are stored as attributes of one tuple in the respective database relation and every tuple is assigned a unique ID. Since relations can be described as tables the rows represent the tuple with the cell attributes and the columns represent the different cell entries.

The structure of the database is designed to make the subsequent data analyses as flexible and easy as possible. Figure A.2 illustrates the structure of the database. The database structure is adopted to the definition of an *eccell* and the tracking concept of ec-TRAM (see section 3.1). So cell parameters of *radcells* and *licells*, which are tracked separately and independently, are also stored in two independent main database relations, namely database *radcell* (*db-radcell*) and database *licell* (*db-licell*). Every database entry is assigned a unique ID. Global *eccell* properties like cell area, cell centroid, etc. are stored in the database relation database *eccell* (*db-eccell*) and the entries are also marked with unique IDs. But unlike *radcells* or *licells* an *eccell* can consist of one single *radcell* or one single *licell* as well as the combination of one or more *radcells* with one or more *licells*. Therefore the relationship between *eccell:radcell:licell* is $1:n:m$. So to assess not only the global cell characteristic but also the cell properties of the single cell participants of the *eccell* complex, like e.g. the electrical discharge characteristic of the *licell*(s) or the reflectivity pattern of the *radcell*(s), it is necessary to connect every *eccell* entry in the *db-eccell* to the respective *licell* entries and *radcell* entries. This requires an extra database relation, here called database *eccell_id* (*db-eccell_id*), which stores the ID of a specific *eccell* with the IDs of all associated *licell* and *radcell* entries. The *eccell* ID is used as primary key while the *licell* and *radcell* IDs are used as foreign keys to link the *eccell* entries in *db-eccell* with the associated *licell* and *radcell* entries in *db-licell* and *db-radcell*, respectively. In *db-eccell_id* every *licell* - *radcell* - combination of an *eccell* has a separate entry.

So if for example an *eccell* consists of one *licell*, one *radcell* or exactly one *licell* and one *radcell* there will be only one entry in *db-eccell_id* with the one cell entry ID from *db-eccell* and the respective entry IDs in *db-radcell* and *db-licell*. But if the *eccell* consists of, for example, one *radcell* and two *licells* then two cell entries are required in *db-eccell_id* to describe the cell relations completely. One with the *eccell* entry ID in *db-eccell*, the *radcell* entry ID in *db-radcell* and the one *licell* entry ID in *db-licell* and another entry again with the *eccell* entry ID in *db-eccell* and the *radcell* entry ID in *db-radcell* but now with the other *licell* entry ID in *db-licell*.

A.4.2 Cell Parameters

To avoid database relations with too many attributes the main database relations are split into one or more subrelations. The subrelations follow a simple 1:1 relationship so

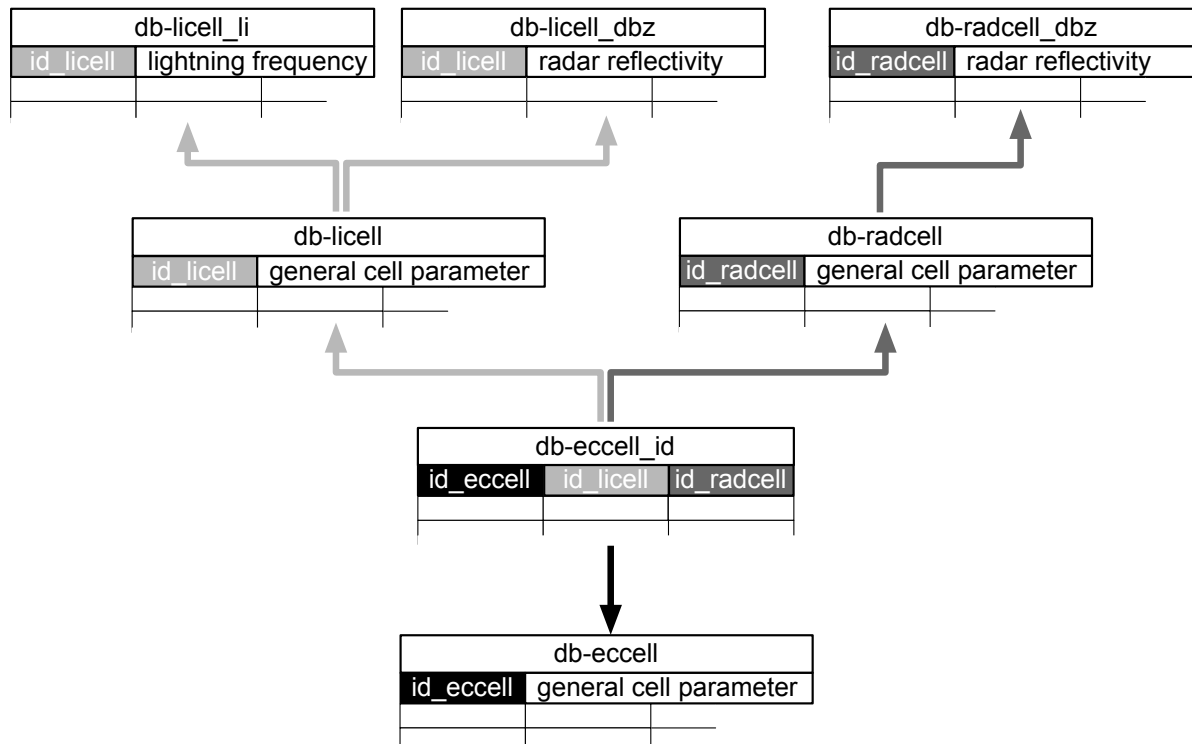


Figure A.2: Scheme of database relationship for the cell parameter tables computed by rad-TRAM, li-TRAM, and ec-TRAM.

it is sufficient to store the entry IDs of the main relations as foreign keys in the subrelations. Those cell attributes which describe spatial cell characteristic, e.g. cell area, cell centroid, or cell displacement, and cell events, e.g. cell splitting or cell merging, are stored in the main relations *db-eccell*, *db-radcell*, and *db-licell*. Table A.3 lists the main relation attributes for *radcells* and *licells* and table A.4 lists the main relation attributes for *eccells*. For *db-radcell* exists one subrelation, database *radcell_dbz* (*db-radcell_dbz*), which stores the reflectivity characteristic of the *radcells*. For *db-licell* two subrelations are introduced. One, database *licell_li* (*db-licell_li*), stores the discharge characteristic and the other one, database *licell_dbz* (*db-licell_dbz*), stores the reflectivity characteristic of the *licells*. Table A.5 lists the attributes of the subrelations *db-licell_dbz* and *db-radcell_dbz* and table A.5 lists the attributes of the subrelation *db-licell_li*. The system leaves the possibility to add other subrelations.

Table A.3: List of main cell attributes for *licells* and *radcells* of the SQL database main relations *db-licell* and *db-radcell*.

| attribute | data type | description |
|----------------|-----------|--|
| id | int | tuple id used as primary key |
| timestamp | timestamp | date and time of calculation run |
| date | date | research day |
| time | time | research time |
| number | int | cell number |
| inarea | int | [0,1] [cell close or out of domain margin, cell totally in domain] |
| merge | int | $n \in \mathbb{N}^-$, $ n $: number of cells participating in a cell merging, current cell is the major cell, cell number is continued |
| split | int | $n \in \mathbb{N}^+$, $ n $: number of cells participating in a cell splitting, current cell number already existed |
| merge_cut | int | same as 'merge', but only used, if current cell is a minor cell which cell record is closed at this time step |
| merge_celldr | varchar | if current cell is a minor cell: number of major cell |
| merge_parents | varchar | if current cell is a major cell: number of merged minor cells |
| split_cut | int | same as 'split', but only used if current cell is a child cell which cell record is newly opened at this time step |
| split_celldr | varchar | if current cell is a splitted child cell: number of splitting parent cell |
| split_children | varchar | if current cell is a splitting cell: number of the other splitted children cells |
| family | varchar | list of cell numbers of the complete life-cycle tree |
| area | float | cell area |
| ratio_cell | float | fraction of cell overlap to current cell from cell contours finally used for cell tracking |
| ratio_tot | float | fraction of cell overlap from all cell candidates for cell tracking |
| ratio_family | varchar | list of overlap fraction of all cell candidates for cell tracking |
| position | point | position of cell center of gravity for <i>radcells</i> and geometrical cell center for <i>licells</i> in (lat/lon) |
| displace | point | two-dimensionally computed cell displacement predicted for the cell center of gravity for the last time step in (km,km) |
| move | point | two-dimensionally computed cell displacement predicted for the cell center of gravity for the next time step in (km,km) |
| velocity | point | in <i>db-radcell</i> only: cell velocity vector calculated as mean value from cell displace vector field covered by cell area in (m/s,m/s) |
| velocity_abs | float | in <i>db-radcell</i> only: absolute cell velocity calculated from cell parameter 'velocity' in m/s |
| velocity_angle | float | in <i>db-radcell</i> only: angle between cell velocity and east - west direction in degree |

continued on next page

| | | |
|--------------------|-------|---|
| velocity_abs_rel | float | in <i>db-radcell</i> only: relative absolute velocity between cell velocity and mean velocity of entire respective coherent reflectivity field in <i>m/s</i> |
| velocity_angle_rel | float | in <i>db-radcell</i> only: relative angle between cell velocity vector and mean velocity vector of entire respective coherent reflectivity field in <i>degree</i> |

Table A.4: List of main cell attributes for *eccells* of the database main relation *db-ecell*.

| attribute | data type | description |
|--------------|-----------|---|
| id | int | tuple id used as primary key |
| timestamp | timestamp | date and time of calculation run |
| date | date | research day |
| time | time | research time |
| number | int | cell number |
| first_entry | varchar | type of first cell entry. 'rad': only <i>radcell</i> , 'li': only <i>licell</i> , 'ec': <i>licell</i> - <i>radcell</i> - complex. |
| last_entry | varchar | type of last cell entry. 'rad': only <i>radcell</i> , 'li': only <i>licell</i> , 'ec': <i>licell</i> - <i>radcell</i> - complex. |
| sum_licell | int | number of <i>licells</i> being part of the <i>eccell</i> complex |
| sum_radcell | int | number of <i>radcells</i> being part of the <i>eccell</i> complex |
| nr_licell | varchar | list of cell numbers of <i>licells</i> being part of the <i>eccell</i> complex |
| nr_radcell | varchar | list of cell numbers of <i>radcells</i> being part of the <i>eccell</i> complex |
| id_licell | varchar | list of cell IDs of <i>licells</i> being part of the <i>eccell</i> complex |
| id_radcell | varchar | list of cell IDs of <i>radcells</i> being part of the <i>eccell</i> complex |
| overlap | float | ratio of overlapping area to total <i>eccell</i> area |
| overlap_li | float | fraction <i>licell</i> area which is overlapping with <i>radcells</i> |
| inarea | int | all <i>eccell</i> participants are in the research domain |
| merge | int | sum of <i>licells</i> and <i>radcells</i> which are involved in cell merging process in current time step |
| merge_cut | int | sum of <i>licells</i> and <i>radcells</i> which disappeared in current time step due to cell merging |
| split | int | sum of <i>licells</i> and <i>radcells</i> which are involved in cell splitting process in current time step |
| split_cut | int | sum of <i>licells</i> and <i>radcells</i> which appeared in current time step due to cell splitting |
| area | float | total <i>eccell</i> area |
| area_licell | char | list of all cell areas of <i>licell</i> compounds |
| area_radcell | char | list of all cell areas of <i>radcell</i> compounds |
| position | point | position of geometrical cell center of <i>eccell</i> in (lat/lon) |

continued on next page

| | | |
|----------------|-------|--|
| displace | point | two-dimensionally computed cell displacement in km predicted for the geometrical <i>ecell</i> center for the last time step in (km,km) |
| move | point | two-dimensionally computed cell displacement predicted for the cell center for the next time step in (km,km) |
| velocity | point | not used |
| velocity_abs | float | not used |
| velocity_angle | float | not used |

Table A.5: List of reflectivity attributes for *licells* and *radcells* of the database subrelations *db-licell_dbz* and *db-radcell_dbz*.

| attribute | data type | description |
|-------------------------|-----------|--|
| id | int | tuple id used as primary key |
| timestamp | timestamp | date and time of calculation run |
| date | date | research day |
| time | time | research time |
| nr_licell or nr_radcell | varchar | cell number of associated <i>licell</i> or <i>radcell</i> |
| id_licell or id_radcell | varchar | cell id of associated <i>licell</i> or <i>radcell</i> |
| rainrate | float | estimated total rainrate of the cell calculated for radar reflectivity covered by the cell area after Jones (1956) |
| dbz_min | int | minimum reflectivity value found within cell contour |
| dbz_max | int | maximum reflectivity value found within cell contour |
| dbz_mean | float | mean value of reflectivity values found within cell contour |
| dbz_median | float | median of reflectivity values found within cell contour |
| dbz_stddev | float | standard deviation of reflectivity values found within cell contour |
| quantile25 | float | 25th percentile of reflectivity values found within cell contour |
| quantile50 | float | 50th percentile of reflectivity values found within cell contour |
| quantile75 | float | 75th percentile of reflectivity values found within cell contour |
| dbz_gradient | float | maximum gradient found in cell reflectivity field |
| dbz_0 | int | percentage of pixels with reflectivity interval 0 – 5 dBZ related to the total number of cell pixels |
| dbz_5 | int | like dbz_0 for a reflectivity interval of 5 – 10 dBZ |
| dbz_10 | int | like dbz_0 for a reflectivity interval of 10 – 15 dBZ |
| dbz_15 | int | like dbz_0 for a reflectivity interval of 15 – 20 dBZ |
| dbz_20 | int | like dbz_0 for a reflectivity interval of 20 – 25 dBZ |
| dbz_25 | int | like dbz_0 for a reflectivity interval of 25 – 30 dBZ |
| dbz_30 | int | like dbz_0 for a reflectivity interval of 30 – 34 dBZ |
| dbz_34 | int | like dbz_0 for a reflectivity interval of 34 – 37 dBZ |

continued on next page

| | | |
|--------|-----|---|
| dbz_37 | int | like dbz_0 for a reflectivity interval of 37 – 40 dBZ |
| dbz_40 | int | like dbz_0 for a reflectivity interval of 40 – 43 dBZ |
| dbz_43 | int | like dbz_0 for a reflectivity interval of 43 – 46 dBZ |
| dbz_46 | int | like dbz_0 for a reflectivity interval of 46 – 49 dBZ |
| dbz_49 | int | like dbz_0 for a reflectivity interval of 49 – 51 dBZ |
| dbz_51 | int | like dbz_0 for a reflectivity interval of 51 – 53 dBZ |
| dbz_53 | int | like dbz_0 for a reflectivity interval of 53 – 55 dBZ |
| dbz_55 | int | like dbz_0 for a reflectivity interval of 55 – 59 dBZ |
| dbz_59 | int | like dbz_0 for a reflectivity interval of > 59 dBZ |

Table A.6: List of electrical discharge attributes for *licells* of the database subrelation *db-licell_li*.

| attribute | data type | description |
|------------|-----------|--|
| id | int | tuple id used as primary key |
| timestamp | timestamp | date and time of calculation run |
| date | date | research day |
| time | time | research time |
| nr_licell | varchar | cell number of associated <i>licell</i> |
| id_licell | varchar | cell id of associated <i>licell</i> |
| count | int | total number of IC discharges in the cell |
| mean | float | mean value of IC discharge height |
| min | float | minimum value of IC discharge height |
| max | float | maximum value of IC discharge height |
| stddev | float | standard deviation of IC discharge height |
| quantile25 | float | 25th percentile of IC discharge height |
| quantile50 | float | 50th percentile of IC discharge height |
| quantile75 | float | 75th percentile of IC discharge height |
| cnt_tot | int | total number of TL discharges in the cell |
| cnt_ic | int | total number of IC discharges in the cell |
| cnt_cg | int | total number of CG discharges in the cell |
| dens_tot | float | TL discharge density per cell area calculated as ratio of cnt_tot to cell area |
| dens_ic | float | IC discharge density per cell area calculated as ratio of cnt_ic to cell area |
| dens_cg | float | CG discharge density per cell area calculated as ratio of cnt_cg to cell area |

A.5 Linear Lightning-Cell Parameter Correlation Plots with Distribution Spread

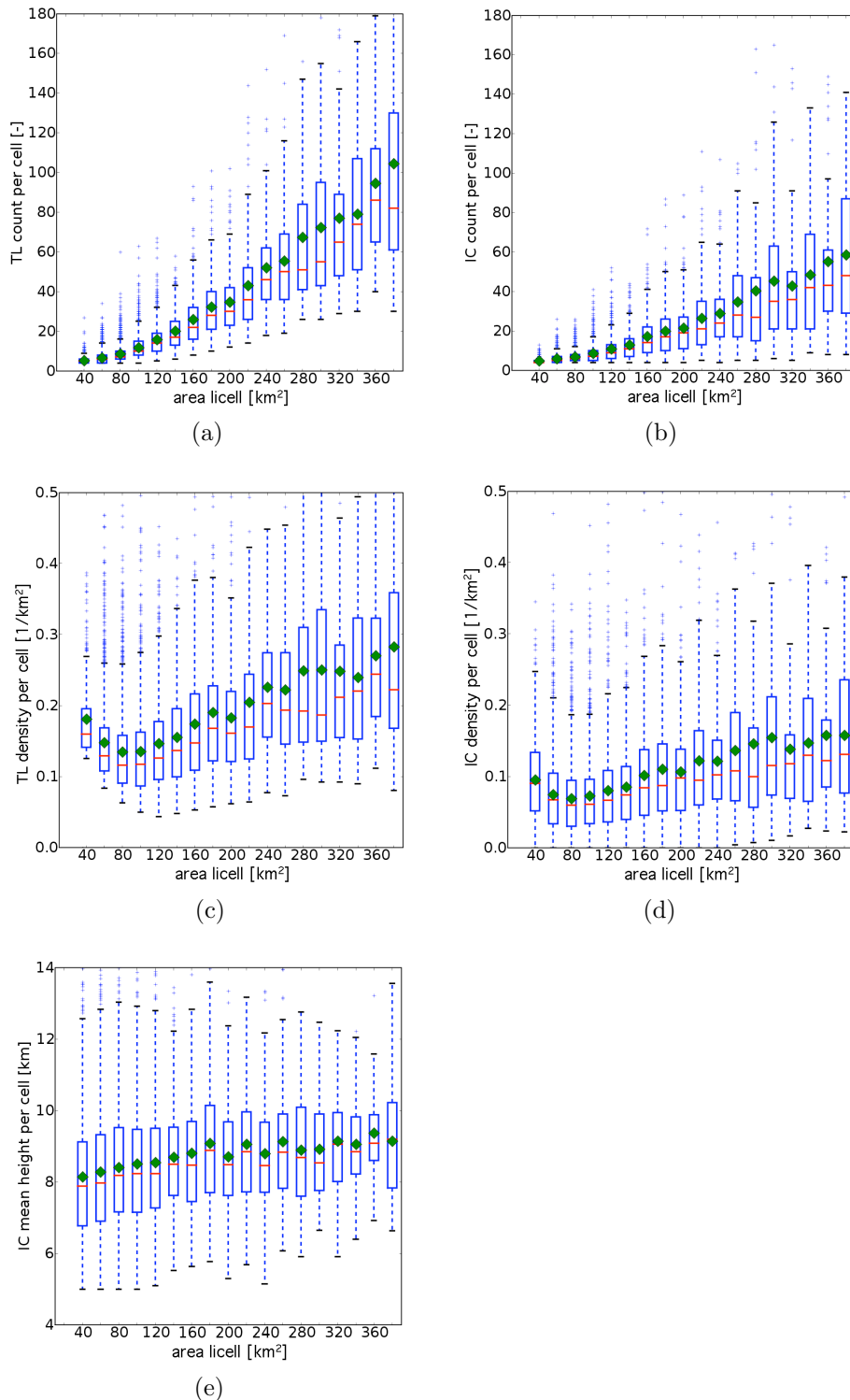


Figure A.3: Linear correlation plots with median, 25th, and 75th percentile of the distribution as red-blue box-and-whisker plots (see appendix A.2) for (a) TL and (b) IC discharge frequencies per *licell* versus *licell* area, (c) TL and (d) IC discharge density per *licell* versus *licell* area, (e) IC mean discharge height per *licell* versus *licell* area for total data set recorded during summer of 2008.

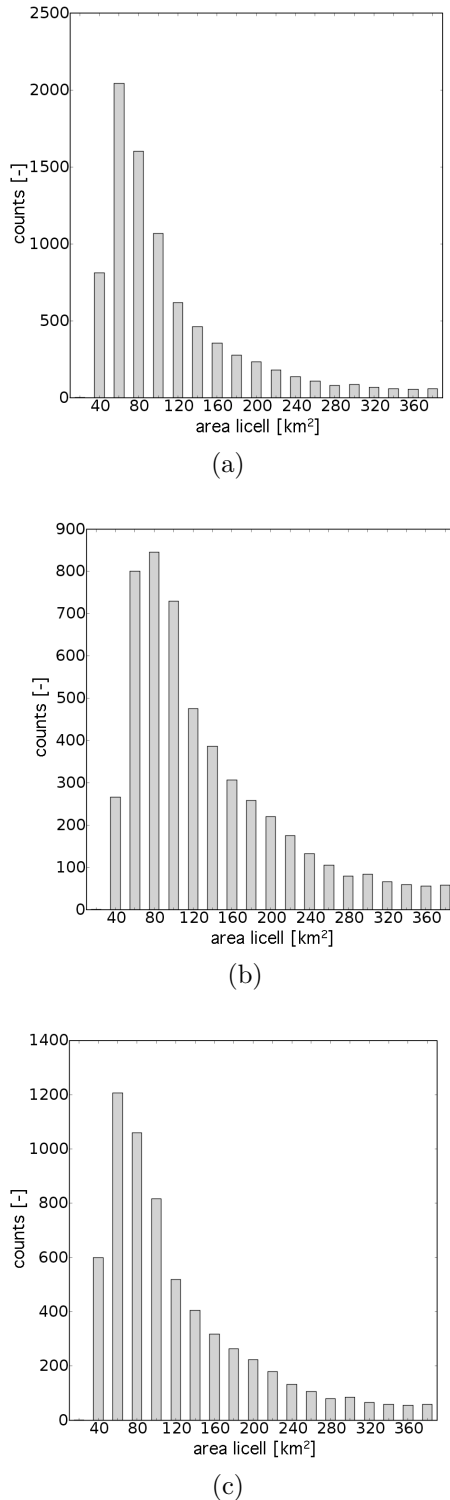


Figure A.4: Count statistics for studies in figure A.3. (a) for figure A.3a and A.3c, (b) for figure A.4b and A.3d, and (c) for figure A.3e.

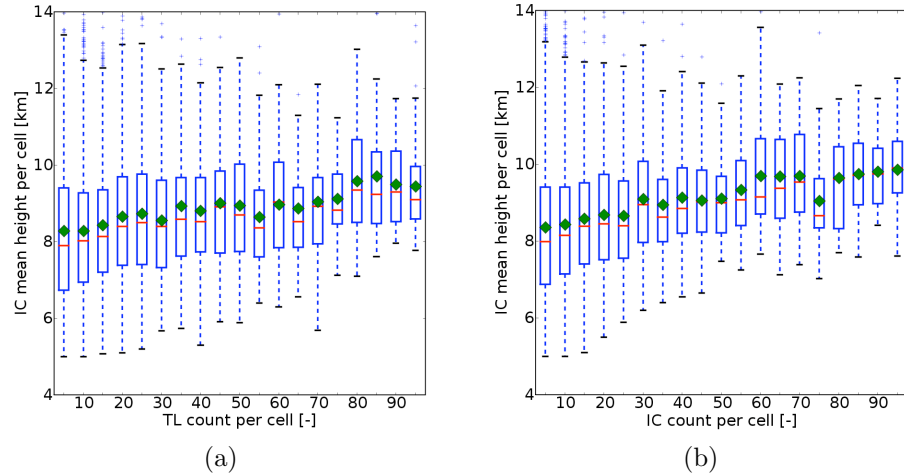


Figure A.5: Linear correlation plots with median, 25th, and 75th percentile of the distribution as red-blue box-and-whisker plots (see appendix A.2) IC mean discharge height per *cell* versus (a) TL and (b) IC discharge frequencies for total data set recorded during summer of 2008.

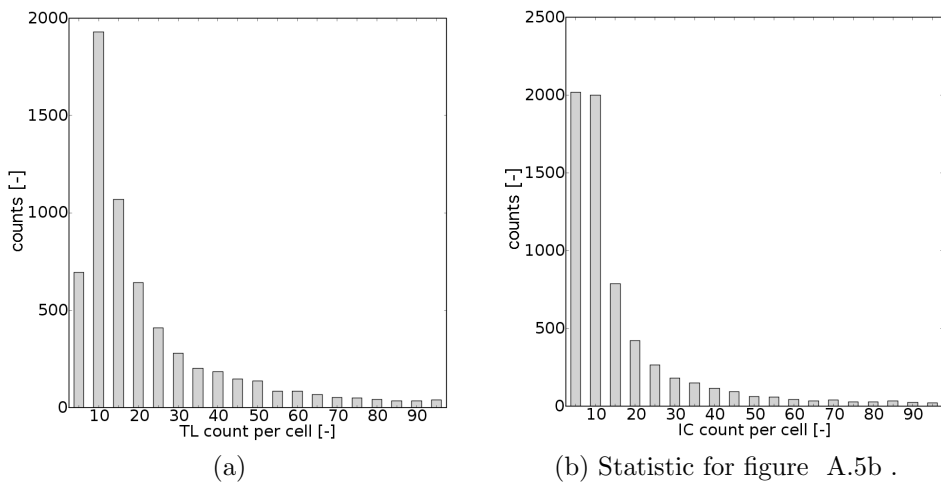


Figure A.6: Count statistics for studies in figure A.3. (a) for figure A.3 and (b) for figure A.5.

Acknowledgements

I want to thank Prof. Schumann, my first supervisor, for patronizing my thesis at the DLR. His critical comments helped substantially to improve the work. I would like to thank Prof. Betz, my second supervisor, for his special interest and his kindest support throughout the whole thesis. I want to express my deepest thanks to Hartmut Höller for his always unhesitating tutoring, his kindest support and good advices. And I am deeply grateful to Nikolai Dotzek for his very valuable mentoring and his precious support.

Sincerest thanks go to Prof. George Craig for his always present, encouraging interest and his unhesitant and especially invaluable advice. And thanks to Thomas Gerz for his always open doors. I want to express my deepest gratitude to Prof. Hitzenberger, former tutor of my diploma thesis, for her continuing precious patronage and her especially helpful and always honest advice.

Many thanks to nowcast GmbH, for the throughout cooperative collaboration during the project RegioExAKT (Regional Risk of Convective Extreme Weather Events: User-oriented Concepts for Climatic Trend Assessment and Adaptation). Especially, I want to thank Gitti Montag, Kersten Schmidt, Michl Zich, and Andreas Besner for the unforgettably great and informative time during my secondment at nowcast GmbH. Furthermore, I want to thank Kersten Schmidt for the always helpful and always enjoyable discussions as my office-mate at the DLR.

Thanks to all the people working within the project RegioExAKT for the very interesting workshops and the pleasant time.

I want to thank Caroline Forster, Kirstin Kober, Jens Reimann, Monika Pfeifer, and Patrick Tracksdorf for their highly valuable introduction into the matters of radar and nowcasting. Furthermore, I want to thank Caroline Forster, Arnold Tafferer, and Heidi Huntrieser for their deep and honest interest, the good and welcome discussions, and their support. Special thanks to Johannes Dahl, Helge Tuschy, and Jan Hoffmann for their patient and extraordinary enjoyable personal lectures with subsequent discussion on the basic problems of meteorology.

Thank you to the PHD and ex-PHD gang of the Institute of Atmospheric Research at the DLR for the unforgettable tremendous and the welcoming and effective after work distractions. My deepest thanks go to all my friends for their company, their great support, and their simply being best friends.

Finally, but most of all, I want to express my profoundest thanks to my wonderful family, especially my parents, my brother, my grandmother, and Christian, for all their encouragements, their support, and their always present best wishes and care.

Bibliography

D. J. Allen and K. E. Pickering. Evaluation of lightning flash rate parameterizations for use in a global chemical transport model. *Journal of Geophysical Research-Atmospheres*, 107 (D23):4711, 2002.

O. Altaratz, Z. Levin, and Y. Yair. Winter thunderstorms in Israel: A study with lightning location systems and weather radar. *Monthly Weather Review*, 129(5):1259–1266, 2001.

B. Baker, M. B. Baker, E. R. Jayaratne, J. Latham, and C. P. R. Saunders. The influence of diffusional growth rates on the charge transfer accompanying rebounding collisions between ice crystals and soft hailstones. *Quarterly Journal of the Royal Meteorological Society*, 113: 1193–1215, 1987.

S. L. Barnes and C. W. Newton. *Thunderstorms in the synoptic setting*. Thunderstorm Morphology and Dynamics, 1983.

L. J. Battan. *Radar observations of the atmosphere*. University of Chicago Press, 1973.

I. Bertram and G. J. Mayr. Lightning in the eastern Alps 1993–1999, part I: Thunderstorm tracks. *Natural Hazards and Earth System Sciences*, 4:501–511, 2004.

H. D. Betz, K. Schmidt, B. Fuchs, W. P. Oettinger, and H. Höller. Cloud lightning: detection and utilization for total lightning measured in the VLF/LF regime. *Journal of Lightning Research*, 2:1–17, 2007.

H. D. Betz, T. C. Marshall, M. Stolzenburg, K. Schmidt, W. P. Oettinger, E. Defer, J. Konarski, P. Laroche, and F. Dombai. Detection of in-cloud lightning with VLF/LF and VHF networks for studies of the initial discharge phase. *Geophysical Research Letters*, 35(23):L23802, 2008.

H. D. Betz, K. Schmidt, P. Laroche, P. Blanchet, W. P. Oettinger, E. Defer, Z. Dziewit, and J. Konarski. LINET: An international lightning detection network in Europe. *Atmospheric Research*, 91(2-4):564–573, 2009a.

H. D. Betz, U. Schumann, and P. Laroche. *Lightning: principles, instruments and applications. Review of modern lightning research*. Springer Verlag, 2009b.

D. J. Boccippio, W. Koshak, R. Blakeslee, K. Driscoll, D. Mach, D. Buechler, W. Boeck, H. J. Christian, and S. J. Goodman. The Optical Transient Detector (OTD): Instrument characteristics and cross-sensor validation. *Journal of Atmospheric and Oceanic Technology*, 17(4):441–458, 2000.

D. J. Boccippio, K. L. Cummins, H. J. Christian, and S. J. Goodman. Combined satellite- and surface-based estimation of the intracloud - cloud-to-ground lightning ratio over the continental United States. *Monthly Weather Review*, 129(1):108–122, 2001.

P. Bonelli and P. Marcacci. Thunderstorm nowcasting by means of lightning and radar data: algorithms and applications in northern Italy. *Natural Hazards and Earth System Sciences*, 8(5):1187–1198, 2008.

V. N. Bringi and V. Chandrasekar. *Polarimetric Doppler Weather Radar: Principles and Applications*. Cambridge University Press, 2001.

V. N. Bringi, K. Knupp, A. Detwiler, L. Liu, I. J. Caylor, and R. A. Black. Evolution of a Florida thunderstorm during the Convection and Precipitation/Electrification Experiment: The case of 9 August 1991. *Monthly Weather Review*, 125(9):2131–2160, 1997.

E. C. Bruning, W. D. Rust, T. J. Schuur, D. R. MacGorman, P. R. Krehbiel, and W. Rison. Electrical and polarimetric radar observations of a multicell storm in telex. *Monthly Weather Review*, 135(2525–2544), 2007.

H. R. Byers and R. R. Jr Braham. Thunderstorm structure and circulation. *Journal of the Atmospheric Sciences*, 5(3):71–86, 1948.

L. D. Carey and S. A. Rutledge. A multiparameter radar case study of the microphysical and kinematic evolution of a lightning producing storm. *Meteorology and Atmospheric Physics*, 59(33–64), 1996.

L. D. Carey and S. A. Rutledge. Electrical and multiparameter radar observations of a severe hailstorm. *Journal of Geophysical Research-Atmospheres*, 103(D12):13979–14000, 1998.

L. D. Carey, M. J. Murphy, T. L. McCormick, and N. W. S. Demetriades. Lightning location relative to storm structure in a leading-line, trailing-stratiform mesoscale convective system. *Journal of Geophysical Research*, 110:D03105, 2005.

H. Christian, R. Blakeslee, S. Goodman, D. Mach, M. Stewart, D. Buechler, W. Koshak, J. Hall, W. Boeck, K. Driscoll, et al. The lightning imaging sensor. In *NASA conference publication*, pages 746–749. NASA, 1999.

V. Cooray, editor. *The lightning flash*. 34. IEE Power & Energy, 2003.

V. Cooray. Propagation effects on radiation field pulses generated by cloud lightning flashes. *Journal of atmospheric and solar-terrestrial physics*, 69(12):1397–1406, 2007.

V. Cooray, M. Fernando, T. Sørensen, T. Götschl, and A. Pedersen. Propagation of lightning generated transient electromagnetic fields over finitely conducting ground. *Journal of Atmospheric and Solar-Terrestrial Physics*, 62(7):583–600, 2000.

K. L. Cummins and M. J. Murphy. An Overview of Lightning Locating Systems: History, Techniques, and Data Uses, With an In-Depth Look at the US NLDN. *IEEE Transactions on Electromagnetic Compatibility*, 51(3):499, 2009.

J. G. Dash, B. L. Mason, and J. S. Wetzlaufer. Theory of charge and mass transfer in ice-ice collisions. *Journal of Geophysical Research*, 106(D17):20395–20402, 2001.

N. W. S. Demetriades and R. L. Holle. Long range lightning nowcasting applications for tropical cyclones. In *Preprints, Conf. Meteorology Application of Lightning Data, Atlanta*, 2006.

N. W. S. Demetriades, M. J. Murphy, R. L. Holle, and P. Richard. The importance of total lightning in the future of weather nowcasting. In *Preprints, Symposium on Planning, Nowcasting, and Forecasting in the Urban Zone*, pages 11–15, 2004.

M. Dixon and G. Wiener. TITAN: Thunderstorm identification, tracking, analysis, and nowcasting—A radar-based methodology. *Journal of Atmospheric and Oceanic Technology*, 10(6):785–797, 1993.

C. A. Doswell and L. F. Bosart. Extratropical synoptic-scale processes and severe convection. *Meteorological Monographs*, 28:27–70, 2001.

C. A. Doswell III. The distinction between large-scale and mesoscale contribution to severe convection: A case study example. *Weather and Forecasting*, 2(1):3–16, 1987.

N. Dotzek, H. Höller, C. Théry, and T. Fehr. Lightning evolution related to radar-derived microphysics in the 21 July 1998 EULINOX supercell storm. *Atmospheric Research*, 56 (1-4):335–354, 2001.

R. J. Doviak and D. S. Zrnić. *Doppler radar and weather observations*. Academic Press, Inc., Orlando, 1984.

R. L. Dowden, J. B. Brundell, and C. J. Rodger. VLF lightning location by time of group arrival (TOGA) at multiple sites. *Journal of Atmospheric and Solar-Terrestrial Physics*, 64 (7):817–830, 2002.

J. R. Dwyer, H. K. Rassoul, M. Al-Dayeh, L. Caraway, A. Chrest, B. Wright, E. Kozak, J. Jerauld, M. A. Uman, V. A. Rakov, et al. X-ray bursts associated with leader steps in cloud-to-ground lightning. *Geophysical Research Letters*, 32:L01803, 2005.

K. A. Emanuel. Overview and definition of mesoscale meteorology. *Mesoscale Meteorology and Forecasting*, pages 1–17, 1986.

T. Fehr, N. Dotzek, and H. Höller. Comparison of lightning activity and radar-retrieved microphysical properties in eulinox storms. *Atmospheric Research*, 76(1-4):167–189, 2005.

C. Forster and A. Tafferner. Nowcasting and forecasting thunderstorms for air traffic with an integrated forecast system based on observations and model data. In *WMO Symposium on Nowcasting, Whistler, B.C., Canada, 30 August - 4 September 2009*, 2009a.

C. Forster and A. Tafferner. An integrated user-oriented weather forecast system for air traffic using real-time observations and model data. In *Proceedings of the European Air and Space Conference (CEAS), Manchester, UK, 26 - 29 October 2009*, 2009b.

U. Germann and I. Zawadzki. Scale-dependence of the predictability of precipitation from continental radar images. Part I: Description of the methodology. *Monthly Weather Review*, 130(12):2859–2873, 2002.

U. Germann and I. Zawadzki. Scale dependence of the predictability of precipitation from continental radar images. Part II: Probability forecasts. *Journal of Applied Meteorology*, 43 (1):74–89, 2004.

U. Germann, I. Zawadzki, and B. Turner. Predictability of precipitation from continental radar images. Part IV: Limits to prediction. *Journal of the Atmospheric Sciences*, 63(8): 2092–2108, 2006.

B. W. Golding. Nimrod: A system for generating automated very short range forecasts. *Meteorological Applications*, 5(01):1–16, 1998.

S. J. Goodman and D. R. MacGorman. Cloud-to-ground lightning activity in mesoscale convective complexes. *Monthly Weather Review*, 114(12):2320–2328, 1986.

A. V. Gurevich and K. P. Zybin. Runaway breakdown and the mysteries of lightning. *Physics today*, 58(5):37–43, 2005.

W. H. Hand. An object-oriented technique for nowcasting heavy showers and thunderstorms. *Meteorological Applications*, 3(1):31–41, 1996.

J. Handwerker. Cell tracking with TRACE3D—a new algorithm. *Atmospheric Research*, 61 (1):15–34, 2002.

A. M. Hering, C. Morel, G. Galli, S. Sénési, P. Ambrosetti, and M. Boscacci. Nowcasting thunderstorms in the Alpine region using a radar based adaptive thresholding scheme. In

Proceedings of ERAD, volume 1, 2004.

J. Hoffmann. *Entwicklung und Anwendung von statistischen Vorhersage-Interpretationsverfahren für Gewitternowcasting und Unwetterwarnungen unter Einbeziehung von Fernerkundungsdaten*. PhD thesis, Freie Universität Berlin, 2007.

R. L. Holle, R. E. López, R. Ortiz, C. H. Paxton, D. M. Decker, and D. L. Smith. The local meteorological environment of lightning casualties in central Florida. In *Preprints, 17th Conference on Severe Local Storms and Conference on Atmospheric Electricity, St. Louis, MO, Amer. Meteor. Soc*, pages 779–784, 1993.

H. Höller, M. Hagen, P. F. Meischner, V. N. Bringi, and J. Hubbert. Life cycle and precipitation formation in a hybrid-type hailstorm revealed by polarimetric and Doppler radar measurements. *Journal of the Atmospheric Sciences*, 51(17):2500–2522, 1994.

H. Höller, U. Finke, H. Huntrieser, M. Hagen, and C. Feigl. Lightning-produced NO_x (LINOX): Experimental design and case study results. *Journal of Geophysical Research*, 104:13911–13922, 1999.

H. Höller, H. D. Betz, K. Schmidt, R. V. Calheiros, P. May, E. Hougninou, and G. Scialom. Lightning characteristics observed by a VLF/LF lightning detection network (LINET) in Brazil, Australia, Africa and Germany. *Atmospheric Chemistry and Physics Discussions*, 9(2):6061–6146, 2009.

H. Huntrieser, U. Schumann, H. Schlager, H. Höller, A. Giez, H. D. Betz, D. Brunner, C. Forster, O. Pinto Jr, and R. Calheiros. Lightning activity in Brazilian thunderstorms during TROCCINOX: implications for NO_x production. *Atmospheric Chemistry and Physics*, 8:921–953, 2008.

A. R. Jameson, M. J. Murphy, and E. P. Krider. Multiple-parameter radar observations of isolated Florida thunderstorms during the onset of electrification. *Journal of Applied Meteorology*, 35(3):343–354, 1996.

R. H. Johns and C. A. Doswell III. Severe local storms forecasting. *Weather and Forecasting*, 7(4):588–612, 1992.

J. T. Johnson, P. L. MacKeen, A. Witt, E. D. W. Mitchell, G. J. Stumpf, M. D. Eilts, and K. W. Thomas. The storm cell identification and tracking algorithm: An enhanced WSR-88D algorithm. *Weather and Forecasting*, 13(2):263–276, 1998.

D. M. A. Jones. Rainfall drop size-distribution and radar reflectivity. *Illinois State Water Survey Div Urbana*, 1956.

T. Keenan, P. Joe, J. Wilson, C. Collier, B. Golding, D. Burgess, P. May, C. Pierce, J. Bally, A. Crook, et al. The Sydney 2000 world weather research programme forecast demonstration project. *Bulletin of the American Meteorological Society*, 84:1041–1054, 2003.

T. D. Keenan. Hydrometeor classification with a C-band polarimetric radar. *Australian Meteorological Magazine*, 52(1):23–31, 2003.

W. H. Klein, B. M. Lewis, and I. Enger. Objective prediction of five-day mean temperatures during winter. *Journal of the Atmospheric Sciences*, 16(6):672–682, 1959.

J. B. Klemp. Dynamics of tornadic thunderstorms. *Annual Review of Fluid Mechanics*, 19(1):369–402, 1987.

K. Kober and A. Tafferner. Tracking and nowcasting of convective cells using remote sensing data from radar and satellite. *Meteorologische Zeitschrift*, 18(1):75–84, 2009.

P. Lang. Cell tracking and warning indicators derived from operational radar products. In *Proceedings of the 30th International Conference on Radar Meteorology, Munich, Germany*,

pages 245–247, 2001.

L. Li, W. Schmid, and J. Joss. Nowcasting of motion and growth of precipitation with radar over a complex orography. *Journal of applied meteorology*, 34(6):1286–1300, 1995.

H. Liu and V. Chandrasekar. Classification of hydrometeors based on polarimetric radar measurements: Development of fuzzy logic and neuro-fuzzy systems, and in situ verification. *Journal of Atmospheric and Oceanic Technology*, 17(2):140–164, 2000.

R. E. Lopez and J. P. Aubagnac. The lightning activity of a hailstorm as a function of changes in its microphysical characteristics inferred from polarimetric radar observations. *Journal of Geophysical Research*, 102(D14):16799–16813, 1997.

N. R. Lund, D. R. MacGorman, T. J. Schuur, M. I. Biggerstaff, and W. D. Rust. Relationships Between Lightning Location and Polarimetric Radar Signatures in a Small Mesoscale Convective System. *Monthly Weather Review*, 2009.

Pfeifer M. *Evaluation of precipitation forecasts by polarimetric radar*. PhD thesis, Ludwig-Maximilians-Universität, 2007.

D. MacGorman, I. Apostolakopoulos, A. Nierow, M. J. Murphy, N. W. S. Demetriades, J. Cramer, and P. Krehbiel. Improved timeliness of thunderstorm detection from mapping a larger fraction of lightning flashes. In *Second Conference on Meteorological Applications of Lightning Data*, 2006.

D. R. MacGorman and W. D. Rust. *The Electrical Nature of Storm*. Oxford University Press, 1998.

D. R. MacGorman, D. W. Burgess, V. Mazur, W. D. Rust, W. L. Taylor, and B. C. Johnson. Lightning rates relative to tornadic storm evolution on 22 May 1981. *Journal of the Atmospheric Sciences*, 46(2):221–251, 1989.

D. R. MacGorman, J. M. Straka, and C. L. Ziegler. A lightning parameterization for numerical cloud models. *Journal of Applied Meteorology*, 40(3):459–478, 2001.

H. Mannstein, R. Meyer, and P. Wendling. Operational detection of contrails from NOAA-AVHRR-data. *International Journal of Remote Sensing*, 20(8):1641–1660, 1999.

V. Mazur and L. H. Ruhnke. Model of electric charges in thunderstorms and associated lightning. *Journal of geophysical research*, 103(D18):23299–23309, 1998.

T. L. McCormick, L. D. Carey, M. J. Murphy, and N. W. S. Demetriades. Three-dimensional radar and total lightning characteristics of mesoscale convective systems. *AGU Fall Meeting Abstracts*, pages B93+, dec 2002.

P. F. Meischner, I. Dölling, and M. Hagen. Polarimetrische radarmessungen in der meteorologie. *Annalen der Meteorologie*, 32, 1995.

V. Meyer, H. Höller, and Schmidt K. Betz, H.-D. Temporal evolution of total lightning and radar parameters of thunderstorms in southern germany and its benefit for nowcasting. *Proceedings: 5th European Conference on Severe Storms*, 10 2009.

S. M. Motley, L. D. Carey, B. L. Ely, R. E. Orville, J. Guynes, and M. J. Murphy. Total lightning characteristics of ordinary convection. In *19th International lightning Detection Conference, Tucson, Arizona, USA*, 2996.

C. Mueller, T. Saxen, R. Roberts, J. Wilson, T. Betancourt, S. Dettling, N. Oien, and J. Yee. NCAR auto-nowcast system. *Weather and Forecasting*, 18(4):545–561, 2003.

A. Nag, D. Tsalikis, and V. A. Rakov. Measurements of wideband electric fields and their derivatives in conjunction with HF and VHF radiatin produced by lightning discharges. In

AGU Fall Meeting Abstract, 2007.

D. Petersen, M. Bailey, W.H. Beasley, and J. Hallett. A brief review of the problem of lightning initiation and a hypothesis of initial lightning leader formation. *Journal of Geophysical Research-Atmospheres*, 113(D17):D17205, 2008.

C. E. Pierce, P. J. Hardaker, C. G. Collier, and C. M. Haggett. GANDOLF: A system for generating automated nowcasts of convective precipitation. *Meteorological Applications*, 7 (04):341–360, 2001.

C. Price and D. Rind. A Simple lightning parameterization for calculating global lightning distributions. *Journal of Geophysical Research*, 97:9919–9933, 1992.

C. Price and D. Rind. What determines the cloud-to-ground lightning fraction in thunderstorms? *Geophysical Research Letters*, 20:463–466, 1993.

C. Price, Y. Yair, A. Mugnai, K. Lagouvardos, M. C. Llasat, and S. Michaelides. Flash: A new EU project using lightning data to study mediterranean flash floods. In *13th International Conference on Atmospheric Electricity, August, 2007, Beijing, China*, 2007.

D. E. Proctor. Regions where lightning flashes began. *Journal of Geophysical Research-Atmospheres*, 96(D3), 1991.

V. A. Rakov and M. A. Uman. *Lightning: Physics and Effect*. Cambridge University Press, Cambridge, UK, September 2003.

R. E. Rinehart and E. T. Garvey. Three-dimensional storm motion detection by conventional weather radar. *Nature*, 273:287–289, 1978.

S. A. Rutledge and D. R. MacGorman. Cloud-to-ground lightning activity in the 10-11 june 1985 mesoscale convective system observed during the oklahoma-kansas pre-storm project. *Monthly Weather Review*, 116(7):1393–1408, 1988.

M. M. F. Saba, M. G. Ballarotti, and O. Pinto Jr. Negative cloud-to-ground lightning properties from high-speed video observations. *Journal of Geophysical Research-Atmospheres*, 111 (D3):D03101, 2006.

C. Saunders. Charge separation mechanisms in clouds. *Space Science Reviews*, 137(1):335–353, 2008.

C. P. R Saunders and S. L. Peck. Laboratory studies of the influence of the rime accretion rate on charge transfer during crystal/graupel collisions. *Journal of Geophysical Research*, 103(D12), 1998.

C. P. R Saunders, H. Bax-Norman, C. Emersic, E. E. Avila, and N. E. Castellano. Laboratory studies of the effect of cloud conditions on graupel/crystal charge transfer in thunderstorm electrification. *Quarterly Journal of the Royal Meteorological Society*, 132(621):2653–2674, 2006.

Kersten Schmidt. *Ortung und Analyse von Blitzentladungen mittels Registrierung von VLF-Atmospherics innerhalb eines Messnetzes*. PhD thesis, Ludwig-Maximilians-Universität, Munich, 2007. URL http://edoc.ub.uni-muenchen.de/6925/1/schmidt_kersten.pdf.

A. C. Schroth, M. S. Chandra, and P. F. Meischner. A C-band coherent polarimetric radar for propagation and cloud physics research. *Journal of Atmospheric and Oceanic Technology*, 4, 20, 24(5):804–822, 1988.

U. Schumann and H. Huntrieser. The global lightning-induced nitrogen oxides source. *Atmospheric Chemistry and Physics*, 7(14):3823–3907, 2007.

A. W. Seed. A dynamic and spatial scaling approach to advection forecasting. *Journal of Applied Meteorology*, 42(3):381–388, 2003.

T. A. Seliga and V. N. Bringi. Potential use of radar differential reflectivity measurements at orthogonal polarizations for measuring precipitation. *Journal of Applied Meteorology*, 23, 24(15):69–76, 1976.

D. Sentman. Schumann resonance spectra in a two-scale-height Earth-ionosphere cavity. *Journal of Geophysical Research*, 101:9479–9488, 1996.

X. M. Shao and P. R. Krehbiel. The spatial and temporal development of intracloud lightning. *Journal of geophysical research*, 101(D 21):26641–26668, 1996.

R. Solomon, V. Schroeder, and M. B. Baker. Lightning initiation - conventional and runaway-breakdown hypotheses. *Quarterly Journal of the Royal Meteorological Society*, 127(578):2683–2704, 2001.

K. M. Soul, E. J. Archibald, P. J. Hardaker, and A. Hounsell. Using the GANDOLF system as a tool to aid the forecasting of lightning strikes. *Meteorological Applications*, 9(02):229–238, 2002.

M. Stolzenburg, W. D. Rust, and T. C. Marshall. Electrical structure in thunderstorm convective regions 3. Synthesis. *Journal of Geophysical Research-Atmospheres*, 103(D12), 1998.

J. M. Straka, D. S. Zrnić, and A. V. Ryzhkov. Bulk hydrometeor classification and quantification using polarimetric radar data: Synthesis of relations. *Journal of Applied Meteorology*, 39(8):1341–1372, 2000.

T. Takahashi. Riming electrification as a charge generation mechanism in thunderstorms. *Journal of the Atmospheric Sciences*, 35(8):1536–1548, 1978.

S. A. Tessendorf, L. J. Miller, K. C. Wiens, and S. A. Rutledge. The 29 June 2000 supercell observed during STEPS. Part I: Kinematics and microphysics. *Journal of the Atmospheric Sciences*, 62(12):4127–4150, 2005.

M. A. Uman. *The lightning discharge*. Dover Pubns, 2001.

K. C. Wiens, S. A. Rutledge, and S. A. Tessendorf. The 29 June 2000 supercell observed during STEPS. Part II: Lightning and charge structure. *Journal of the Atmospheric Sciences*, 62 (12):4151–4177, 2005.

Wikipedia. <http://en.wikipedia.org/wiki/boxplot>, March 2010. URL <http://en.wikipedia.org/wiki/Boxplot>.

E. Williams, B. Boldi, A. Matlin, M. Weber, S. Hodanish, D. Sharp, S. Goodman, R. Raghavan, and D. Buechler. The behavior of total lightning activity in severe Florida thunderstorms. *Atmospheric Research*, 51(3-4):245–265, 1999.

E. R. Williams. Large-scale charge separation in thunderstorms. *Journal of Geophysical Research-Atmospheres*, 90(D4):6013–6025, 1985.

E. R. Williams. The tripole structure of thunderstorms. *Journal of Geophysical Research*, 94 (D11):13151–13167, 1989.

E. R. Williams. Problems in lightning physics. *Plasma Sources Science and Technology*, 15: S91–S108, 2006.

E. R. Williams, M. E. Weber, and R. E. Orville. The relationship between lightning type and convective state of thunderclouds. *Journal of Geophysical Research*, 1987.

J. W. Wilson, E. E. Ebert, T. R. Saxen, R. D. Roberts, C. K. Mueller, M. Sleigh, C. E. Pierce, and A. Seed. Sydney 2000 forecast demonstration project: convective storm nowcasting.

Weather and Forecasting, 19(1):131–150, 2004.

L. H. Y. Yeung, E. S. T. Lai, and S. K. S. Chiu. Lightning Initiation and Intensity Nowcasting Based on Isothermal Radar Reflectivity-A Conceptual Model. In *The 33rd International Conference on Radar Meteorology*, pages 6–10, 2007.

T. Zinner, H. Mannstein, and A. Tafferner. Cb-TRAM: Tracking and monitoring severe convection from onset over rapid development to mature phase using multi-channel Meteosat-8 SEVIRI data. *Meteorology and Atmospheric Physics*, 101(3):191–210, 2008.

CURRICULUM VITAE

Dipl.-Ing. VERA MEYER

BIRTH 26 December 1979, Vienna, Austria
NATIONALITY Austria

EDUCATION

2007-(2010) **Post graduate studies (Ph.D.) in Severe Weather Nowcasting**
at the Faculty of Physics, Ludwig-Maximilians-University Munich,
in cooperation with the Institute of Atmospheric Physics,
German Aerospace Center (DLR), Oberpfaffenhofen, Germany
Topic: Methods of Severe Thunderstorm Nowcasting on the Basis of Three Dimensional Lightning Data and Conventional and Innovative Radar Data
Supervisors: Prof. U. Schumann (DLR), Prof. H.-D. Betz (LMU)

03/2006 **Master's degree** (Dipl.-Ing), Vienna University of Technology
final examination with distinction (GPA 1.0)
Topic: Cloud Condensation Nucleus Activation Experiments of the Water-Soluble Fraction in Urban Aerosol'
Specialisation: Technical Physics - Methods and Technology
Supervisors: Prof. H. Ebel (Vienna University of Technology),
Prof. R. Hitzenberger (University of Vienna)

2005-2006 **Master's thesis in Experimental Aerosol Physics**
at the Institute for Experimental Physics, University of Vienna

01/2004-07/2004 Erasmus exchange program, Technical Physics continued at Geocentrum, Uppsala University, Sweden

2000-2006 **Study of Technical Physics**, TU Vienna

10/2000 **VET-Diploma**, College of Interior Design and Timber Technology
Specialisation: Interior Design and Furniture Making

1999-2000 Supplementary course in rhetorics, HTL Mödling

1998-2000 **College of Interior Design and Timber Technology**
HTL-Mödling, Lower Austria

06/1998 **General qualification for university entrance**, (Reifeprüfung)

1990-1998 Grammar school, BG Wien XVIII, Klostergasse, Vienna

1986-1990 Elementary school, Albertus Magnus Schule der Marianisten, Vienna

SCHOLARSHIPS

2006 Research Scholarship, Vienna University of Technology
2003 and 2005 Scholarships awarded for excellent achievement, Vienna University of Technology

EMPLOYMENTS History

03/2010 – 06/2010 Science Officer, German Aerospace Center (DLR), Oberpfaffenhofen, Germany,
Severe Weather Nowcasting (continued)

02/2007 – 01/2010 Doc-position, German Aerospace Center (DLR), Oberpfaffenhofen, Germany,
Severe Weather Nowcasting

02/2007 – 08/2007 Secondment to nowcast GmbH, Germany,
Quality testing of lightning data from European lightning detection network LINET

10/2006 – 01/2007 Pre-doc position, Faculty of Physics, Ludwig-Maximilians-University
in cooperation with nowcast GmbH, Munich
Data analyses with focus on finding and testing possible wave form criteria for the classification of lightning induced electromagnetic signals for operational usage in European lightning detection network LINET

12/2005 – 04/2006 Institute for Experimental Physics, University of Vienna,
Administrative assistance at the COST633 conference in Vienna

